Modeling and Scaling of a Flexible Subscale Aircraft for Flight Control Development and Testing in the Presence of Aeroservoelastic Interactions

Jeffrey Ouellette

Dissertation submitted to the Faculty of the
Virginia Polytechnic Institute and State University
in partial fulfillment of the requirements for the degree of

Doctor of Philosophy
in
Aerospace Engineering

Mayuresh Patil, Chair
Rakesh Kapania
Craig Woolsey
Mazen Farhood

August 14, 2013
Blacksburg, Virginia

Keywords: Flight Dynamics, Flexible Structures, Aeroelasticity, Aeroservoelasticity, Subscale, Aircraft Scaling, Flight Control, Adaptive Control

Modeling and Scaling of a Flexible Subscale Aircraft for Flight Control Development and Testing in the Presence of Aeroservoelastic Interactions

Jeffrey Ouellette

(ABSTRACT)

The interaction of an aircraft's structure and the flight dynamics can degrade the performance of a controller designed only considering the rigid body flight dynamics. These concerns are greater for the next generation adaptive controls. These interactions lead to an increase in the tracking error, instabilities in the control parameters, and significant structural excitations. To improve the understanding of these issues the interactions have been examined using simulation as well as flight testing of a subscale aircraft. The scaling required for such a subscale aircraft has also been examined. For the simulation a coordinate system where the non-linear flight dynamics are orthogonal to the linear structural dynamics was defined. The orthogonality allows the use of separates models for the aerodynamics. For the non-linear flight dynamics, preexisting table lookups with extended vortex lattice are used to determine the aerodynamic forces. Strip theory is then used to determine the smaller, but still important, unsteady aerodynamic forces due to the flexible motion. Because the orientation of the engines is dependent on the structural deformations, the propulsive force is modeled as a non-conservative follower force. The simulation of the integrated dynamics is then used to examine the effects of the aircraft flexibility and resultant ASE interactions on the performance of adaptive controls. For the scaling, the complete similitude of a flexible aircraft was examined. However, this complete similitude is unfeasible for an actual model, so partial similitude is investigated using two approaches. First, the classical approximations of the flight dynamic modes are used to reduce the order of the coupled model, and consequently the number of scaling parameters required to maintain the physics of the system. The second approach uses sensitivity of the response to errors in the aircraft's nondimensional parameters. Both methods give a consistent set of nondimensional parameters which do not have significant influence on the aeroservoelastic interaction. These parameters do not need to be scaled, thus leading to a viable scaled model. A subscale vehicle has been designed which shows significant coupling between the flight dynamics and structural dynamics. This vehicle was used to validate the results of the scaling theory. Output error system identification was used to identify a model from the flight test data. This identified model provides the frequency of the short-period mode, and the effects of the Froude number on the flexibility.

Contents

List of Figures

List of Tables

Nomenclature

$\mathbf{A}(s)$	Observer filter numerator
b	Wing Span
$\bar{c}$	Mean aerodynamic chord
$\mathbf{C}$	Aerodynamic coefficient matrix
c	Local chord
$C(k)$	Theodorsen's function
$\bar{e}$	Root mean square error
$\|\mathbf{A}\|_F$	Frobenius matrix norm, $\|\mathbf{A}\|_F = \mathrm{tr}\left(\mathbf{A}^T\mathbf{A}\right)$
$\mathbf{F}$	Forces
$\mathbf{g}$	Gravity vector
$\mathbf{H}^e$	Engine angular momentum about the engine centerline
$\mathbf{I}$	Inertia Matrix
$\mathbf{K}$	Modal Stiffness Matrix
$\mathbf{K}_m$	Reference model gain matrix

$\mathbf{K}_p$	Plant high frequency gain
$\mathfrak{k}_{ij}$	Aerodynamic correction factor
k	Reduced Frequency, $k = \frac{\omega \bar{c}}{2V_T}$
$\mathfrak{L}$	Characteristic length matrix for non-dimensionalization
$\mathbf{M}$	Moments
M	Mach number
$\hat{p}$	Non-dimensional roll rate, $\frac{bp}{2V}$
$\mathbf{P}_m$	Reference model pole matrix
$P_p(s)$	Plant characteristic equation
$\bar{q}$	Dynamic pressure
$\hat{q}$	Non-dimensional pitch rate, $\frac{\bar{c}p}{2V}$
$\mathbf{Q}$	Generalized modal force
$\mathfrak{r}$	Reference signal
$\hat{r}$	Non-dimensional yaw rate, $\frac{br}{2V}$
$\mathbf{S}_p$	Adaptive gain, $\mathbf{S} \in \mathbb{R}^{3\times 3}$
S	Wing planform area
s	Laplace variable
$\mathbf{u}$	Plant inputs
$\mathbf{r}$	Position vector
$\mathbf{v}$	Linear velocity

V_T	True airspeed
$\mathfrak{w}_i$	Gauss point weights
$\mathbf{x}$	Plant states
$\overset{*}{x}$	Derivative of x with respect to non-dimensional time , $\overset{*}{x} \triangleq \frac{d}{d\tau}x$
$\mathbf{y}$	Plant outputs
$\mathbf{y}_m$	Reference model output
$\mathbf{Z}_p(s)$	Plant zero matrix
Z_m	Plant zero equation

SUBSCRIPTS

avl	AVL Output
B	Fixed body reference frame
exp	Experimental Data
I	Inertial reference frame
M	Mean axis reference frame

SYMBOLS

$\boldsymbol{\delta}$	Mode shape displacements
$\boldsymbol{\Delta}_a(s)$	Additive unmodeled transfer function matrix
$\boldsymbol{\Delta}_m(s)$	Multiplicative unmodeled transfer function matrix
$\Lambda(s)$	Observer filter characteristic equation

$\boldsymbol{\Omega}$	Observer states
$\boldsymbol{\omega}$	Angular Velocity
ϕ	Euler angle about the x-axis
ψ	Euler angle about z-axis
$\boldsymbol{\varphi}$	Mode shape
$\sigma(t)$	Switching sigma modification
$\boldsymbol{\theta}$	Mode shape rotations
τ	Non-dimensional time, $\tau \triangleq \frac{2V_T}{\bar{c}}t$
θ	Euler angle about y-axis
$\boldsymbol{\Theta}(t)$	Control gains
$\boldsymbol{\Theta}^*$	Non-adaptive control gains
$\boldsymbol{\xi}$	Modal Coordinate

SUPERSCRIPTS

a	At the aerodynamic center
B	Fixed body axis origin
e	Engine reference point
l	Local beam axis
M	Mean axis origin
V	Point on the vehicle

Chapter 1

Introduction

1.1 Motivation

As more efficient structures are being used in modern commercial aircraft, the interaction of the structural dynamics with the flight dynamics is becoming an increasing concern. These interactions are even more significant for the development of next generation flight controls, such as adaptive controls. These adaptive controls show great potential in recovering from a loss of control, one of the leading causes of commercial aircraft accidents[3].

The basic form of an adaptive controller is shown in Figure 1.1. All adaptive controllers have a corresponding non-adaptive control law. This is shown by the black and the blue por-

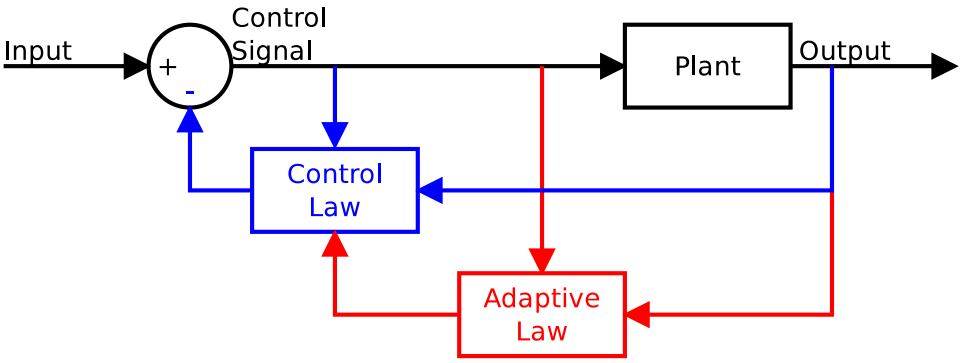

Figure 1.1: Adaptive Controller

tions of Figure 1.1. For a non-adaptive controller, the gains of the control law are calculated from *a priori* models of the system. However, these controllers will only be as effective in the domain for which the model used to determine the parameters was designed. By adding the adaptive law, shown in red, the control gains are determined in real-time based on the system response. The inclusion of the adaptive law allows the controller to compensate for some unknown or unmodeled domain such as a post-stall condition.

However, even if the open loop system is linear, the adaptive laws will result in a non-linear closed loop system. These non-linearities make it impossible to evaluate the control law's performance using analytical tools typically used for linear systems. The analytical tools for non-linear systems, such as Lyapunov stability analysis, generally result in overly conservative estimates of the system response, such as overestimating the error in the system response or underestimating the allowable parameter uncertainty. Thus, simulations and flight tests are still heavily relied upon for the examination and the evaluation of the adaptive control schemes. Since the adaptive parameters are varying in time, it introduces additional transience

In general, the examination of adaptive control laws have focused on rigid aircraft[4]. However, this rigid assumption is unrealistic. The exclusion of the flexibility in any closed-loop control design results in control spillover[5], which causes an increase in the controller's tracking error. The adaptive controls present further complications which can result in instabilities in the control gains, or high frequency control signals that can produce greater structural excitation then a non-adaptive controller. The interaction of the aeroelastic modes generates a parametric uncertainty in the flight dynamic modes, model form uncertainty, and structural excitations that need to be considered in the evaluation of these adaptive control laws. The parametric uncertainty is of less concern since the adaptive control laws are designed to handle significant parametric uncertainty. Of a greater concern is the model form uncertainty since the structural dynamics are not considered in the design of the adaptive control. This model form uncertainty makes it impossible for the adaptive controller to find a correct value for the control parameters. This can cause an instability in the control

parameters, and thus in the closed loop system, known as parameter drift. This parameter drift was a contributing factor in the crash of an X-15 aircraft in 1967[6]. Since that time, many modification terms for the adaptive laws have been developed to prevent this parameter drift. However, these modifications cause an increase in the tracking error of the adaptive controller, resulting in a loss of performance of the controller. To evaluate these modifications, or other potential modifications, tools are needed which will demonstrate this model form uncertainty due to structural dynamics.

Furthermore, in an adaptive controller the control parameters vary in time. For the rapid adaptations needed for upset recovery, these time varying parameters can cause very high frequency control inputs. These high frequency inputs can result in much higher structural loads than would be present with a non-adaptive controller. These tools must also be able to demonstrate these structural excitations.

1.2 Objectives

The aim of the present dissertation is to develop tools which will aid in the evaluation and development of the next generation adaptive flight control laws for commercial transport aircraft. This work focuses on the utilization of subscale models to achieve this. These models offer a safer and more cost effective means of testing flight control laws. The work is broken down into three primary areas; modeling, scaling, and flight testing.

- Modeling
  - Including flight dynamic and structural degrees of freedom
  - Exhibit degradation of adaptive controls
    - Reduced tracking performance
    - Structural excitation by adaptations
- Scaling

  - Parameters to relate subscale and fullscale vehicles
  - Simplified set of parameters for model design

- Flight Testing
  - Demonstrate ability of subscale model to show coupling
  - Demonstrate effects of velocity on short-period mode
    * Validation of scaling theory

The first piece of these tools is the modeling and simulation. This represent the safest and most cost effective means of evaluating the control laws. The simulation must accurately capture the non-linearities present in the flight dynamics. But it must also include the structural dynamics, such that the model will demonstrate the needed model form uncertainty and the structural excitation.

To demonstrate the capabilities of the simulation, a simple adaptive control scheme is examined. This output feedback model reference adaptive control (MRAC) is shown to be sufficient for a flexible vehicle. The control scheme must still demonstrate the ability of the current tools to model the anticipated complications present in adaptive controls.

Although the present work is focusing on the use of subscale models, it is still necessary to consider the scaling of these models such that the results can be applied to a realistic transport aircraft. To achieve this the complete similitude of a flexible vehicle is demonstrated. However, it is not feasible to create a subscale model which will achieve this complete similitude. Therefore, the interaction of these dynamics are further examined to demonstrate a scaling which will still achieve sufficient similarity in the dynamics to create a model relevant for evaluating adaptive flight controls.

Unfortunately there is very little experimental data available for the validation of the simulation or the scaling. Thus, a vehicle has been developed which shows these interactions between the flight dynamics and the structural dynamics. By using frequency domain identification techniques, the experimental data will be compared against the simulation.

The present simulation demonstrates a new method of using the mean axis system. Not for simplification of the equations, but for the application of different aerodynamic models. The adaptive control shows for the first time that specifically the structural excitations can be increased by adaptive controls. Highlighted the need to include the structure in future adaptive control design. The scaling presents two new methods of determining partial matching for constructing a subscale model. These approaches were used to show that if the focus is the short-period mode, that the Froude number can be neglected. Finally the flight testing validated the independence of the short-period mode and the Froude number.

Chapter 2

Literature Review

As with the rest of this dissertation, the literature review has been broken down into four sections. The first section focuses on work related to the integrated modeling. The modeling includes integrated aeroelastic and flight dynamics modeling, as well as aeroelastic modeling which goes beyond the capabilities of previous integrated modeling. The second section focuses on the scaling, from the origins to many specific applications to aircraft. The Third section on the flight testing gives a history of several subscale vehicle studies as well as a sampling system identification techniques. The final section focuses on the issues of controlling a flexible vehicle focusing on the limited history of adaptive controllers.

2.1 Modeling

There have been several works considering the aeroelastic response in an effort to determine the loads acting on the aircraft. The loads on a highly flexible flying wing due to random gust loads was explored by Patil[7]. This time domain simulation used a sum of sinusoids weighted to match the von Kármán gust spectrum acting on the structure. For small gusts the power spectrum density of the time domain results was shown to match well against the analytical frequency domain results for a linear structure. In contrast, Kier and Looye[8] generated

a time domain simulation of the gust and maneuver loads on an undamaged conventional aircraft with a linear structure. The aerodynamics were modeled using a doublet lattice method (DLM). A rational function approximation (RFA) was used to translate the frequency domain DLM data into the time domain. The time domain model using the nonlinear equations of motion was used to show the loads due to a discrete sinusoidal gust and was compared against the results of a frequency domain model which had been transformed to the time domain. Roughen, Bendiksen, and Baker[9] generated linear state-space models of a flexible aircraft. The models include only structural dynamics, no rigid body motion. A low order model was generated from a high fidelity finite element model of the structure. The aerodynamics are expressed in the time domain by the use of Roger's rational function approximation. A reduced order model is generated by balance order reduction using modal truncation. The resulting reduced order model was shown to match a full order NASTRAN model of the AGARD 445.6 wing. Torralba et al.[10] use a set of aeroelastic models to fit a response surface giving the wing loads as a function of the parameters of the system such as the Mach number and airspeed.

There have also been several studies in the effect of a follower load, such as an engine, on the structural response. Using variational methods, Hodges[11] derived equations of motion for a cantilevered beam with a force whose orientation depends on the beam deflection, a follower force. It was shown that for a constant force a follower force results in a change in the effective stiffness, and can cause a dynamic instability in the beam. The work of Detinko[12] showed very similar results. Mazidi et al. [13] explored this further examining the effect of a follower force from the engine on an aircraft wing undergoing a roll maneuver. It was again shown that the follower force will reduce the effective stiffness and the flutter speed of the aircraft.

2.1.1 Integrated Modeling

2.1.1.1 Linear Structure

Although not a standard practice, there have been several efforts to generate integrated models of the flight dynamics and the structural dynamics. Much of the earliest work focused on vehicles with linear structural dynamics. One of the earliest such works is shown by Milne[14]. The equations of motion were derived for several different coordinate systems. These include a body-fixed axis system and a principle axis system, which simplifies the equations for the rotational dynamics. Also it was shown by defining a mean axis system such that linear and angular momentum of the structural motion is zero, that the flight dynamics and structural dynamics will be coupled only by the aerodynamics. The mean axis system is further demonstrated in the work of Waszak and Schmidt[15]. Energy methods were used to derive the equations of motion of a flexible aircraft. The mean axis system was used to simplify these equations. It was shown that if the aircraft's inertia matrix is assumed to be constant then the mean axis system will remove the inertial coupling in the equations of motion. They will however remain coupled by the aerodynamic forcing terms. A quasi-steady strip theory was then used to determine the effect of the flexibility of the aircraft stability. This flexibility was also shown to effect the zeros of the system transfer functions. Waszak et al.[16] used the same model in a simulator study to examine the effects of the flexibility on the aircraft's handling qualities. It was shown that significant flexibility can make the aircraft much more difficult to fly. This same model was used by Baghdadi et al.[17] to demonstrate the use of bifurcation techniques to examine the aircraft dynamics. This technique examines the variations in the steady state solutions as the horizontal stabilizer deflection is varied. This provides insight to the system dynamics, without requiring costly simulations.

There have also been more recent efforts to apply the mean axis formulation. Many of these efforts have used a strip theory to determine the unsteady aerodynamic effects using several different methods. The work of Silvestre and Luckner[18] used a convolution integral to determine the unsteady effects. Although this approach can potentially provide

an analytical solution for the given strip theory, it is very computationally expensive. To reduce the cost, Pogorzelski et al.[19] used a rational function approximation of the unsteady aerodynamics. By creating a similar rational function approximation from a doublet lattice model Reschke[20] created a simulation which offers greater fidelity in the results, with only an increase in the prepossessing cost.

An alternative approach to the motion of a flexible aircraft is given in the work of Meirovitch and Tuzcu[21, 22, 23]. This approach models the aircraft as a collection of independent bodies. The wing, fuselage, horizontal, and vertical tails each have their own degrees of freedom, that are then related to an axis system fixed on the aircraft. This results in a different set of constraints on the structural dynamics. Rather then the free-free modes required by the mean axis system, this formulation uses the cantilevered modes of each body of the aircraft. This formulation was also used by Nguyen and Tuzcu[24, 25, 26] to model a flexible commercial aircraft. Grant, Abbasi, and Li[27, 28] applied both of these approaches to the same aircraft model, for comparison of the results. With out a validation case, it was impossible to draw significant conclusions from the small differences between the models.

2.1.1.2 Non-Linear Structure

The use of linear structural models is inadequate for some aircraft, especially high aspect ratio flying wings. These vehicles have lead to efforts to model such geometrically non-linear structures. Each of the three models discussed here discretized the vehicle into separate elements. The motions of these elements are constrained by the given structural model. Unlike the previous models, which make a clear separation of the equations for the flight dynamics, the rigid body motion is implicit in the constraints. Patil and Hodges[29] use an intrinsic beam formulation which defines constraints as a function of the velocity of the element nodes. Sotoudeh et al.[30] used a variety of test cases to further test this model. Zhao and Ren[31] instead treat element as rigid bodies connected by discrete springs. For sufficient elements, these results are consistent with other models.

2.1.1.3 Body Freedom Flutter

Body freedom flutter is a well known, although not well understood, instability which results from the interaction of the flight dynamics and the structural dynamics. In an effort to examine the origin of the instability Niblett[32] used a simplified model with only three degrees of freedom. Due to the very simple model, the results are inconclusive. Love et al.[33] used both a linear NASTRAN model and a non-linear ASWING model of a flying wing configuration to demonstrate the body-freedom flutter. The interaction of the short-period mode with the structure was shown to create an instability at flight speeds well below the typical flutter, i.e. bending-torsion flutter, speed.

2.2 Control

2.2.1 Robust/Optimal Control

Although the present focus is on adaptive control, there have been a lot more studies on non-adaptive controls and many of the issues remain the same. The structural dynamics have infinite degrees of freedom. As a result it is necessary to use a reduced order model for the control synthesis. Haddad and Bernstein[34] present a methodology for generating an observer for a reduced order system. These observers are designed to work for unstable modes, as long as the unstable modes are observable in the output. These reduced order observers provide the states for the control laws. Prudhomme[35] goes further, examining the application of optimal, linear quadratic Gaussian (LQG), control laws to reduced order models. It is shown that, depending on the model reduction used, the resulting performance of the "optimal" control law may inferior to a non-optimal controller.

It is important that the controller does not generate control inputs which are large enough to damage the aircraft's structure. Frost et al.[36] addresses this by including the load constraints into the optimization to determine the control gains. The loads introduce an

additional Lagrange multiplier in the cost function. Alternatively, the controller can be designed to reduce the loads on the aircraft. Moulin and Karpel[37] developed controllers for discrete gust load alleviation. Frequency domain models were used for load determination and state-space models were used for control synthesis. Accelerometer measurements on the wing were sufficient input to enable minimization of the root bending moment. Additional control surfaces on the wings were shown to yield a further reduction in the gust loads. Tuefel et al.[38] consider the loads from multidimensional random gusts. The controller showed that it is possible to reduce the loads due to gusts, but that oversimplification of the gusts for control synthesis would inhibit the load reductions. Haghighat et al.[39] includes the design of the load alleviating controller into the design of the wing structure. Since the required wing strength is reduced by the controller, the resulting vehicle offered a significant increase in efficiency.

The controllers can also be used to delay the onset of flutter. Gang et al.[40] use a linear optimal controller to suppress the instability due to flutter. To avoid the performance costs shown by Prudhomme[35], the reduction of the model is done by balanced proper orthogonal decomposition.

2.2.2 Adaptive Control

Gadient et al.[41] compared the classical model reference adaptive control (MRAC) and composite MRAC (CMRAC) to a robust linear controller. All three controllers were applied to the nonlinear simulation of the Generic Transport Model (GTM). Both adaptive controllers were shown to have similar performance. The CMRAC had an equal or lower power to the inputs. This would potentially reduce the excitation of the structure, but there is no formal proof, and the effects of the structure are not considered in this work.

Hinson et al.[42] use a model of a general aviation aircraft to examine an adaptive nonlinear dynamic inversion controller. The controller was restricted to the longitudinal dynamics. The controller uses an adaptive neural network to approximate the functions for

the inversion. A notch filter was added to the controller to suppress any excitation of the structure. The notch filter was able to improve the performance of the controller, but the implementation of such a notch filter does require more knowledge than some other methodologies. Calise et al.[43, 44] used a similar dynamic inversion controller. However, for this case there was a non-adaptive baseline controller. The neural network augmented this baseline controller to correct for the changes in the system. In this case the notch filter was found to have a very small effect.

Zeng et al. [45] examine the possibility of designing the a controller without a notch filter. A model of the F/A-18 Active Aeroelastic Wing was used for this study. The notch filters did have some benefit even if the structural parameters changed. As one would expect the notch filters became significantly less effective. The controller of Li et al.[46] uses narrow bandwidth filter technology to identify the structural mode. This approach examines a limited bandwidth of outputs frequency content to identify the frequency of the structural mode. This is then applied to the notch filter. This approach was able to suppress the excitation of the structure, without requiring *a priori* knowledge of the structure.

Kim et al.[47] apply an adaptive controller based on a recursive solution to the algebraic Riccati equation typically seen in linear optimal control. This model used the pitch rate, pitch angle, and one structural modal displacement for output. The inputs used were a combination of the the elevators and flap deflections. Since the structure appears in the output and only one structural degree of freedom was used in the plant, this does not demonstrate the robustness to unmodeled dynamics. It does however demonstrate that the controller is able to be applied to a system with non-minimum phase zeros.

Nguyen et al.[48, 49] demonstrate an alternative to the traditional σ and e modifications that will yield robust adaptive control laws. This modification known as optimal control modification attempts to minimize the $\mathcal{L}_2$ norm of the tracking error, rather then just applying the modification to a control law designed to drive the tracking error to zero. This appears to give a significant reduction in the tracking error, with only a minimal increase in the complexity of the adaptive law.

Avanzini et al.[50] applied the $\mathcal{L}_1$ adaptive control law to the longitudinal dynamics of an aircraft which included one structural mode for the wing and one for the fuselage. The $\mathcal{L}_1$ adaptive control law applies a filter to the control signals. This allows for very high rates of adaptation without the typical loss of robustness. It was shown that the filter can be designed to limit the interactions as is typically done with notch filters.

Adaptive controllers are useful for more then controlling the flight dynamics. Roemer at al.[51] used an adaptive control law for suppressing the instability due to flutter. They used an indirect adaptive controller, which means that the controller identifies the system parameters. These parameters were then used in a traditional controller, such as μ-synthesis. This approach was shown to successfully reduce the instabilities even when the wing properties changed, such as due to damage.

2.3 Scaling

In 1914 Buckingham[52] showed that similarity between two systems can be achieved by matching the nondimensional parameters. Buckingham also showed that by writing in terms of nondimensional parameters the total number of parameters is reduced. Therefore, it is possible to create subscale models, which can be related to the fullscale by the examination of the nondimensional parameters. This complete similitude becomes very difficult for more complex systems such as an aircraft. Instead a partial matching of the system parameters is used. Wolowicz, Bowman, and Gilbert[53] discuss the partial similitude that is currently used in creating models for a variety of different tests. These tests include rigid windtunnel models, rigid models for free flight, and aeroelastic models for windtunnel. The review of these models is comprehensive, but provides no discussion of a partial similitude that could be used for creating a model for flight testing which will capture the interaction of the flight dynamics and the structural dynamics. This similitude, including for linearized compressible flow, was examined for a wing with a control surface by Presente and Friedmann[54, 55].

Much of the current discussion in scaling focuses in the creation of models to match the

conditions set forth by these earlier works. An example of a subscale vehicle designed for the study of body-freedom flutter is the X-56A, formerly the Multi-Utility Technology Testbed (MUTT)[56, 57]. The X-56A is a subscale model of AFRL's sensorcraft project. This vehicle is designed with an interchangeable wing so that it can be used to examine both the flying wing and joined wing configurations being examined. It was found that complete scaling of the vehicle was not practical for this project. Instead the aircraft was geometrically scaled, and then the stiffness of the structure was reduced such that the joined wing aircraft would experience body-freedom flutter at a speed within the subscale aircraft's flight envelope. This approach is able to produce an aircraft that demonstrates body-freedom flutter. However, this scaling does not guarantee similarity in the body freedom flutter between the subscale and fullscale vehicles. Therefore this model can be used to study the physics of body freedom flutter, but the results cannot be related to a full scale vehicle. A separate effort with the sensorcraft is presented by Richards et al.[58, 59]. This vehicle is a 1/9th scale model designed to examine the gust response of the joined wing Sensorcraft. This model does achieve similitude, but is not designed to capture both the flight dynamics and the resulting interactions with the structural dynamics.

2.4 Flight and Ground Testing

The ground vibration tests of Templeton and Rice[60] demonstrate the ability to determine the free-free modes of a vehicle experimentally. The Generic Transport Model was suspended by bungee cords, such that the resulting modes would be much lower then the structural modes. Thus the resulting modal frequencies are representative of the free-free modes. These tests also provide the mass normalized mode shapes. Although the shapes are limited to plunge of the wing and horizontal tail and sway of the vertical tail.

2.4.1 Current Aeroservoelastic and Subscale Flight Testing

There have been a number of flight test programs which examine the aeroservoelastic response of an aircraft as well as programs to test adaptive control laws. One example of a program to examine aeroservoelasticity was the F/A-18 Active Aeroelastic Wing (AAW) Program. As part of this program Brenner and Prazenica[61] used the flight test data to do identification of the non-linear dynamics. Since the conclusion of the AAW program, the vehicle, now known as the Full-Scale Advance Systems Testbed (FAST)[62, 63], has been modified for the study of adaptive controls. These modifications include the ability to switch between a baseline controller and the experimental control laws. With this vehicle's flexible wing, it offers great potential for studying the interaction of the aeroservoelastic dynamics, but it is unclear how these results would relate specifically to a commercial aircraft.

In addition to this fullscale vehicle there have been a variety of efforts using subscale vehicles. The Airborne Subscale Transport Aircraft Research Testbed (AirSTAR) refers to a set of aircraft and the associated ground facilities which were developed for examining loss of control (LOC) events for commercial aircraft. The first vehicle was the S-2 Aircraft[64], which is an off-the-shelf model fitted with additional instrumentation. This aircraft was used for initial development of the procedures and ground facilities. This allows testing and development without risking the more sophisticated and more expensive dynamically scaled aircraft. In addition to the S-2 aircraft, two dynamically scaled aircraft have been developed by Jordan et al.[65, 66]. These aircraft are known as the GTM-T1 and GTM-T2. These aircraft were designed to be 5.5% scaled version of an actual commercial aircraft. The GTM-T2 has a lighter airframe allowing for additional instrumentation and electronics. Both of these vehicles were dynamically scaled such that the flight dynamics can be related to a fullscale vehicle. The vehicle has a very stiff structure which is very difficult to measure, because the structural scaling was not considered in the design. The stiffness combined with a lack of measurement of the structure makes it very difficult to examine the aeroservoelastic interactions.

In an effort to validate the models of high altitude long endurance (HALE) aircraft, Cesnik et al.[67] are developing a subscale model of a high aspect ratio flying wing known as X-HALE. This model does capture the complete coupling present in these HALE aircraft. However, due to large structural deformations, these vehicles exhibit significantly different behavior then a traditional transport aircraft. Furthermore, since this is primarily an effort to validate computer models, this effort does not examine the scale effects for these couplings.

2.4.2 Aircraft System Identification

2.4.2.1 Input Design

The first step in system identification is determining the inputs to the system, which will have a significant effect on the quality of the results. It is preferable for the inputs to uniformly excite a broad spectrum of frequencies, so that the power spectrum density is flat. It is also preferred that the control deflections will remain small, so that the system response remains linear and so that controls are not saturated. Morelli[68] developed a multi-input frequency sweep to achieve both of these goals. This Morelli sweep, based on the single input Shroeder sweep, uses a sum of phase shifted sinusoids. However, the frequencies of the sinusoids to each input are selected so that the control signals are orthogonal to each other. This makes the contribution of each input to the system response more clear. The phase shift of each sinusoid is selected to maximize the root mean square value of the input, while minimizing the bounds on the input.

Brenner et al. [69] examined the aeroelastic response of an F/A-18 based on flight test data. The data included linear and logarithmic frequency sweeps to special exciters which were mounted to the wing tip. Also a Shroeder sweep and sinc pulses were applied to the controls. The sinc pulses offer a flat PSD similar to the Schroeder sweep, but have a much larger peak deflection.

Troyer et al.[70] use a nonparametric system identification to determine the excitation due to gust loads during a flight test. The estimates of the gust excitations are then used

as an additional input in the parametric identification. Since the gusts excite a broader spectrum then the controls, it was possible to identify the dynamics in a broader spectrum then from examining the control inputs alone.

2.4.2.2 Frequency Domain Identification

Once the inputs have been selected, it is then necessary to then relate the outputs of the system to the inputs in order to complete the system identification. The use of the frequency domain offers many advantages for the system identification. Typically, the frequency domain requires the data to be analyzed after the conclusion of the flight tests. However, Morelli[71] has developed a method for the real time estimation of aircraft parameters in the frequency domain. Using a recursive form of the discrete Fourier transform, the system output are transformed into the frequency domain in real time. The power spectrum density of the Morelli sweeps used for inputs are flat and the magnitude is known. Therefore, the frequency response is given by the Fourier transform of the outputs. By restricting the bandwidth, the computational cost of a recursive discrete Fourier transform is low enough that it can be performed in real-time. Using a parametrization of the aircraft, which is linear in the parameters, the parameters can be determined using a linear least squares algorithm. This real-time frequency domain identification has been used for number of projects. For example, to reduce the significant costs and the difficulties of calibrating air flow angle vanes, Morelli[72] proposed a method of identification which instead uses the measurements of the aircraft IMU and the airspeed measurement. Rather than measuring the airflow angles directly, they are instead reconstructed using the standard 6 degree of freedom equations of motion. This will tend to create significant bias errors in the reconstructed angles. Because the identification is done in the frequency domain, these errors are removed by the use of a high pass filter, which does not effect the higher frequency data used for the identification. This method was applied to a simulation of an F-16 and flight test data for the GTM-T2 aircraft. The reconstructed angles produced equivalent estimates of the aerodynamic parameters, but at the cost on increased uncertainty.

Using a more traditional frequency domain identification technique, Theodore et al.[73] examined the identification of a flexible transport aircraft. This study examined only the lateral dynamics and assumed that there was no effect of the flexible motion of the rigid body dynamics. The coupling was limited to the rigid body motion and control inputs exiting the aircraft structure. The structural motion was limited to the first two modes, and these were assumed to be fully decoupled from each other. The first mode was an asymmetric wing bending mode that was excited by the roll rate, aileron and flaperon. The second mode was a lateral fuselage bending mode excited by the sideslip angle, yaw rate and the rudder. Several manual and automated linear frequency sweeps were used to each of the 3 control surfaces separately. The identification of the aircraft parameters was achieved using the method of Tischler and Remple[74]. The state-space equations of motion are transformed into the frequency domain, and a non-linear optimization is used to minimize the least-squares error in the frequency response. Overall the resulting identified model matches the flight test data. Yet, for high frequency inputs which excite the structure, the lack of coupling from the flexible body motion to the rigid body motion can be observed.

2.4.2.3 Time Domain Identification

Rather then using the cross spectral density to remove the noise from the output signal, the work of Callafon et. al[75] used the covariance functions. The resulting input and cross covariance are used to determine the system's Markov-parameters. The discrete time system response is then given by the Markov-parameter convolution. Unlike the work in Section 2.4.2.2, this is an unstructured identification of the system. A simulation of the F/A-18AAW aircraft with noise was used to demonstrate the methodology. The identified model was compared to the simulation results with and without noise and disturbances. The system identification was able to correctly remove the noise and matched the simulation with the noise removed.

Although the frequency domain offers advantages for the system identification, it does limit the analysis to linear systems. To handle nonlinear systems, the use of time domain

techniques are needed. In the time domain, neural networks can be used for the nonparametric identification of non-linear system dynamics. Boely and Botez[76] examined the identification of a non-linear structural response of an F/A-18 using Neural Networks. Newton's method was used to train the neural network from flutter flight test data. The resulting model showed very strong correlation. However, the neural network provides little physical insight to the system dynamics. A structured identification offers greater insight to the physics. Silva [77] used the parametrization of Waszak and Schmidt[15] for a time domain identification of a flexible aircraft. A variety of inputs were used such as frequency sweeps and doublets. Using the flight test data from an SB 10 glider, which has a very flexible wing, an accurate model was identified without the assumptions used by Theodore et al.[73].

Generally in system identification the aerodynamics loads are measured indirectly as their effect on the structural or rigid body response. In contrast, Mangalam et. al[78] are using a hot film sensor to measure the leading edge stagnation point. This measurement along with the Kutta condition can be used to determine the circulation and thus the aerodynamic loads. They then demonstrate a strong correlation between the work done by these aerodynamic loads and the system response for the onset of flutter.

Chapter 3

Modeling and Simulation

The primary goal of the present modeling is for the examination of flight controls, therefore the focus is on the rigid body (flight) dynamics. These rigid body dynamics can have large displacements resulting in significant non-linearities. However, these dynamics are of a finite low order (6 degrees of freedom), and are relatively slow. In contrast, the structural deformation has infinite degrees of freedom, but the deflections are small enough to allow for a linear approximation. Due to the differences in the flight dynamics and structural dynamics, it is desirable to separate these dynamics as much as possible to allow different aerodynamic models which will better represent the physics present. The use of the mean axis system, shown in Figure 3.1, gives a unified set of equations off motion for the non-linear rigid body and linear structural dynamics while ensuring that these motions remain orthogonal. The decoupling due to the mean axis system allows for a high fidelity nonlinear quasi-steady aerodynamic model for the loads due to rigid body dynamics and a low fidelity unsteady aerodynamic model for the loads due to small unsteady structural motion. This modeling approach is applied to the NASA Generic Transport Model (GTM), a 5.5% scaled model of a commercial aircraft.

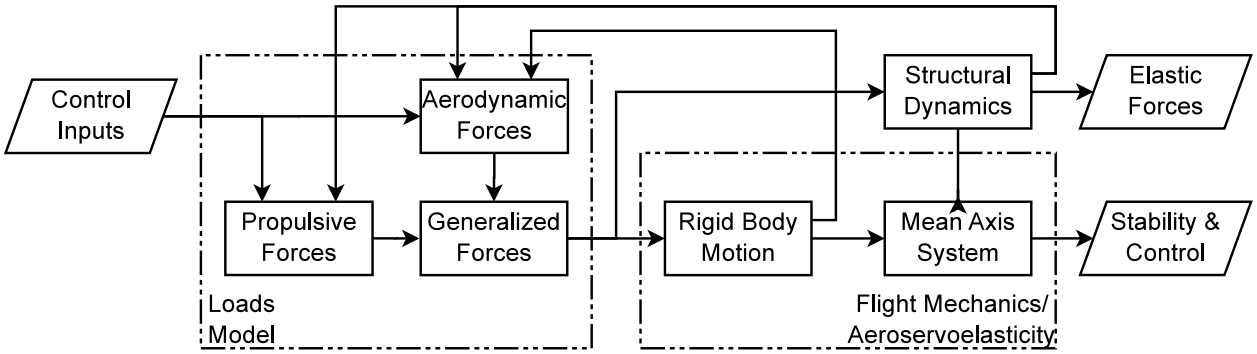

Figure 3.1: Aeroservoelastic Modeling Methodology

3.1 Flight Mechanics and Aeroelasticity

Several coordinate systems are used to represent the aircraft's motion and the forces on the aircraft. The first coordinate system is the inertial coordinate system fixed to a point on the earth. Since different models are used for the forcing of the non-linear flight dynamics and the linear structural dynamics, it is desirable to define these motions about a coordinate system where these two types of motion are orthogonal.

$$\int_V \left\{\boldsymbol{\varphi}_M^{V/M}\right\}_{flexible} \cdot \left\{\boldsymbol{\varphi}_M^{V/M}\right\}_{rigid} dV \quad = \quad 0 \tag{3.1}$$

This is accomplished by defining the axis such that the linear momentum and angular momentum due to the structural deformations are zero.

$$\int_V \rho \left\{\mathbf{v}_M^{V/M}\right\} dV \quad = \quad \{\mathbf{0}\} \tag{3.2}$$

$$\int_V \left\{\mathbf{r}_M^{V/M}\right\} \times \rho \left\{\mathbf{v}_M^{V/M}\right\} dV \quad = \quad \{\mathbf{0}\} \tag{3.3}$$

This axis system is known as the mean axis system[14]. This coordinate system is still not unique so it is further constrained by fixing the coordinate system at the center of gravity which is guaranteed to satisfy the first constraint. In addition to the mean axis system,

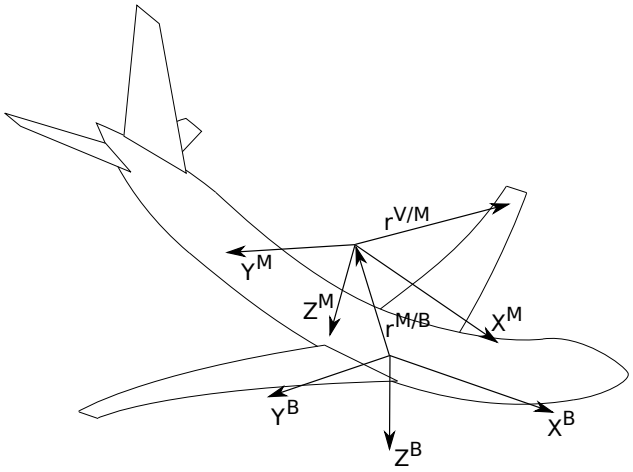

Figure 3.2: Diagram of the Mean and the Body-Fixed Axis Systems

a body fixed axis system is defined such that it will move with the body deformations, consistent with a sensor attached to the aircraft. The equations of motion and the forcing are defined in the mean axis system. The models of the onboard sensors used in the GTM simulation require both the body fixed axis states and their derivatives. Therefore, the time marching is applied to the states in the body fixed axis system. The transformation between these two reference frames requires an additional set of kinematic equations. This approach is needed to keep the orthogonality of the flight dynamics and structural dynamics, which is needed for the aerodynamic models, while providing all of the states required by the sensor models.

3.1.1 Equations of Motion

Since the structural deformations are linear and small, the variations in the aircraft's inertia matrix due to the deformations are negligible. For this time invariant inertia, the equations of motion about the mean axes of a flexible aircraft are given by Waszak and Schmidt[15].

$$m\left\{\dot{\mathbf{v}}_M^{M/I}\right\} + m\left\{\boldsymbol{\omega}_M^{M/I}\right\} \times \left\{\mathbf{v}_M^{M/I}\right\} + m\left[\boldsymbol{\mathcal{C}}^{M/I}\right]\{\mathbf{g}_I\} = \{\mathbf{F}^M\} \quad (3.4)$$

$$\left[\mathbf{I}^M\right]\left\{\dot{\boldsymbol{\omega}}_M^{M/I}\right\} + \left\{\boldsymbol{\omega}_M^{M/I}\right\} \times \left[\mathbf{I}^M\right]\left\{\boldsymbol{\omega}_M^{M/I}\right\} = \{\mathbf{M}^M\} \quad (3.5)$$

$$\left\{\ddot{\boldsymbol{\xi}}\right\} + [\mathbf{K}]\{\boldsymbol{\xi}\} = \{\mathbf{Q}^M\} \quad (3.6)$$

The use of the mean axis system removes the inertial coupling between the rigid body motion, Eqs. 3.4 and 3.5 on one hand, and the flexible body motion, Eq. 3.6 on the other. As a result, the first six equations are identical to the traditional rigid body equations. The remaining equations represent the structural motion. Yet, equations 3.4, 3.5, and 3.6 are still coupled by the forcing terms ($\{\mathbf{F}^M\}$, $\{\mathbf{M}^M\}$, and $\{\mathbf{Q}^M\}$) .

The kinematics of the rigid body flight dynamics modes are represented by Euler angles, as used in traditional flight mechanics[1].

Finite element analysis or ground vibration tests (GVT) provide the frequencies and the mass normalized mode shapes for the *in vacuo* free vibration modes. These free modes are orthogonal to the rigid body motion, and thus are guaranteed to satisfy both the translational and rotational mean axis constraints, Eqs. 3.2 and 3.3. For a subscale vehicle, such as the NASA GTM, these free modes can be easily achieved experimentally by suspending the aircraft with bungee cords. For sufficiently flexible cords, the frequencies will have a negligible effect on the structure, simulating a free mode. For the GTM, the structural model was available from a preliminary GVT test. These earlier tests examined the frequency response of single axis accelerometers at 28 points, to the excitation of an impact hammer at several different locations. The results of the tests were available as the deflections for the first 7 mass normalized modes at each accelerometer, 16 along the wing, 8 along the horizontal tail, and 4 along the vertical tail. The accelerometers had been distributed in pairs along the span of each surface shown in Figure 3.3. The data is transformed into the 2 beam degrees of freedom, deflection and twist at the quarter chord, that are required by the present aerodynamic model. The deflections are determined by a linear interpolation for

Figure 3.3: GVT Wing Accelerometers

each pair. The twist is calculated from the arctangent of the slope of the linear interpolation.

3.1.2 Kinematic Equations

The directional cosine matrix which relates the orientation of the inertial, earth fixed, reference frame and the body-fixed axis system is defined in terms of the three Euler angles.[1]

$$\left[\boldsymbol{C}^{B/I}\right] = \begin{bmatrix} \cos\theta\cos\psi & \cos\theta\sin\psi & -\sin\theta \\ \sin\phi\sin\theta\cos\psi - \cos\phi\sin\psi & \sin\phi\sin\theta\sin\psi - \cos\phi\cos\psi & \sin\phi\cos\theta \\ \cos\phi\sin\theta\cos\psi - \sin\phi\sin\psi & \cos\phi\sin\theta\sin\psi - \sin\phi\cos\psi & \cos\phi\cos\theta \end{bmatrix} \tag{3.7}$$

The Euler angles are calculated from the kinematic equations in terms of the body-fixed axes angular velocities.

$$\left\{\dot{\boldsymbol{\theta}}_I^{B/I}\right\} = \begin{bmatrix} 1 & \sin\phi^{B/I}\tan\theta^{B/I} & \cos\phi^{B/I}\tan\theta^{B/I} \\ 0 & \cos\phi^{B/I} & \sin\phi^{B/I} \\ 0 & \sin\phi^{B/I}\sec\theta^{B/I} & \cos\phi^{B/I}\sec\theta^{B/I} \end{bmatrix} \left\{\boldsymbol{\omega}_B^{B/I}\right\} \tag{3.8}$$

Additionally, the position of the body fixed axis system in the inertial reference frame is determined by integration of the velocity in the inertial frame. The velocity in the inertial

frame is found by the rotation of the body-fixed axes velocities[1].

$$\left\{\dot{\mathbf{r}}_I^{B/I}\right\} = \left[\boldsymbol{C}^{I/B}\right]\left\{\mathbf{v}_B^{B/I}\right\} \tag{3.9}$$

3.1.3 Transformation: Mean Axes to Body-Fixed Axes

The equations of motion give the mean axes states. However, the sensors measuring the aircraft states are fixed to the aircraft and require the body-fixed axes states and rates ($\left\{\mathbf{v}_B^{B/I}\right\}$, $\left\{\boldsymbol{\omega}_B^{B/I}\right\}$, $\left\{\dot{\mathbf{v}}_B^{B/I}\right\}$, and $\left\{\dot{\boldsymbol{\omega}}_B^{B/I}\right\}$). The origin of the body fixed axis system is simply a point that is moving in the mean axis frame. The acceleration of such a point in a non-inertial frame is given by the kinematic equations[79]:

$$\begin{aligned}\left\{\dot{\mathbf{v}}_M^{B/I}\right\} &= \left\{\dot{\mathbf{v}}_M^{M/I}\right\} + \left\{\dot{\boldsymbol{\omega}}_M^{M/I}\right\} \times \left\{\mathbf{r}_M^{B/M}\right\} + 2\left\{\boldsymbol{\omega}_M^{M/I}\right\} \times \left\{\mathbf{v}_M^{B/M}\right\} \\ &\quad + \left\{\boldsymbol{\omega}_M^{M/I}\right\} \times \left(\left\{\boldsymbol{\omega}_M^{M/I}\right\} \times \left\{\mathbf{r}_M^{B/M}\right\}\right) + \left\{\dot{\mathbf{v}}_M^{B/M}\right\} \qquad (3.10) \\ \left\{\dot{\boldsymbol{\omega}}_M^{B/I}\right\} &= \left\{\dot{\boldsymbol{\omega}}_M^{M/I}\right\} + \left\{\dot{\boldsymbol{\omega}}_M^{M/I}\right\} \times \left\{\boldsymbol{\theta}_M^{B/M}\right\} + 2\left\{\boldsymbol{\omega}_M^{M/I}\right\} \times \left\{\boldsymbol{\omega}_M^{B/M}\right\} \\ &\quad + \left\{\boldsymbol{\omega}_M^{M/I}\right\} \times \left(\left\{\boldsymbol{\omega}_M^{M/I}\right\} \times \left\{\boldsymbol{\theta}_M^{B/M}\right\}\right) + \left\{\dot{\boldsymbol{\omega}}_M^{B/M}\right\} \qquad (3.11)\end{aligned}$$

The motion of the body-fixed axis system relative to the mean axis system is available from the modal analysis. However, the transformations in Eqs. 3.10 and 3.11 are in the mean axis frame, to express the velocities and angular rates in the body fixed axis, an additional rotation is required.

$$\begin{aligned}\left\{\dot{\mathbf{v}}_B^{B/I}\right\} &= \left[\boldsymbol{\mathcal{C}}^{B/M}\right]\left(\left\{\dot{\mathbf{v}}_M^{M/I}\right\} + \left\{\dot{\boldsymbol{\omega}}_M^{M/I}\right\} \times \left[\boldsymbol{\delta}_M^{B/M}\right]\{\boldsymbol{\xi}\} + 2\left\{\boldsymbol{\omega}_M^{M/I}\right\} \times \left[\boldsymbol{\delta}_M^{B/M}\right]\left\{\dot{\boldsymbol{\xi}}\right\}\right. \\ &\quad \left. + \left\{\boldsymbol{\omega}_M^{M/I}\right\} \times \left(\left\{\boldsymbol{\omega}_M^{M/I}\right\} \times \left[\boldsymbol{\delta}_M^{B/M}\right]\{\boldsymbol{\xi}\}\right) + \left[\boldsymbol{\delta}_M^{B/M}\right]\left\{\ddot{\boldsymbol{\xi}}\right\}\right) \qquad (3.12) \\ \left\{\dot{\boldsymbol{\omega}}_B^{B/I}\right\} &= \left[\boldsymbol{\mathcal{C}}^{B/M}\right]\left(\left\{\dot{\boldsymbol{\omega}}_M^{M/I}\right\} + \left\{\dot{\boldsymbol{\omega}}_M^{M/I}\right\} \times \left[\boldsymbol{\theta}_M^{M/B}\right]\{\boldsymbol{\xi}\} + 2\left\{\boldsymbol{\omega}_M^{M/I}\right\} \times \left[\boldsymbol{\theta}_M^{M/B}\right]\left\{\dot{\boldsymbol{\xi}}\right\}\right. \\ &\quad \left. + \left\{\boldsymbol{\omega}_M^{M/I}\right\} \times \left(\left\{\boldsymbol{\omega}_M^{M/I}\right\} \times \left[\boldsymbol{\theta}_M^{M/B}\right]\{\boldsymbol{\xi}\}\right) + \left[\boldsymbol{\theta}_M^{M/B}\right]\left\{\ddot{\boldsymbol{\xi}}\right\}\right) \qquad (3.13)\end{aligned}$$

Time marching of these states will yield the body-fixed axes states and the rates required by the sensors.

3.1.4 Transformation: Body-Fixed Axes to Mean Axes

To maintain the orthogonality in the dynamics provided by the mean axis system, it is necessary to transform the body-fixed axes states back to the mean axis system for the next time step. The non-linear transformation of the velocity in the mean axis system to the body-fixed axes frame is given by[79]:

$$\left\{\mathbf{v}_B^{M/I}\right\} = \left\{\mathbf{v}_B^{B/I}\right\} + \left\{\boldsymbol{\omega}_B^{B/I}\right\} \times \left\{\mathbf{r}_B^{M/B}\right\} + \left\{\mathbf{v}_B^{M/B}\right\} \tag{3.14}$$

$$\left\{\boldsymbol{\omega}_B^{M/I}\right\} = \left\{\boldsymbol{\omega}_B^{B/I}\right\} + \left\{\boldsymbol{\omega}_B^{B/I}\right\} \times \left\{\boldsymbol{\theta}_B^{M/B}\right\} + \left\{\boldsymbol{\omega}_B^{M/B}\right\} \tag{3.15}$$

As was done previously, the motion of the mean axis system is given by the modal states. Therefore, the mean axes states can be written in terms of the available body-fixed axes states.

$$\left\{\mathbf{v}_M^{M/I}\right\} = \left[\boldsymbol{\mathcal{C}}^{B/M}\right]^T \left(\left\{\mathbf{v}_B^{B/I}\right\} - \left\{\boldsymbol{\omega}_B^{B/I}\right\} \times \left[\boldsymbol{\mathcal{C}}^{B/M}\right] \left[\boldsymbol{\delta}_M^{B/M}\right] \{\boldsymbol{\xi}\}\right) - \left[\boldsymbol{\delta}_M^{B/M}\right] \left\{\dot{\boldsymbol{\xi}}\right\} \tag{3.16}$$

$$\left\{\boldsymbol{\omega}_M^{M/I}\right\} = \left[\boldsymbol{\mathcal{C}}^{B/M}\right]^T \left(\left\{\boldsymbol{\omega}_B^{B/I}\right\} - \left\{\boldsymbol{\omega}_B^{B/I}\right\} \times \left[\boldsymbol{\mathcal{C}}^{B/M}\right] \left[\boldsymbol{\theta}_M^{B/M}\right] \{\boldsymbol{\xi}\}\right) - \left[\boldsymbol{\theta}_M^{M/B}\right] \left\{\dot{\boldsymbol{\xi}}\right\} \tag{3.17}$$

3.2 Loads Model

The forces acting on the aircraft include a distributed loading due to the aerodynamics and a concentrated loading due to the engines.

3.2.1 Aerodynamic Loads

The aerodynamic loads are separated into four categories, shown in Table 3.1. The first two

Table 3.1: Categories of Loads

		Loads a Function of	
		Rigid	Flexible
Loads Act Upon	Rigid	Windtunnel Based Quadratic Quasi-Steady 3-D Effects	Strip Theory Linear Unsteady 2-D Theory
	Flexible	VLM Based Quadratic Quasi-Steady 3-D Effects	Strip Theory Linear Unsteady 2-D Theory

are the forces due to the motion of the rigid body modes. The rigid body states, $\left\{\mathbf{v}_M^{M/I}\right\}$ and $\left\{\boldsymbol{\omega}_M^{M/I}\right\}$, are the primary factors affecting the loads causing the rigid body dynamics and the flexible dynamics. Therefore, a moderate to high fidelity aerodynamic model which can capture the 3-D effects as well as the nonlinearities due to a large angle of attack or sideslip is used. Since the rigid body states have a low reduced frequency, a quasi-steady model is sufficient for capturing the aerodynamic loading.

The loads on the rigid body dynamics and the flexible dynamics are also a function of the structural states. Although the structural motion has a smaller effect on the overall loads, they do have an important effect on the coupling between the rigid and flexible body motion, and thus cannot be neglected. However, the flexible body motion will be at a much higher reduced frequency. To capture these effects, a low fidelity 2-D unsteady linear aerodynamic model is used.

These two models are combined to give a set of non-dimensional coefficients, which define a surrogate model relating the rigid-body motion, flexible motion, and control deflections to the aerodynamic forces. The resulting surrogate model of the forces at the quarter chord is

of the form:

$$\left\{ \begin{array}{c} \frac{d}{dy}\mathbf{F}_M^a \\ \frac{d}{dy}\mathbf{M}_M^a \end{array} \right\} = \bar{q}S\left[\mathfrak{L}\right]\left(\left[\begin{array}{cc} \mathbf{C}_{rigid}^a & \mathbf{C}_{struc}^a \end{array} \right] \left\{ \begin{array}{c} \boldsymbol{x}_{rigid} \\ \boldsymbol{x}_{struc} \end{array} \right\} + C\left(k\right) \left[\begin{array}{c} \mathbf{C}_{us}^a \end{array} \right] \left\{ \begin{array}{c} \boldsymbol{x}_{struc} \end{array} \right\} \right) \tag{3.18}$$

Where the diagonal matrix of the characteristic lengths is given by Eq. 3.19.

$$\left[\mathfrak{L}\right] = \text{diag}\left[\begin{array}{cccccc} 1 & 1 & 1 & b & \bar{c} & b \end{array} \right] \tag{3.19}$$

Theodorsen's function used for the unsteady aerodynamics is an irrational function defined in the frequency domain. For the present time domain simulations, this function is approximated by a rational function approximation (RFA). One such RFA for Theodorsen's function is given by Venkatesan and Friedmann[80]. It was shown that the second order function is of the form,

$$C\left(k\right) \approx \frac{n_0 s^2 + n_1 \frac{2V_T}{\bar{c}} s + n_2 \left(\frac{2V_T}{\bar{c}}\right)^2}{s^2 + d_1 \frac{2V_T}{\bar{c}} s + d_2 \left(\frac{2V_T}{\bar{c}}\right)^2} \tag{3.20}$$

Venkatesan and Friedmann selected the parameters of this RFA to minimize the least-squares error under the constraint that the equation would match the exact value at zero frequency and infinite frequency. The resulting parameters are[80]:

3.2.1.1 Loads Due to Rigid Body Motion

The loads on the rigid body modes are expressed as a function of the flight dynamic states by using table lookups. However, these table lookups contain no information about the distributed loads, which are needed for modeling the structural dynamics. To determine the distributed loads, a vortex lattice model, which was available from earlier work [81, 82], was used. The extended vortex lattice code Athena Vortex Lattice (AVL) is used to generate the

Table 3.2: Coefficients of Rational Function Approximation

Parameter	Value
n_0	$\frac{1}{2}$
n_1	0.3930
n_2	0.0439
d_1	0.5520
d_2	0.0440

Table 3.3: Limits on Aerodynamic States for AVL Simulation

State	Lower Limit	Upper Limit
M	0	0.3
α	$-5°$	$10°$
β	$-7°$	$7°$
$\hat{p}$	-0.1	0.1
$\hat{q}$	-0.005	0.005
$\hat{r}$	-0.05	0.05

aerodynamic loads. These forces were calculated in the body axes directions. In addition to capturing the effects of the shed vortex, AVL allows for capturing the effects of viscous forces, flow around slender bodies, wing thickness, camber, and compressible subsonic flow[83].

Since AVL is based on a linear and quasi-steady vortex lattice method, there are several restrictions on the aircraft states. These restrictions on the states are given in Table 3.3. The angle of attack and the sideslip angle are restricted such that no part of the aircraft, wing or tail, has stalled. Furthermore, the code AVL is a quasi-steady method. Therefore, the angular velocities must remain small[83]. The effects of drag will introduce non-linearities into the aerodynamics. To account for these non-linearities, quadratic terms are added to the rigid state vector.

$$\{\boldsymbol{x}_{rigid}\} = \left\{ \begin{array}{cccccccccccccccc} 1 & \alpha & \frac{\alpha^2}{2} & \beta & \frac{\beta^2}{2} & \hat{p} & \frac{\hat{p}^2}{2} & \hat{q} & \frac{\hat{q}^2}{2} & \hat{r} & \frac{\hat{r}^2}{2} & \delta_a & \frac{\delta_a^2}{2} & \delta_e & \frac{\delta_e^2}{2} & \delta_r & \frac{\delta_r^2}{2} \end{array} \right\}^T \tag{3.21}$$

If only linear terms are used, then $\left[\mathbf{C}^a_{rigid}\right]$ represent the traditional linear stability derivatives[1]. Determination of the first column of the coefficient matrix is given by the aerodynamics loads where all the states are equal to zero ($\alpha = 0$, $\beta = 0$, etc.). Since this model remains linear in the coefficients, the remaining coefficients are calculated by linear least squares.

To ensure consistency between the lookup tables used for the rigid body modes and the AVL results used for the flexible modes, a set of correction factors is calculated. To determine the correction factors, the response surface is first determined for both the AVL results and the lookup table data. By comparing the two surrogate models, a correction factor is calculated for each term in the coefficient matrix $\left[\mathbf{C}^a_{rigid}\right]$.

$$\mathfrak{K}_{ij} = \frac{(C_{ij})_{exp}}{(C_{ij})_{avl}} \tag{3.22}$$

As a result of the symmetry of the aircraft, several of the coefficients for the integrated loads are approximately zero. This implies that there is insufficient information in the integrated loads to correct the coefficients for the distributed loads. If $(C_{ij})_{avl} \approx 0$, it will cause an artificially large correction factor. If $(C_{ij})_{exp} \approx 0$ it will drive the correction factor to zero. To ensure that the correction factor does not cancel or over-inflate the coefficients, if either of the coefficients are very small ($< 10^{-5}$), the correction factor is assumed to be one.

3.2.1.2 Loads Due to Flexible Body Motion

The aerodynamics from the flexible motion will have an important effect on the coupling between rigid body motion and the flexible body motion. However, the forces caused by the flexibility are smaller than the forces due to rigid body motion. As a result, it is assumed that the current configuration has a high enough aspect ratio such that 2-D strip theory will provide sufficient accuracy, without a correction for the tip effect. The structural modes also have a much higher natural frequency. Therefore, the unsteady effects will be much more important. The unsteady aerodynamics for a 2-D thin airfoil are given by Theodorsen[84].The

derivatives are rewritten in terms of the non-dimensional time to remove the explicit velocity term from the expression. Using the mode shapes, the forces are written in terms of the modal coordinates, which gives the remaining coefficient matrices for the surrogate model in Eq. 3.18.

$$[\mathbf{C}^a_{struc}] = \begin{bmatrix} 0 & 0 & 0 & 0 & 0 & 0 & 0 & 0 & 0 & 0 & 0 & 0 \\ 0 & 0 & 0 & 0 & 0 & 0 & 0 & 0 & 0 & 0 & 0 & 0 \\ 0 & 0 & -\frac{2\pi c^2}{\bar{c}^2 S} & 0 & -\frac{\pi c^3}{2\bar{c}^2 S} & 0 & 0 & 0 & 0 & 0 & -\frac{\pi c^2}{\bar{c} S} & 0 \\ 0 & 0 & 0 & 0 & 0 & 0 & 0 & 0 & 0 & 0 & 0 & 0 \\ 0 & 0 & -\frac{\pi c^3}{2\bar{c}^3 S} & 0 & -\frac{3\pi c^4}{16\bar{c}^3 S} & 0 & 0 & 0 & 0 & 0 & -\frac{\pi c^3}{2\bar{c}^2 S} & 0 \\ 0 & 0 & 0 & 0 & 0 & 0 & 0 & 0 & 0 & 0 & 0 & 0 \end{bmatrix} \begin{bmatrix} \boldsymbol{\varphi}^a_M & \mathbf{0} \\ \mathbf{0} & \boldsymbol{\varphi}^a_M \end{bmatrix} \quad (3.23)$$

$$\begin{bmatrix} \\ \mathbf{C}^a_{us} \\ \\ \end{bmatrix} = \begin{bmatrix} 0 & 0 & 0 & 0 & 0 & 0 & 0 & 0 & 0 & 0 & 0 & 0 \\ 0 & 0 & 0 & 0 & 0 & 0 & 0 & 0 & 0 & 0 & 0 & 0 \\ 0 & 0 & -\frac{4\pi c}{\bar{c} S} & 0 & -\frac{\pi c^2}{\bar{c} S} & 0 & 0 & 0 & 0 & 0 & -\frac{2\pi c}{S} & 0 \\ 0 & 0 & 0 & 0 & 0 & 0 & 0 & 0 & 0 & 0 & 0 & 0 \\ 0 & 0 & 0 & 0 & 0 & 0 & 0 & 0 & 0 & 0 & 0 & 0 \\ 0 & 0 & 0 & 0 & 0 & 0 & 0 & 0 & 0 & 0 & 0 & 0 \end{bmatrix} \begin{bmatrix} \boldsymbol{\varphi}^a_M & \mathbf{0} \\ \mathbf{0} & \boldsymbol{\varphi}^a_M \end{bmatrix} \quad (3.24)$$

3.2.2 Propulsive Forces

Because the engine is attached to the flexible structure, the orientation of the engine, and thus the propulsive forces, change with the deflections. The orientation of the engine is described by the Euler angles about the x and y axis, shown in Figure 3.4. These angles are functions of the modal coordinates and are assumed to be small. Because the orientation of the propulsive forces is dependent on the structural displacements, it is a non-conservative follower force. This means that the propulsive forces will have an impact on the effective stiffness and damping of the structure. This effect was previously examined for a cantilevered beam by Hodges[11]. It was shown that this follower force can produce a dynamic instability

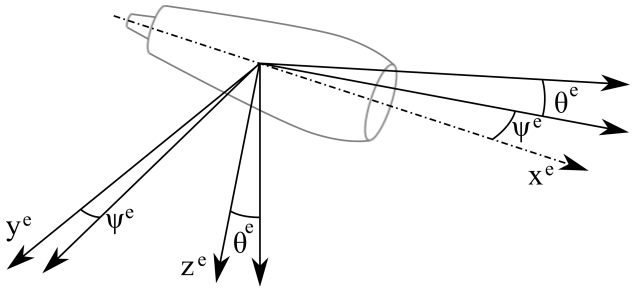

Figure 3.4: Engine Rotation Angles

in the beam. Although, unlikely for the present force to destabilize the wing structure, it is desirable to capture the effects on the frequency and damping of the structure. The engines generate two loads, which include the load due to the thrust and the load due to the engines' angular momentum, gyroscopic force. From the engine model, the angular momentum, is known about the engine's centerline, which is rotated into the mean axes frame.

$$\{\mathbf{H}_M^e\} = \left[\boldsymbol{\mathcal{C}}^{M/e}\right]\{\mathbf{H}^e\} \tag{3.25}$$

The angular momentum is assumed to change very slowly and thus is effectively constant. Euler's equation is used to determine the gyroscopic forces. The moment due to the engine's offset is added to give the total moment of the engine on the wing.

$$\{\mathbf{M}_M^e\} = \{\mathbf{r}_M^{\Delta e}\} \times \left[\boldsymbol{\mathcal{C}}^{M/e}\right]\{\mathbf{F}^e\} + \{\boldsymbol{\omega}^M\} \times \left[\boldsymbol{\mathcal{C}}^{M/e}\right]\{\mathbf{H}^e\} + \left[\dot{\boldsymbol{\mathcal{C}}}^{M/e}\right]\{\mathbf{H}^e\} \tag{3.26}$$

The forces and moments act only about the x-direction of the local engine axes through the engine's centerline, and the structural deformations are small. Thus the force and angular

momentum in the mean axis system becomes,

$$\left[\boldsymbol{\mathcal{C}}^{M/e}\right]\{\mathbf{F}^e\} = \{\mathbf{F}^e_M\} = \left\{\begin{array}{c} 1 \\ \psi^e \\ -\theta^e \end{array}\right\} \|\mathbf{F}^e\| \tag{3.27}$$

$$\left[\boldsymbol{\mathcal{C}}^{M/e}\right]\{\mathbf{H}^e\} = \{\mathbf{H}^e_M\} = \left\{\begin{array}{c} 1 \\ \psi^e \\ -\theta^e \end{array}\right\} \|\mathbf{H}^e\| \tag{3.28}$$

$$\left[\dot{\boldsymbol{\mathcal{C}}}^{M/e}\right]\{\mathbf{H}^e\} = \left\{\dot{\mathbf{H}}^e_M\right\} = \left\{\begin{array}{c} 0 \\ \dot{\psi}^e \\ -\dot{\theta}^e \end{array}\right\} \|\mathbf{H}^e\| \tag{3.29}$$

3.2.3 Generalized Forces

Thus far the load models gave the force and moment distributed on the aircraft. The generalized forces for the present stick model are found from the principle of virtual work[85].

$$\{\mathbf{Q}\} = \int_l \left[\boldsymbol{\varphi}^l_M\right]^T \left\{\begin{array}{c} \frac{d}{dl}\mathbf{F}^l_M \\ \frac{d}{dl}\mathbf{M}^l_M \end{array}\right\} dl \tag{3.30}$$

Since the free modes from the GVT are being used, these generalized forces will be correct for the loads in the mean axis reference frame. The integrated loads on the aircraft are determined similarly by using the rigid body mode shapes.

$$\left[\boldsymbol{\varphi}^l_M\right] = \left[\begin{array}{cc} \boldsymbol{\mathcal{I}}_{3\times3} & -\frac{\pi}{180}\tilde{\mathbf{r}}^{l/M}_M \\ \mathbf{0} & \frac{\pi}{180}\boldsymbol{\mathcal{I}}_{3\times3} \end{array}\right] \tag{3.31}$$

3.2.3.1 Aerodynamic Forces

To determine the generalized forces due to the aerodynamics, the aerodynamic forces per unit span, Eq. 3.18, were applied to the generalized forces, Eq. 3.30. However, the forces in Eq. 3.18 are given at the quarter chord. The mode shapes from the ground vibration tests are offset from the quarter chord. Thus the transformation matrix is used to give the structural displacements at the quarter chord.

$$\left[\boldsymbol{\lambda}_{6\times6}^{a/l}\right] = \begin{bmatrix} \boldsymbol{\mathcal{C}}^{a/l} & \frac{\pi}{180}\boldsymbol{\mathcal{C}}^{a/l}\tilde{\mathbf{r}}^{a/l} \\ \mathbf{0} & \frac{\pi}{180}\boldsymbol{\mathcal{C}}^{a/l} \end{bmatrix} \tag{3.32}$$

The generalized forces are given by the integral,

$$\begin{Bmatrix} \mathbf{F}^M \\ \mathbf{M}^M \\ \mathbf{Q}^M \end{Bmatrix} = \bar{q}S\int_a \left[\boldsymbol{\varphi}_M^l\right]^T \left[\boldsymbol{\lambda}_{6\times6}^{a/l}\right]^T [\mathfrak{L}] \begin{bmatrix} \mathbf{C}_{rigid}^a & \mathbf{C}_{struc}^a \end{bmatrix} \begin{Bmatrix} \boldsymbol{x}_{rigid} \\ \boldsymbol{x}_{struc} \end{Bmatrix} da$$
$$+\bar{q}S\int_a C(k)\left[\boldsymbol{\varphi}_M^l\right]^T \left[\boldsymbol{\lambda}_{6\times6}^{a/l}\right]^T [\mathfrak{L}] \begin{bmatrix} \mathbf{C}_{us}^a \end{bmatrix} \begin{Bmatrix} \boldsymbol{x}_{struc} \end{Bmatrix} da \tag{3.33}$$

Theodorsen function is dependent on the reduced frequency. To remove the dependence on the local chord, a single reference chord length is used[84]. This reference length was selected as the mean aerodynamic chord, $\bar{c}$. This will result in a misrepresentation of the local reduced frequency. The error remains less than the error of a quasi-steady approximation, $C(k) = 1$, over the complete range of reduced frequencies for a ratio of the local chord to mean aerodynamic chord of $0.5 \lesssim \frac{\bar{c}}{c} \lesssim 2.2$. For points outside these limits, the local error will be larger than those for a quasi-steady model. However, the average error over the complete span will be less. By assuming a uniform reduced frequency ($\bar{k}$), Theodorsen function can be removed from the integral. Gauss quadrature is used to evaluate the integral separately for the wing, horizontal tail, and vertical tail. For each of these surfaces $m = 20$ Gauss points, with weights $\mathfrak{w}_i$, was found to provide sufficient accuracy for the integral. The application

of the Gauss quadrature reduces the integral to summations[86].

$$\left[\mathbf{C}^{M}_{rigid}\right] = \sum_{i=1}^{m} \frac{\mathfrak{w}_i}{2b} \left[\boldsymbol{\varphi}^{l}_{M}\right]^{T} \left[\boldsymbol{\lambda}^{a/l}_{6\times6}\right]^{T} [\mathfrak{L}] \left[\begin{array}{c} \mathbf{C}^{a}_{rigid} \end{array}\right] \tag{3.34}$$

$$\left[\mathbf{C}^{M}_{flex}\right] = \sum_{i=1}^{m} \frac{\mathfrak{w}_i}{2b} \left[\boldsymbol{\varphi}^{l}_{M}\right]^{T} \left[\boldsymbol{\lambda}^{a/l}_{6\times6}\right]^{T} [\mathfrak{L}] \left[\begin{array}{c} \mathbf{C}^{a}_{struc} \end{array}\right] \tag{3.35}$$

$$\left[\begin{array}{c} \mathbf{C}^{M}_{us} \end{array}\right] = \sum_{i=1}^{m} \frac{\mathfrak{w}_i}{2b} \left[\boldsymbol{\varphi}^{l}_{M}\right]^{T} \left[\boldsymbol{\lambda}^{a/l}_{6\times6}\right]^{T} [\mathfrak{L}] \left[\begin{array}{c} \mathbf{C}^{a}_{us} \end{array}\right] \tag{3.36}$$

The resulting surrogate model for the complete generalized forces is,

$$\left\{\begin{array}{c} \mathbf{F}^{M} \\ \mathbf{M}^{M} \\ \mathbf{Q}^{M} \end{array}\right\} = \bar{q}Sb \left[\begin{array}{cc} \mathbf{C}^{M}_{rigid} & \mathbf{C}^{M}_{flex} \end{array}\right] \left\{\begin{array}{c} \boldsymbol{x}_{rigid} \\ \dot{\boldsymbol{x}}_{struc} \end{array}\right\} + \bar{q}SbC\left(\bar{k}\right) \left[\begin{array}{c} \mathbf{C}^{M}_{us} \end{array}\right] \left\{\begin{array}{c} \boldsymbol{x}_{struc} \end{array}\right\} \tag{3.37}$$

3.2.3.2 Propulsive Forces

Since the propulsive forces are a concentrated loading, the integral of Eq. 3.30 can be evaluated.

$$\{\mathbf{Q}_e\} = [\boldsymbol{\varphi}^{e}_{M}]^{T} \left\{\begin{array}{c} \mathbf{F}^{e}_{M} \\ \mathbf{M}^{e}_{M} \end{array}\right\} \tag{3.38}$$

$$= [\boldsymbol{\delta}^{e}_{M}]^{T} \{\mathbf{F}^{e}_{M}(t)\} + [\boldsymbol{\theta}^{e}_{M}]^{T} \{\mathbf{M}^{e}_{M}(t)\} \tag{3.39}$$

The loads of Eq. 3.26 are used to complete the generalized forces.

$$
\begin{aligned}
\{\mathbf{Q}_e\} &= [\boldsymbol{\delta}_M^e]^T \begin{Bmatrix} 1 \\ \psi^e \\ -\theta^e \end{Bmatrix} \|\mathbf{F}^e\| + [\boldsymbol{\theta}_M^e]^T \left[\tilde{\mathbf{r}}_M^{\Delta e}\right] \begin{Bmatrix} 1 \\ \psi^e \\ -\theta^e \end{Bmatrix} \|\mathbf{F}^e\| \\
&\quad + [\boldsymbol{\theta}_M^e]^T \left[\tilde{\boldsymbol{\omega}}^M\right] \begin{Bmatrix} 1 \\ \psi^e \\ -\theta^e \end{Bmatrix} \|\mathbf{H}^e\| + [\boldsymbol{\theta}_M^e]^T \begin{Bmatrix} 0 \\ \dot{\psi}^e \\ -\dot{\theta}^e \end{Bmatrix} \|\mathbf{H}^e\| \qquad (3.40)
\end{aligned}
$$

Chapter 4

Adaptive Control

Presently, a model reference adaptive control (MRAC) is used to demonstrate the interaction of the structural dynamics and the dynamics of an adaptive controller. The output feedback direct MRAC scheme based on Tao[87] was selected. The plant is given by the transfer function,

$$\{\mathbf{y}\} = \left([\mathbf{K}_p] \frac{[\mathbf{Z}_p(s)]}{\mathbf{P}_p(s)} ([\mathcal{I}] + [\mathbf{\Delta}_m(s)]) + [\mathbf{\Delta}_a(s)] \right) \{\mathbf{u}\} \tag{4.1}$$

The plant is required to be minimum phase, the zeros have negative real parts, relative degree 1, the difference between the number of poles and the number of zeros, and have a known order. The minimum phase condition is because in order to force the closed-loop system to match the reference model, the controller introduces additional poles to the system which will cancel with the open-loop system's zeros. As a result, to avoid instabilities in the closed-loop system the inputs and outputs must be selected such that the zeros have negative real parts, i.e. minimum phase.

In addition to the plant, a reference model is selected.

$$\{\mathbf{y}_m\} = \left(Z_m(s) [\mathbf{K}_m] [\mathbf{P}_m(s)]^{-1} \right) \{\mathbf{u}\} \tag{4.2}$$

This reference model must be strictly positive real (SPR) such that,

$$\mathrm{Re}\left(Z_m(s)\left[\mathbf{P}_m(s)\right]^{-1}\right) \succ 0 \quad \forall \quad \mathrm{Re}(s) \succ 0 \tag{4.3}$$

This SPR condition requires the system to be minimum phase, the zeros have negative real parts, and stable, the poles have negative real parts. The SPR condition also requires that the system has a relative degree equal to 1.

4.1 Non-Adaptive Model Reference Control

To derive an adaptive controller, we must first consider a non-adaptive controller which will achieve the desired response. In order to reconstruct the states, a filter of order equal to that of the plant, without unmodeled dynamics, is used.

$$\{\mathbf{\Omega}(t)\} = \frac{[\mathbf{A}(s)]}{\Lambda(s)}\left\{\begin{array}{c}\mathbf{u}(t)\\ \mathbf{y}(t)\end{array}\right\} \tag{4.4}$$

$$[\mathbf{A}(s)] = \left[\begin{array}{cccc} s^7\boldsymbol{\mathcal{I}} & s^6\boldsymbol{\mathcal{I}} & \ldots & s\boldsymbol{\mathcal{I}} \quad \boldsymbol{\mathcal{I}}\end{array}\right]^T \tag{4.5}$$

The the estimates of the system states from the observer are an unknown linear combination of these observer filter states. WA control law is defined which uses the filter output and the reference signal to track the output of the reference model[87].

$$\{\mathbf{u}(t)\} = [\mathbf{\Theta}^*]^T\left\{\begin{array}{c}\mathbf{\Omega}(t)\\ \mathbf{y}(t)\\ \mathfrak{r}(t)\end{array}\right\} \tag{4.6}$$

Applying the control law to the system, the resulting closed loop system can be rewritten as a nonminimal statespace realization. The nonminimal realization means that the number of

states is greater then the order of the transfer function.

$$\{\dot{\mathbf{x}}_p\} = [\mathbf{A}_c]\{\mathbf{x}_p\} + [\mathbf{B}_c]\{\mathfrak{r}\} + \{\mathbf{f}(\mathbf{x}_p, \mathfrak{r}, t)\} \tag{4.7}$$

$$\{\mathbf{y}\} = [\mathbf{C}_c]\{\mathbf{x}_p\} \tag{4.8}$$

By applying the control law to the system plant without the unmodeled dynamics, Eqn. 4.1, the resulting closed loop dynamics will be equal to the reference model in Eqn. 4.2. This results in a model matching equation.

$$[\mathbf{\Theta}^*]^T \begin{bmatrix} P_p(s) Z_m(s) \mathbf{A}(s) \\ Z_m(s) \mathbf{A}(s) \mathbf{Z}_p(s) \\ \Lambda(s) P_m(s) \mathbf{Z}_p(s) \\ \Lambda(s) \mathbf{P}_m(s) \mathbf{Z}_p(s) \end{bmatrix} = P_p(s) Z_m(s) \Lambda(s) [\boldsymbol{\mathcal{I}}] \tag{4.9}$$

For this output feedback control law, the model matching equation will be guaranteed as long as the previous assumptions have been satisfied.

4.2 Model Reference Adaptive Control (MRAC)

Defining the tracking error, $\{\mathbf{e}(t)\} = \{\mathbf{y}(t)\} - \{\mathbf{y}_m(t)\}$, and the parameter error, $\left[\tilde{\mathbf{\Theta}}(t)\right] = [\mathbf{\Theta}(t)] - [\mathbf{\Theta}^*]$, the error dynamics for the closed loop system can be rewritten,

$$\{\dot{\mathbf{x}}_e\} = [\mathbf{A}_c]\{\mathbf{x}_e\} + [\mathbf{B}_c][\mathbf{K}_p][\mathbf{K}_m]^{-1}\left[\tilde{\mathbf{\Theta}}(t)\right]^T \{\mathbf{\Omega}(t)\} + \{\mathbf{f}(\mathbf{x}_p, \mathfrak{r}, t)\} \tag{4.10}$$

$$\{\mathbf{e}\} = [\mathbf{C}_c]\{\mathbf{x}_e\} \tag{4.11}$$

Because the reference model is SPR, there exists a solution to the linear Lyapunov equation of the form[88],

$$[\mathbf{A}_c][\mathbf{P}_c] + [\mathbf{P}_c][\mathbf{A}_c]^T = -[\mathbf{Q}_c] \tag{4.12}$$

$$[\mathbf{K}_m][\mathbf{P}_c][\mathbf{B}_c] = [\mathbf{C}_c] \tag{4.13}$$

where $[\mathbf{Q}_c] = [\mathbf{Q}_c]^T \succ 0$ and $[\mathbf{P}_c] = [\mathbf{P}_c]^T \succ 0$. To determine the adaptive law which is used to update the values of $[\mathbf{\Theta}(t)]$ and to prove stability of the adaptive law, it is necessary to first define a candidate Lyapunov function. The candidate Lyapunov function is given by Tao[87],

$$V = \frac{1}{2}\{\mathbf{x}_e(t)\}^T[\mathbf{P}_c]\{\mathbf{x}_e(t)\} + \frac{1}{2}\mathrm{tr}\left(\left[\tilde{\mathbf{\Theta}}(t)\right][\mathbf{S}_p][\mathbf{K}_p][\mathbf{K}_m]^{-1}\left[\tilde{\mathbf{\Theta}}(t)\right]^T\right) \tag{4.14}$$

Where $[\mathbf{S}_p]$ is a known matrix which satisfies the condition:

$$[\mathbf{S}_p][\mathbf{K}_p][\mathbf{K}_m]^{-1} = \left([\mathbf{S}_p][\mathbf{K}_m]^{-1}[\mathbf{K}_p]\right)^T \succ 0 \tag{4.15}$$

Differentiating this Lyapunov function

$$\begin{aligned}\dot{V} = & -\frac{1}{2}\{\mathbf{x}_e(t)\}^T[\mathbf{Q}_c]\{\mathbf{x}_e(t)\} \\ & +\mathrm{tr}\left(\{\mathbf{\Omega}(t)\}^T\left[\tilde{\mathbf{\Theta}}(t)\right][\mathbf{K}_m]^{-T}[\mathbf{K}_p]^T[\mathbf{B}_c]^T[\mathbf{P}_c]^T\{\mathbf{x}_e(t)\}\right) \\ & +\mathrm{tr}\left(\left[\tilde{\mathbf{\Theta}}(t)\right][\mathbf{K}_m]^{-T}[\mathbf{K}_p]^T[\mathbf{S}_p]^T\left[\dot{\tilde{\mathbf{\Theta}}}(t)\right]^T\right) \\ & +\{\mathbf{x}_e(t)\}^T[\mathbf{P}_c]\{\mathbf{f}(\mathbf{x}_p, \mathfrak{r}, t)\}\end{aligned} \tag{4.16}$$

The terms inside the trace can be rearranged.

$$\begin{aligned}\dot{V} = & -\frac{1}{2}\{\mathbf{x}_e(t)\}^T[\mathbf{Q}_c]\{\mathbf{x}_e(t)\} + \mathrm{tr}\left(\left[\tilde{\mathbf{\Theta}}(t)\right][\mathbf{K}_m]^{-T}[\mathbf{K}_p]^T[\mathbf{B}_c]^T[\mathbf{P}_c]^T\{\mathbf{x}_e(t)\}\{\mathbf{\Omega}(t)\}^T\right) \\ & +\mathrm{tr}\left(\left[\tilde{\mathbf{\Theta}}(t)\right][\mathbf{K}_m]^{-T}[\mathbf{K}_p]^T[\mathbf{S}_p]^T\left[\dot{\tilde{\mathbf{\Theta}}}(t)\right]^T\right) + \{\mathbf{x}_e(t)\}^T[\mathbf{P}_c]\{\mathbf{f}(\mathbf{x}_p, \mathfrak{r}, t)\}\end{aligned} \tag{4.17}$$

Applying the second condition in the linear Lyapunov equation,

$$\begin{aligned}\dot{V} &= -\frac{1}{2}\left\{\mathbf{x}_e(t)\right\}^T\left[\mathbf{Q}_c\right]\left\{\mathbf{x}_e(t)\right\} + \mathrm{tr}\left(\left[\tilde{\boldsymbol{\Theta}}(t)\right]\left[\mathbf{K}_m\right]^{-T}\left[\mathbf{K}_p\right]^T\left[\mathbf{K}_m\right]^{-1}\left\{\mathbf{e}(t)\right\}\left\{\boldsymbol{\Omega}(t)\right\}^T\right) \\ &\quad + \mathrm{tr}\left(\left[\tilde{\boldsymbol{\Theta}}(t)\right]\left[\mathbf{K}_m\right]^{-T}\left[\mathbf{K}_p\right]^T\left[\mathbf{S}_p\right]^T\left[\dot{\boldsymbol{\Theta}}(t)\right]^T\right) + \left\{\mathbf{x}_e(t)\right\}^T\left[\mathbf{P}_c\right]\left\{\mathbf{f}(\mathbf{x}_p, \mathfrak{r}, t)\right\} \qquad (4.18)\end{aligned}$$

Rather then solving Eq. 4.9, the gains are updated by the adaptive law of Tao[87].

$$\left[\dot{\boldsymbol{\Theta}}(t)\right]^T = -\left[\mathbf{S}_p\right]^{-T}\left[\mathbf{K}_m\right]^{-1}\left\{\mathbf{e}(t)\right\}\left\{\boldsymbol{\Omega}(t)\right\}^T - \sigma(t)\left[\boldsymbol{\Theta}(t)\right]^T \qquad (4.19)$$

The switching sigma modification term is a function of the Frobenius norm of the control gains, such that the error will converge to zero in the absence of unmodeled dynamics or noise.

$$\sigma(t) = \begin{cases} 0 & \|\boldsymbol{\Theta}(t)\|_F < M \\ \bar{\sigma}\left(\frac{\|\boldsymbol{\Theta}(t)\|_F}{M} - 1\right) & M \le \|\boldsymbol{\Theta}(t)\|_F < 2M \\ \bar{\sigma} & \|\boldsymbol{\Theta}(t)\|_F \ge 2M \end{cases} \qquad (4.20)$$

If the adaptive law is substituted into the Lyapunov rate the equation is simplified.

$$\begin{aligned}\dot{V} &= -\frac{1}{2}\left\{\mathbf{x}_e(t)\right\}^T\left[\mathbf{Q}_c\right]\left\{\mathbf{x}_e(t)\right\} + \left\{\mathbf{x}_e(t)\right\}^T\left[\mathbf{P}_c\right]\left\{\mathbf{f}(\mathbf{x}_p, \mathfrak{r}, t)\right\} \\ &\quad -\sigma(t)\,\mathrm{tr}\left(\left[\tilde{\boldsymbol{\Theta}}(t)\right]\left[\mathbf{K}_m\right]^{-T}\left[\mathbf{K}_p\right]^T\left[\mathbf{S}_p\right]^T\left[\boldsymbol{\Theta}(t)\right]^T\right) \qquad (4.21)\end{aligned}$$

This can be simplified further by applying the norm, and apply the Cauchy–Schwarz inequality. This changes the equation to an inequality and thus increases the conservative nature of any conclusions.

$$\begin{aligned}\dot{V} &\le -\frac{1}{2}\left\|\mathbf{Q}_c\right\|\left\|\mathbf{x}_e(t)\right\|^2 - \sigma(t)\left[\left\|\boldsymbol{\Theta}(t)\right\| - \frac{1}{2}\left\|\mathbf{S}_p\mathbf{K}_p\mathbf{K}_m^{-1}\right\|\left\|\boldsymbol{\Theta}^*\right\|\right]^2 \\ &\quad + \left\|\mathbf{x}_e(t)\right\|\left\|\mathbf{P}_c\right\|\left\|\mathbf{f}(\mathbf{x}_p, \mathbf{z}, t)\right\| + \frac{1}{4}\sigma(t)\left\|\mathbf{S}_p\mathbf{K}_p\mathbf{K}_m^{-1}\right\|^2\left\|\boldsymbol{\Theta}^*\right\|^2 \qquad (4.22)\end{aligned}$$

By the conditions applied to the unmodeled dynamics, $\{\mathbf{f}(\mathbf{x}_p, \mathfrak{r}, t)\}$, they are guaranteed to be bounded input bounded-output (BIBO) stable[89]. Therefore, the resulting disturbance is bounded. Thus the system response is guaranteed to remain bounded. Furthermore, if there is no disturbance, $\|\mathbf{f}(\mathbf{x}_p, \mathfrak{r}, t)\| = 0$, and if the switching sigma modification is defined such that $M > \|[\mathbf{\Theta}^*]\|_F$, then by Barbalat's lemma[90] the error, $\|\mathbf{x}_e(t)\|$, will go to zero.

4.3 Implementation

The adaptive controller has been implemented in the model of the NASA GTM. For the present flight control law, the modeled dynamics used in the design of the controller are restricted to the rigid body dynamics.

$$\{\mathbf{x}\} = \left\{ \begin{array}{cccccccc} u & v & w & p & q & r & \phi & \theta \end{array} \right\}^T \tag{4.23}$$

Blending of the states in the output is used to achieve a system with relative degree 1[1].

$$\{\mathbf{u}\} = \left\{ \begin{array}{ccc} \delta_e & \delta_a & \delta_r \end{array} \right\}^T \tag{4.24}$$

$$\{\mathbf{y}\} = \left\{ \begin{array}{ccc} \phi + p & \theta + q & r \end{array} \right\}^T \tag{4.25}$$

For a linear system the first two outputs are the dynamic pitch and dynamic roll metrics used by Wilborn and Forster[91] for the definition of loss of control. For the flexible aircraft, the multiplicative and additive unmodeled dynamics due to the structure do not have to be minimum phase. Therefore it is not possible for the controller to completely control these dynamics. However, in the absence of aeroelastic instabilities such as flutter or divergence, these dynamics will remain stable. As a result, the structural dynamics, and the resulting error, will remain bounded so long as the control inputs remain bounded.

The poles of the observer filter were selected to correspond to the bandwidth of the

Table 4.1: Control Parameters

Parameter	Value
$[\mathbf{S}_p]$	$2.5 \times 10^3\,[\boldsymbol{\mathcal{I}}]$
$\bar{\sigma}$	0.5
M	3

actuator dynamics.

$$\Lambda(s) = (s + 8\pi)^8 \tag{4.26}$$

The controller was examined for a nominal flexible aircraft and for a very flexible aircraft where the modal stiffness has been scaled by a factor of 0.5. For the simulation, the aircraft has been trimmed to an airspeed of 75 knots at 900 ft. By solving the model matching equation, Eq. 4.9, a non-adaptive controller is derived for comparison to the adaptive controller. To avoid complications associated with model reduction that would be required for determining the solution of the flexible aircraft, the non-adaptive controller is based only on a rigid aircraft. The control gains for the adaptive controller are also initialized at this exact solution, but the errors due to structural interactions still lead to adaptations.

The reference model is selected as the nominal rigid aircraft. The linearization of the model was achieved by a small perturbation method, available in Simulink®, applied to the rigid aircraft model. As was shown in Figure 7.3, the presence of flexibility does result in parametric uncertainty in the rigid body dynamics, which the adaptive control should be able to handle very well. Of more interest is the interaction of the structure with this adaptive control law. The remaining control parameters are shown in Table 4.1. The reference signal was selected as a square wave input with a magnitude of 10° and frequency of 0.1 Hz.

Chapter 5

Scaling Theory

5.1 Full Similitude

The ideal for the scaling of a vehicle is to produce a subscale model which can be related exactly to the fullscale prototype. This exact matching is known as full similitude. To find such a subscale model, first consider a fullscale prototype system with dynamics which are a function of n dimensional parameters, $\lambda_1, \lambda_2, \ldots, \lambda_n$.

$$f(\lambda_1, \lambda_2, \ldots, \lambda_n) = 0 \tag{5.1}$$

Each parameter can be expressed as a product of k fundamental dimensions. Buckingham-Π theory[52, 92] ensures that the total number of parameters of any physical system can be reduced by rewriting in terms of $n - k$ non-dimensional Π groups.

$$\psi(\Pi_1, \Pi_2, \ldots, \Pi_{n-k}) = 0 \tag{5.2}$$

For an aircraft there are three dimensions, expressed as length, time, and either mass or force, and thus $k = 3$. These Π groups are of the form,

$$\Pi = \prod_{i=1}^{n} \lambda_i^{\gamma_i} \tag{5.3}$$

The dimension of the parameter λ_i can be expressed as the product $\lambda_i = M^{\alpha_i} L^{\beta_i} T^{\delta_i}$. For the Π groups to be dimensionless the exponents must satisfy Eqn. 5.4.

$$\begin{bmatrix} \alpha_1 & \alpha_2 & \cdots & \alpha_n \\ \beta_1 & \beta_2 & \cdots & \beta_n \\ \delta_1 & \delta_2 & \cdots & \delta_n \end{bmatrix} \begin{Bmatrix} \gamma_1 \\ \gamma_2 \\ \vdots \\ \gamma_n \end{Bmatrix} = \begin{Bmatrix} 0 \\ 0 \\ 0 \end{Bmatrix} \tag{5.4}$$

The exponents of the Π groups are defined by the nullspace of this matrix. For any system with more than k dimensional parameters, the selection of the nullspace is not unique. Therefore, the number of distinct non-dimensional Π groups is fixed, but the definition of these parameters is not unique.

The scaling laws for each dimension can be selected arbitrarily. Then the dimensional parameters of the model are determined by applying this scaling to the parameters' dimensions. More often the scaling laws are determined by selecting k dimensional parameters which are fixed or have a fixed scaling. The scaling of each dimension can then be determined such that the non-dimensional Π groups of the model are identical to the prototype. Since the Π groups of the model and the prototype are identical, the dynamics of both systems are the same in the nondimensional space even though the scale of the systems differs.

It should be noted that the determination of the Π groups depends only on the parameters which describe the system and not the form of the equations. As a result, the scaling laws from complete similitude are valid on linear as well as non-linear systems.

5.1.1 Aircraft Parametrization

Complete similitude does not require the equations of motion, only knowledge of the parameters which describe the physics. By assuming a linear structure, Waszak and Schmidt[15] derive the kinetic energy, T, potential energy, U, and virtual work, $\overline{\delta W}$, of a flexible aircraft. They used a mean axis system which simplifies the expressions.

$$T = \frac{1}{2}m\mathbf{v}^T(t)\,\mathbf{v}(t) + \frac{1}{2}\boldsymbol{\omega}^T(t)\,\mathbf{I}(t)\,\boldsymbol{\omega}(t) + \frac{1}{2}\sum_{i=1}^{\infty} m_i\xi_i^2(t) \tag{5.5}$$

$$U = -mg\left[-x\sin\theta + y\sin\phi\cos\theta + z\cos\phi\cos\theta\right] + \frac{1}{2}\sum_{i=1}^{\infty} m_i\omega_i^2\xi_i^2(t) \tag{5.6}$$

$$\overline{\delta W} = \mathbf{F}^T(\rho,V,\nu)\,\delta\mathbf{r} + \mathbf{M}^T(\rho,V,\nu)\,\delta\boldsymbol{\theta} + \sum_{i=1}^{\infty}\left[Q_i(\rho,V,\nu) - \zeta_i\dot{\xi}_i\right]\delta\xi_i \tag{5.7}$$

The details of these dimensional parameters for the flexible aircraft are given in Table 5.1. Although the energy in Eqns. 5.5, 5.6, and 5.7 are based on a mean axis formulation, the equivalent parameters for a fixed axis system will have identical dimensions. The used of a fixed axis system would only introduce additional terms to the energy equations, without adding additional parameters[14]. Because the complete similitude is independent of the form of the equations, the complete similitude will be applicable for whichever axis system is used to describe the dynamics of the system.

5.1.2 Scaling Laws

By considering non-dimensional parameters, the number of system parameters is reduced by three, the number of dimensions for the current system. Therefore, it is possible to select three independent scaling parameters. The first parameter is a geometric scaling parameter, γ, which is given as the ratio of the lengths for the model (subscale) to the prototype (full-scale). For example, this can be defined as the ratio of the mean aerodynamic chords. The second scaling parameter is selected as the ratio of these two air densities, ϱ. This is necessary because the model operates at a different altitude from the prototype. The

Table 5.1: Dimensional Parameters for a Flexible Aircraft

Type	Parameter	Symbol	Dimension	Scaling
States	Time	t	T	$\sqrt{\gamma}$
	Position	$\mathbf{r}$	L	γ
	Velocity	$\mathbf{v}$	LT^{-1}	$\sqrt{\gamma}$
	Angular Velocity	$\boldsymbol{\omega}$	T^{-1}	$\frac{1}{\sqrt{\gamma}}$
	Euler Angles	$\boldsymbol{\theta}$	–	–
	Modal Displacement	ξ	–	–
Geometric	Chord	$\bar{c}$	L	γ
	Span	b	L	γ
	Planform Area	S	L^2	γ^2
Inertial	Aircraft Mass	m	M	$\varrho\gamma^3$
	Moment of Inertia	I	ML^2	$\varrho\gamma^5$
	Gravitational Acceleration	g	LT^{-2}	–
Structural	Modal Mass	m_i	ML^2	$\varrho\gamma^4$
	Modal Damping	ζ_i	–	–
	Frequency of Mode	ω_i	T^{-1}	$\frac{1}{\sqrt{\gamma}}$
Aerodynamic	True Airspeed at Trim	V_0	LT^{-1}	$\sqrt{\gamma}$
	Air density	ρ	ML^{-3}	ϱ
	Air viscosity	ν	L^2T^{-1}	$\gamma\sqrt{\gamma}$
	Speed of Sound	a	LT^{-1}	$\sqrt{\gamma}$
	Aerodynamic Force	$\mathbf{F}$	MLT^{-2}	$\varrho\gamma^3$
	Aerodynamic Moment	$\mathbf{M}$	ML^2T^{-2}	$\varrho\gamma^4$
	Aerodynamic Modal Force	$\mathbf{Q}$	ML^2T^{-2}	$\varrho\gamma^4$

difference in altitude results in a different air density. The final constraint for the scaling is that the acceleration due to gravity is equal for the two vehicles. Considering the parameters of the subscale model, shown by the subscript m, and the full-scale prototype, shown by the subscript p, the scaling parameters can be written:

$$\gamma \triangleq \frac{\bar{c}_m}{\bar{c}_p} = \frac{L_m}{L_p} \tag{5.8}$$

$$\varrho \triangleq \frac{\rho_m}{\rho_p} = \frac{M_m L_m^{-3}}{M_p L_p^{-3}} \tag{5.9}$$

$$1 \triangleq \frac{g_m}{g_p} = \frac{M_m T_m^{-2}}{M_p T_p^{-2}} \tag{5.10}$$

Using these scaling parameters, each dimension will have the following scaling:

$$\frac{M_m}{M_p} = \varrho\gamma^3 \tag{5.11}$$

$$\frac{L_m}{L_p} = \gamma \tag{5.12}$$

$$\frac{T_m}{T_p} = \sqrt{\gamma} \tag{5.13}$$

The scaling can then be applied to the dimensions for each dimensional parameter, giving the scaling shown in Table 5.1. The complete application of these scaling laws will ensure complete similitude between the model and the prototype. Furthermore, the similitude is valid for non-linear dynamics, assuming that the parameters presented in Table 5.1 represent a complete set of all the system's parameters.

5.1.3 Aircraft Π Groups

The scaling laws provide a means to determine the parameters of the subscale model. In order to relate the results from the subscale vehicle to the fullscale prototype, the Π groups must also be determined. Where possible, the Π groups have been selected to match the non-dimensional parameters given by Wolowicz, Bowman, and Gilbert[53]. The resulting

Table 5.2: Non-dimensional Parameters for a Flexible Aircraft

Scaling Type	Parameter	Symbol	Value
Geometric	Aspect Ratio	AR	$\frac{b}{\bar{c}}$
Dynamic	Non-dimensional Time	τ	$\frac{2tV_0}{\bar{c}}$
	Velocity	$\hat{V}$	$\frac{V_T}{V_0}$
	Angle of Attack	α	—
	Non-dimensional Pitch Rate	$\hat{q}$	$\frac{q\bar{c}}{2V_0}$
	Euler Angles	$\boldsymbol{\theta}$	—
	Mass Ratio	μ	$\frac{2m}{S\bar{c}\rho}$
	Non-dimensional Inertia	$\hat{I}_{yy}$	$\frac{8I_{yy}}{S\bar{c}^3\rho}$
	Froude Number	Fr	$\frac{V_T}{\sqrt{\bar{c}g}}$
Structural (Constitutive)	Modal Mass Ratio	μ_i	$\frac{4m_y}{S\bar{c}^2\rho}$
	Modal Damping	ζ_i	—
	Reduced Frequency of Mode	k_i	$\frac{\omega_y\bar{c}}{2V_0}$
	Modal Displacement	ξ_i	—
Aerodynamic	Reynolds Number	Re	$\frac{V_0\bar{c}}{\nu}$
	Mach Number	M	$\frac{V_0}{a}$
	Force Coefficient	C_F	$\frac{2F}{\rho V_0^2 S}$
	Moment Coefficient	C_M	$\frac{2M}{\rho V_0^2 S\bar{c}}$
	Modal Force Coefficient	C_Q	$\frac{2M}{\rho V_0^2 S\bar{c}}$

Π groups are shown in Table 5.2. Many of these parameters are commonly seen in non-dimensional analysis of the independent aircraft disciplines. For example, the Reynolds number, often appears in the aerodynamics and represents the ratio of the inertial to the viscous forces. This is important for correctly capturing the viscous forces and for post-stall conditions. However, because it is very difficult to match this correctly, these effects are often simulated by adding roughness to the leading edge of the wing to simulate the flow separation due to the viscous effects.

The Mach number, which represents the ratio of the inertial to pressure forces, is important for capturing the effects of the compressibility of the air. Similarly, the Froude number, which is the ratio of the inertial to the gravitational forces, is an important parameter for matching the flight dynamics. It is difficult to match both the Mach number and the Froude

number. In windtunnel tests the use of heavy gases can make matching possible. For flight testing this is not possible. As a result it is necessary to choose one of these parameters to be neglected. For the present work the compressibility effects, and thus Mach number, have been considered to be less important.

The relative density factor and relative mass moment of inertia are important for both the flight dynamics and the aeroelastic response. These parameters are important for correctly capturing the aerodynamic forces relative to the aircraft's mass.

5.2 Partial Similitude

For a complex system, such as an aircraft, it is impractical or even impossible to achieve complete similitude. One limitation is the atmospheric properties. For example, air density, the speed of sound, and viscosity are fixed for a given altitude so only one can be matched for the scaling. The matching of the structure is also limited by the materials used. For example, the Young's modulus, E, and shear modulus, G, are determined by material selection. As a result, matching the nondimensional stiffness parameters requires changing the material, which may not have sufficient strength, or modifying the subscale model's structure. As result of these effects, designing a vehicle which matches all of the non-dimensional parameters can be prohibitively expensive and involved, if not impossible. Thus, it is necessary to determine which of these parameters are most important to the system response. The resulting partial matching is known as partial similitude.

To facilitate this goal of reducing the number of parameters, the desire is to focus only on a portion of the overall dynamics. Because the coupling of the short-period mode and the first wing bending mode is most significant for the present applications, the scaling laws are considered such that these modes will match between the fullscale and subscale.

To examine these effects, it is necessary to apply a structure to the dynamics and define the equations of motion. For the present work, the effects of Reynolds number and Mach

number are neglected immediately. This is considered an acceptable assumption because these are parameters commonly neglected in both low speed flight dynamics and aeroelasticity testing. The aerodynamic forces are assumed to be a linear function of the non-dimensional states.

$$C_D = C_{D_0} + C_{D_\alpha}\alpha + C_{D_\delta}\delta + C_{D_\xi}\xi_i + C_{D_{\dot{\xi}}}\overset{*}{\xi}_i + C_{D_q}\hat{q} + C_{D_{\dot{\alpha}}}\overset{*}{\alpha} - C_{X_T}\hat{T}\cos\alpha \quad (5.14)$$

$$C_L = C_{L_0} + C_{L_\alpha}\alpha + C_{L_\delta}\delta + C_{L_\xi}\xi_i + C_{L_{\dot{\xi}}}\overset{*}{\xi}_i + C_{L_q}\hat{q} + C_{L_{\dot{\alpha}}}\overset{*}{\alpha} + \frac{1}{2}C_{X_T}\sin\alpha \quad (5.15)$$

$$C_m = C_{m_0} + C_{m_\alpha}\alpha + C_{m_\delta}\delta + C_{m_\xi}\xi_i + C_{m_{\dot{\xi}}}\overset{*}{\xi}_i + C_{m_q}\hat{q} + C_{m_{\dot{\alpha}}}\overset{*}{\alpha} + C_{m_T}\hat{T} \quad (5.16)$$

$$C_Q = C_{\xi_0} + C_{\xi_\alpha}\alpha + C_{\xi_\delta}\delta + C_{\xi_\xi}\xi_i + C_{\xi_{\dot{\xi}}}\overset{*}{\xi}_i + C_{\xi_q}\hat{q} + C_{\xi_{\dot{\alpha}}}\overset{*}{\alpha} \quad (5.17)$$

The structural motion is assumed to be small. As a result, the structural dynamics are linear and the aircraft's moments of inertia are approximately constant. For the present work, the primary interest is in the dynamics of the system, not the equilibrium. The equilibrium is removed by considering a perturbation from the trim. These perturbations are also assumed to be small resulting in the linearized equations of motion.

$$[\mathbf{M}]\left\{\delta\overset{*}{\mathbf{x}}\right\} = [\mathbf{A}]\{\delta\mathbf{x}\} + [\mathbf{B}]\{\delta\mathbf{u}\} \quad (5.18)$$

The nondimensional parameters in Table 5.2 were applied to the mean axis system equations of motion presented by Waszak and Schmidt[15]. The perturbation equations for coupled flight dynamics and aeroelasticity also decouple into longitudinal, including symmetric structural modes, and lateral, including antisymmetric structural modes. For the longitudinal

motion, $\{\mathbf{x}\} = \left\{ \begin{array}{cccccc} \hat{V} & \alpha & \hat{q} & \theta & \overset{*}{\xi}_i & \xi_i \end{array} \right\}$, these matrices are:

$$[\mathbf{M}] = \begin{bmatrix} \mu & \frac{1}{2}C_{D_{\dot{\alpha}}} & 0 & 0 & 0 & 0 \\ 0 & \mu + \frac{1}{2}C_{L_{\dot{\alpha}}} & 0 & 0 & 0 & 0 \\ 0 & -C_{m_{\dot{\alpha}}} & \hat{I}_{yy} & 0 & 0 & 0 \\ 0 & 0 & 0 & 1 & 0 & 0 \\ 0 & -\frac{1}{2}C_{\xi_{\dot{\alpha}}} & 0 & 0 & \mu_i & 0 \\ 0 & 0 & 0 & 0 & 0 & 1 \end{bmatrix} \tag{5.19}$$

$$[\mathbf{A}] = \begin{bmatrix} -C_{D_0} & -\frac{1}{2}C_{L_0} - \frac{1}{2}C_{D_\alpha} & -\frac{1}{2}C_{D_q} & -\frac{\mu}{\mathrm{Fr}} & -\frac{1}{2}C_{D_{\dot{\xi}}} & -\frac{1}{2}C_{D_\xi} \\ -C_{L_0} & \frac{1}{2}C_{D_0} - \frac{1}{2}C_{L_\alpha} & \mu - \frac{1}{2}C_{L_q} & 0 & -\frac{1}{2}C_{L_{\dot{\xi}}} & -\frac{1}{2}C_{L_\xi} \\ 2C_{m_0} & C_{m_\alpha} & C_{m_q} & 0 & C_{m_{\dot{\xi}}} & C_{m_\xi} \\ 0 & 0 & 1 & 0 & 0 & 0 \\ C_{\xi_e} & \frac{1}{2}C_{\xi_\alpha} & \frac{1}{2}C_{\xi_q} & 0 & \frac{1}{2}C_{\xi_{\dot{\xi}}} - 2\mu_i\zeta_i k_i & \frac{1}{2}C_{\xi_\xi} - \mu_i k_i^2 \\ 0 & 0 & 0 & 0 & 1 & 0 \end{bmatrix} \tag{5.20}$$

$$[\mathbf{B}] = \begin{bmatrix} \frac{1}{2}C_{X_T}\cos\alpha_0 & -\frac{1}{2}C_{D_{\delta_e}} \\ -\frac{1}{2}C_{X_T}\sin\alpha_0 & -\frac{1}{2}C_{L_{\delta_e}} \\ C_{m_T} & C_{m_{\delta_e}} \\ 0 & 0 \\ 0 & \frac{1}{2}C_{\xi_{\delta_e}} \\ 0 & 0 \end{bmatrix} \tag{5.21}$$

The perturbation equations do not completely remove the effects of the equilibrium. The equilibrium angle of attack, α_0, and the aerodynamic coefficients at equilibrium, C_{D_0}, C_{L_0}, and C_{m_0}, are present in the perturbation equations. Since these are the only 4 parameters dependent on the equilibrium, the importance of the equilibrium is reduced by considering the linear dynamics.

The non-dimensional parameters for the flexible transport of Waszak and Schmidt[16, 15] are given in Tables 5.3 and 5.4.

Table 5.3: Non-dimensional Parameters of a Flexible Transport

Scaling Type	Parameter	Symbol	Value
Geometric	Aspect Ratio	AR	9.150
Dynamic	Mass Ratio	μ	293.4
	Non-dimensional Inertia	$\hat{I}_{yy}$	3587
	Froude Number	Fr	1759
Structural	Modal Mass Ratio	μ_1	0.7871
(Constitutive)	Modal Damping	ζ_1	0.02
	Reduced Frequency of Mode	k_1	0.07302

Table 5.4: Aerodynamic Coefficients of a Flexible Transport

C_D		C_L		C_m		C_ξ	
C_{D_0}	6.007×10^{-2}	C_{L_0}	-0.3321	C_{m_0}	-0.01250	C_{ξ_0}	3.421×10^{-2}
C_{D_α}	-1.326×10^{-1}	C_{L_α}	2.926	C_{m_α}	-1.662	C_{ξ_α}	-2.279×10^{-1}
$C_{D_{\dot{\alpha}}}$	0.0	$C_{L_{\dot{\alpha}}}$	0.0	$C_{m_{\dot{\alpha}}}$	-4.3	$C_{\xi_{\dot{\alpha}}}$	0.0
C_{D_q}	-1.358	C_{L_q}	-14.74	C_{m_q}	-34.75	C_{ξ_q}	-1.452
C_{D_δ}	-2.493×10^{-3}	C_{L_δ}	0.007660	C_{m_δ}	-0.045	C_{ξ_δ}	-3.427×10^{-3}
C_{D_ξ}	6.692×10^{-4}	C_{L_ξ}	0.02879	C_{m_ξ}	-0.0321	C_{ξ_ξ}	8.951×10^{-4}
$C_{D_{\dot{\xi}}}$	1.970×10^{-3}	$C_{L_{\dot{\xi}}}$	0.08478	$C_{m_{\dot{\xi}}}$	-0.159	$C_{\xi_{\dot{\xi}}}$	-6.426×10^{-3}

Table 5.5: Classical Short-Period Approximation[1, 2]

Short-Period	
$\delta\hat{V} \approx 0$	$\delta\hat{V} \approx 0$
$\delta\alpha \neq 0$	$\delta\alpha \neq 0$
$\delta\hat{q} \neq 0$	$\delta\hat{q} \neq 0$
$\delta\theta \approx 0$	$\delta\theta \approx 0$

5.2.1 Model Reduction

It is possible to create a reduced order model of the classical flight modes by focusing on the dominant motions of the modes. These approximations are shown in Table 5.5. The short-period mode is dominated by variations in the angle of attack and the pitch rate. Since the frequency of the pitching motion is high the magnitude of the variation in the pitch angle remains small. Therefore, the short period mode can be approximated by truncating the dynamics associated with the forward velocity and the pitch angle. The approximation of the Phugoid mode is more complicated because the less significant pitch rate is still important for the forcing that they provide. These require a more complicated residualization of the dynamics. For example, with the Phugoid mode $\dot{\hat{q}} \approx 0$ but $\delta\hat{q} \neq 0$. The resulting expressions are too long for a clear interpretation using the present method. Fortunately, these modes are of a very low frequency, and are thus less likely to lead to a significant coupling with structural modes. Therefore, these modes are not considered in the present analysis.

Applying the short-period approximation shown in Table 5.5 to the perturbation Eqns.

5.19 and 5.20 gives the reduced short-period Eqns. 5.22 and 5.23.

$$[\mathbf{M}_{sp}] = \begin{bmatrix} \mu + \frac{1}{2}C_{L_{\dot{\alpha}}} & 0 & 0 & 0 \\ -C_{m_{\dot{\alpha}}} & \hat{I}_{yy} & 0 & 0 \\ -\frac{1}{2}C_{\xi_{\dot{\alpha}}} & 0 & \mu_i & 0 \\ 0 & 0 & 0 & 1 \end{bmatrix} \tag{5.22}$$

$$[\mathbf{A}_{sp}] = \begin{bmatrix} \frac{1}{2}C_{D_0} - \frac{1}{2}C_{L_\alpha} & \mu - \frac{1}{2}C_{L_q} & -\frac{1}{2}C_{L_{\dot{\xi}_z}} & -\frac{1}{2}C_{L_\xi} \\ C_{m_\alpha} & C_{m_q} & C_{m_{\dot{\xi}_z}} & C_{m_\xi} \\ \frac{1}{2}C_{\xi_\alpha} & \frac{1}{2}C_{\xi_q} & \frac{1}{2}C_{\xi_{\dot{\xi}}} - 2\mu_i\zeta_i k_i & \frac{1}{2}C_{\xi_\xi} - \mu_i k_i^2 \\ 0 & 0 & 1 & 0 \end{bmatrix} \tag{5.23}$$

By applying the classical approximation of the short-period mode there is a simplification of the system dynamics. However, the validity of these approximations is uncertain in the presence of structural flexibility. The approximations assume the effects of the structure are small. As such, it is possible for the interaction of the structural modes to affect the mode shapes and thus change the approximations that should be used. It is also unclear if the structural effects are greater than the effects of the truncated dynamics.

5.2.2 Sensitivity

To address the limitations of the model reduction, the sensitivity of the system response is also examined. The sensitivity shows how small changes in the parameters, will effect the response of the vehicle. To remove the ambiguity of the input design, the frequency response of the system is considered. Due to the use of non-dimensional parameters, this is the reduced frequency domain. Similar to the mismatch shown in the low frequencies in Figure 7.7, the separate modes can be identified by focusing on specific bandwidth. For partial similitude, the parameters of the subscale vehicle, $\{\mathbf{\Pi}_m\}$, will differ from the parameters of the fullscale vehicle, $\{\mathbf{\Pi}_p\}$. The non-dimensional parameters in Table 5.3 vary significantly in magnitude. To allow a direct comparison of the changes in the parameters, the difference

of the parameters is normalized by considering a percent change, $\left\{\widehat{\delta\mathbf{\Pi}}\right\}$, in the fullscale vehicle's parameters.

$$\Pi_{m_i} = \Pi_{p_i} + \Pi_{p_i}\widehat{\delta\Pi_i} \tag{5.24}$$

The transformation of the non-dimensional time domain equations to the reduced frequency domain is given in Eqn. 5.25.

$$\{\mathbf{H}(k,\mathbf{\Pi})\} = [ik\mathbf{M}(\mathbf{\Pi}) - \mathbf{A}(\mathbf{\Pi})]^{-1}\{\mathbf{b}(\mathbf{\Pi})\} \tag{5.25}$$

If the variation in the subscale model parameters is small, the reduced frequency response is approximated as a function of the nominal fullscale vehicle parameters, $\{\mathbf{\Pi}_p\}$.

$$\{\mathbf{H}(k,\mathbf{\Pi}_m)\} \approx \{\mathbf{H}(k,\mathbf{\Pi}_p)\} + \left[\widehat{\nabla_{\mathbf{\Pi}}\mathbf{H}}(k,\mathbf{\Pi}_p)\right]\left\{\widehat{\delta\mathbf{\Pi}}\right\} \tag{5.26}$$

The normalized sensitivities, $\left[\widehat{\nabla_{\mathbf{\Pi}}\mathbf{H}}(k,\mathbf{\Pi}_p)\right]$, are given by:

$$\left[\widehat{\nabla_{\mathbf{\Pi}}\mathbf{H}}(k,\mathbf{\Pi}_p)\right]_{i,j} = \Pi_{p_i}\frac{\partial}{\partial\Pi_j}\mathbf{H}(k,\mathbf{\Pi}_p) \tag{5.27}$$

Although it is possible to calculate these sensitivities analytically, numerical data is required to interpret the results. As long as there is numerical data available for a vehicle, the sensitivities will illustrate the relative effect of each parameter on the system's response. Thus, the parameters will a small effect can be neglected in creating a vehicle which will achieve partial similitude.

Chapter 6

Flight Testing

Although the theoretical analysis offers significant advantages to examining the interactions between the flight dynamics and the structural dynamics, it is necessary to validate the theory by experiment. The response of the two vehicles are compared to further illustrate the coupling between the structural dynamics and the flight dynamics.

The goal of the current flight testing is to create a subscale vehicle which demonstrates coupling between the structure and the flight dynamics. The coupling is examined by doing system identification. The identified models are studied for the increased effects of Froude number on a more flexible vehicle as was seen in the examination of the scaling laws.

6.1 Experiment Configuration

A Sig Rascal 110 was selected to be used in the flight tests. However, as with many R/C aircraft, the wing on the Sig Rascal, Figure 6.1a, is quite stiff and does not show significant ASE interactions. To have an aircraft with significant ASE interactions, the wing of the Rascal was replaced with a more flexible version, Figure 6.1b. The new wing was designed to maintain the same aspect ratio and total span. The undeformed dihedral, $\approx 2^1/_2^\circ$, was also retained for the flexible wing. However, the elliptical shape of the wing was changed in favor

(a) Commercial Off-The-Shelf

(b) Aeroservoelastic Wing

Figure 6.1: Sig Rascal 110

Figure 6.2: Kentland Experimental Aerial Systems (KEAS) Laboratory

of a rectangular wing. The rectangular wing was selected for ease of construction and ease of analysis of the structure. The flight tests were performed at the Kentland Experimental Aerial Systems (KEAS) Laboratory, shown in Figure 6.2. This facility offers a paved 300ft runway for the flight tests.

6.1.1 Sensors

The sensors were selected to provide measurement of the longitudinal rigid body flight dynamics (2 linear accelerations and 1 angular velocity), structural deflections (wing strain),

aircraft velocity (dynamic pressure), and control deflections (elevator angle). The data was sampled at 100Hz, and an anti-aliasing filter with a cutoff frequency of 10Hz was used. These were selected to be much higher then the expected frequencies that were being examined in the flight tests. These anti-aliasing filters are a passive first order analog filter.

6.1.1.1 Data Acquisition and Logging

To measure and record the output of the sensors, a DATAQ Instruments DI-710-UHS stand-alone data logger was used. This system allowed an accurate (14-bit A/D converter) measurement of the sensor voltages that were recorded on an onboard SD card that could be retrieved after landing for analysis. The onboard logging was selected to avoid the complications of implementing a wireless data link from the aircraft to a ground station and the data delays that also result from such a system.

6.1.1.2 Inertial Measurement Unit

Off-the-shelf inertial measurement units (IMUs) typically contain filters which improve their performance and ease of use in applying them to the vehicle. These filters are designed so that the IMU accurately captures the flight dynamic motion. The structural dynamics, which are a major concern in the present experiments, are often at a frequency well above the filter cutoff frequency of these IMUs. As a result, it was necessary to create a new IMU which uses a set of accelerometers and gyros which do not have these filters. An STMicroelectronics LIS334ALH accelerometer was selected for the IMU. This accelerometer offers measurements in 3-axis, and a selectable range of $\pm$2g or $\pm$6g. For these tests the $\pm$6g range was used. To record the angular accelerations, an STMicroelectronics LPR410AL gyro was used. Because only the longitudinal dynamics were of interest for the present testing, this 2-axis accelerometer was sufficient. The accelerometer offers a measurement range of $\pm 100^{\mathrm{deg}}/_{\mathrm{s}}$.

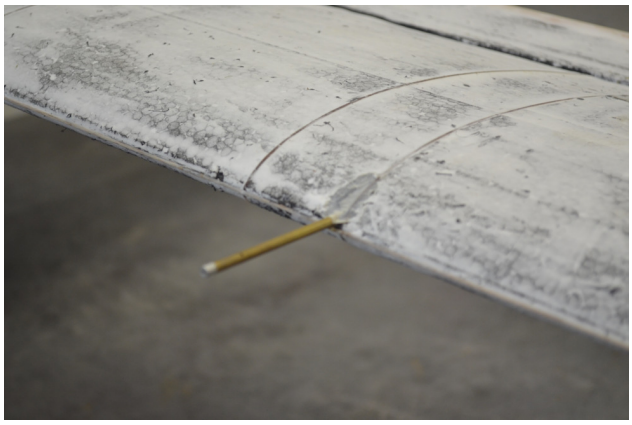

Figure 6.3: Pitot Tube

6.1.1.3 Structural Measurement

The measurement of the structural measurements were provided by Micro-Measurements CEA-06-250UN-350 strain gages. These gages were mounted only to the flexible wing. They were mounted on the main spar (aluminum) and leading edge spar (balsa). They were mounted in a half-bridge configuration, one gage on the top and one on the bottom, which provides increase sensitivity and temperature compensation. They were mounted close to the root where the strain would be greatest. A custom Wheatstone bridge completion circuit was built using $100 \pm 1\text{k}\Omega$ resistors. Amplification of the bridge output was provided by a Texas Instruments INA2126 instrumentation amplifier.

6.1.1.4 Pitot Tube

The airspeed of the aircraft is needed for non-dimensionalization of the system. This measurement is calculated from the dynamic pressure measured by a pitot tube on the wing of the aircraft. The tube was located on the wing to isolate it from the air disturbed by the propeller. Flexible tubing was run from the sensor to the fuselage where a Freescale Semiconductor MPXV7002DP differential pressure sensor provided the dynamic pressure. The static pressure was measured from within the fuselage.

6.1.1.5 Control Deflections

The standard servo used in R/C aircraft is actually a closed loop system. There is an onboard potentiometer which records the rotation of the servo. Normally, there is no output from the servo that could be read by the data logger. Instead, an extra pair of lead wires were attached to the potentiometer inside the servo. The addition of these new leads can lead to issues if there is even a very small voltage applied. The data logger or noise on the long lead wires can cause a voltage which will disrupt the potentiometer reading. Since the elevator servo is a flight critical piece of hardware, it was necessary to isolate the servo from the data logger. The isolation was accomplished using a voltage follower. A voltage follower is an operational amplifier with a gain of 1. Thus the amplifier outputs the same voltage from the potentiometer, but does not allow any other sources to apply a voltage to the potentiometer.

6.1.2 Flexible Wing Design

The new wing for the Sig Rascal must be strong enough to support the flight loads, light enough to fly, and flexible enough to exhibit significant interactions with the flight dynamics. For the strength and weight requirements, a detailed model is created in Inventor. For the final requirement, the earlier modeling is used. However, this requires the data to be in the form of a simple beam.

6.1.2.1 Design Concept

An illustration of the wing structure is given in Figure 6.4.

The main strength of the wing is provided by an aluminum spar. Moving the spar allowed for tailoring the elastic axis of the wing. A thin balsa spar was applied to the leading and trailing edges to provide reinforcement of the edges and to increase for-aft bending stiffness. The foam was applied around these spars to give the wing its aerodynamic shape. The

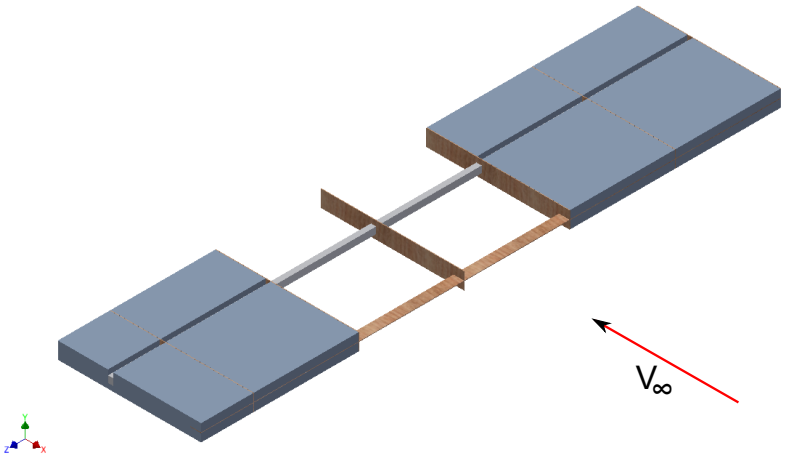

Figure 6.4: Wing Structure Concept

basswood ribs between the foam sections were included to increase the chordwise stiffness and to ensure the load is transferred from the foam to the main spar.

6.1.2.2 Flexibility Requirement

To examine the effect of the flexibility the beam stiffness must be reduced to equivalent beam properties. The properties of the wing are assumed to be uniform for these equivalent properties. The presence of the ribs violates this assumption. Bisplinghoff et al.[84] showed that such an approximation can still provide a good approximation of the beam as long as there are a sufficient number of ribs. Three separate loading cases were used to determine the properties. Only two are required, but the third case provides a verification of the properties. For each of these cases a load was applied to the leading edge, mid chord, and trailing edge respectively. Since the actual loading will be distributed along the span, the load was distributed uniformly along the span. A tip load would not show the strain energy absorbed by the foam sections, and the uniform load still provides an analytical solution for the deflections of a uniform beam about the elastic axis, the line along which the bending

and torsion are decoupled[93].

$$w\left(\frac{b}{2}\right) = \frac{Fb^3}{16EI} \tag{6.1}$$

$$\theta\left(\frac{b}{2}\right) = \frac{Mb}{2GJ} \tag{6.2}$$

The first step to determining the beam properties is to determine the elastic axis, since this is where the the Analytical equations are given. The location of the elastic axis is determined by the intercept of a line fit to the location of the applied load versus the angle of twist. The deflection and the angle of twist at the elastic axis are substituted into Eqns. 6.1 and 6.2 to determined the bending and torsional stiffness, EI and GJ. Inventor will directly provide the inertial properties required to fully define the structural dynamics.

6.1.2.3 Strength and Weight Requirements

The wing has been designed to withstand a maneuver that produces a load factor of 3. To determine the loads on the wing during such a maneuver, the vortex lattice model in AVL was used. The aircraft conditions were set to a 3g pull-up maneuver. AVL then provides the total force on the wing. Since the current wing is designed to show significant aeroelastic coupling and is unswept, the effects of divergence are likely to be significant. To include these effect of the divergence in the aerodynamic loads, a strip theory was applied to a Euler-Bernoulli beam wing[84].

$$\begin{bmatrix} EI & 0 \\ 0 & GJ \end{bmatrix} \begin{Bmatrix} w''''(y) \\ \theta''(y) \end{Bmatrix} = \begin{bmatrix} 0 & 2\pi qc \\ 0 & 2\pi qc^2 e \end{bmatrix} \begin{Bmatrix} w(y) \\ \theta(y) \end{Bmatrix} + \begin{Bmatrix} 2\pi qc\alpha_0 \\ 2\pi qc^2 e\alpha_0 \end{Bmatrix} \tag{6.3}$$

with the boundary conditions:

$$w'''\left(\frac{b}{2}\right) = 0 \tag{6.4}$$

$$w''\left(\frac{b}{2}\right) = 0 \tag{6.5}$$

$$w'(0) = 0 \tag{6.6}$$

$$w(0) = 0 \tag{6.7}$$

$$\theta'\left(\frac{b}{2}\right) = 0 \tag{6.8}$$

$$\theta(0) = 0 \tag{6.9}$$

The initial angle of attack, α_0, is selected so that the total load on the wing will give a net force equal to the results of the pull-up maneuver in AVL. This strip theory does not account for the elliptical lift distribution. Therefore, the loading at the tip and the wing root bending moment will be greater. Since the wing root bending moment is the limiting factor for the present wing, the resulting determination of safety factors are a conservative estimate. The stiffness properties are taken from the equivalent beam properties found in section 6.1.2.2. The forces were applied to the Inventor model as a force and moment uniformly distributed on each foam segment. The load on each segment matches the force from Eqn 6.3.

From the BCAR airworthiness requirements in Megson[94], the aircraft must have a factor of safety of 1.25 in yield and a factor of safety of 1.5 for failure during such a 3g maneuver.

6.1.3 Detailed Design

In addition to the simple model used for the preliminary conceptual design, a more detail model, shown in Figure 6.5, was used to test the design.

The detailed design matches the wing as built. This detailed model included the correct airfoil shape as well as the the aileron and servo assemblies. Due to the more complex geometry, a uniform loading was used for the detailed design. The cad models of wooden

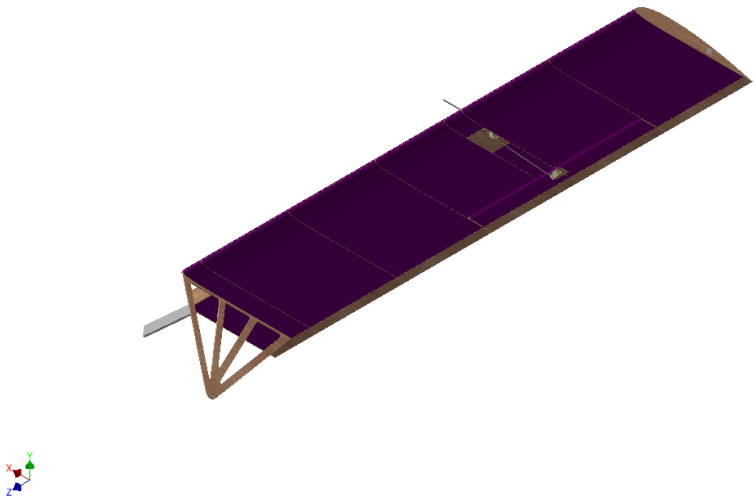

Figure 6.5: Detailed Built-Up Wing Structural Model

pieces were used directly to laser cut the wood so that the built wing would match the designed model.

6.2 System Identification Preliminaries

6.2.1 Least Squares

There are two sources of noise in the measurements from the experimental data. The first is the process noise, which is due to external disturbances to the system. For the flight tests these process noise includes gusts and turbulence. The second source of noise is measurement noise. Measurement noise is caused by an error in the measurements made by the sensors. Reliable models of either type of noise are not available for the present flight tests. Therefore, they are assumed to be zero, which results in an error,$\{\mathbf{e}\}$, in the output. Thus, for the present

equation-error system identification, the dynamics are written in the frequency domain[95].

$$\{\mathbf{z}\} = \{\mathbf{f}(\mathbf{\Theta})\} + \{\mathbf{e}\} \tag{6.10}$$

$$\{\mathbf{z}\} = [\mathbf{X}]\{\mathbf{\Theta}\} + \{\mathbf{e}\} \tag{6.11}$$

The vector $\{\mathbf{z}\}$ is the system outputs, such as the angle of attack, pitch angle and wing strain. These outputs are a function of the system parameters, $\{\mathbf{\Theta}\}$, shown in Eqn. 6.10. For a linear system the function is written as a matrix of regressors, $[\mathbf{X}]$, in Eqn. 6.11. The goal is to determine the matrix $\{\mathbf{\Theta}\}$ which will minimize the cost function defined by the norm of the error, $\{\mathbf{e}\}$.

$$J(\mathbf{\Theta}) = \frac{1}{2}\{\mathbf{z} - \mathbf{f}(\mathbf{\Theta})\}^T \{\mathbf{z} - \mathbf{f}(\mathbf{\Theta})\} \tag{6.12}$$

For the linear version of ordinary least squares, the analytical estimate of the parameter vector, $\left\{\tilde{\mathbf{\Theta}}\right\}$, which minimizes the least-squares cost function, $J(\mathbf{\Theta})$, is given by,

$$\left\{\tilde{\mathbf{\Theta}}\right\} = \left[\mathbf{X}^\dagger\mathbf{X}\right]^{-1}\{\mathbf{X}^\dagger\mathbf{z}\} \tag{6.13}$$

For the non-linear least squares, as is necessary for the output error method used in the flight testing, the solution for the parameter vector requires a numerical solution. The implementation of the Gauss-Newton method available in MATLAB was used to determine the solution.

6.2.2 Error Estimation and Analysis of Variance

To determine the uncertainty in the parameter estimates and to test for the statistical significance of the identified parameters, the analysis of variance (ANOVA) is used[96]. For all of the test statistics, a confidence interval of 95% will be used. The total variation, σ^2, in

the data is defined:

$$\sigma^2 = \{\tilde{\mathbf{z}} - \bar{z}\}^\dagger \{\tilde{\mathbf{z}} - \bar{z}\} \tag{6.14}$$

where $\bar{z}$ is the mean of the measured data. As expressed in Eqn. 6.10, a portion of this variation is due to the coefficients ($\left[\tilde{\mathbf{X}}\right] \left\{\tilde{\mathbf{\Theta}}\right\}$), the explained variation, and a portion is due to the error ($\{\tilde{\mathbf{e}}\}$), the unexplained variation. The unexplained variation is represented by the minimum value of the cost function $J\left(\tilde{\mathbf{\Theta}}\right)$, and is called the sum of squares of the error or squares of the residuals.

$$\text{SSE} = \{\tilde{\mathbf{z}} - \mathbf{f}(\mathbf{\Theta})\}^\dagger \{\tilde{\mathbf{z}} - \mathbf{f}(\mathbf{\Theta})\} \tag{6.15}$$

For the current regression, the number of statistical degrees of freedom is defined:

$$\text{df} = \dim\{\tilde{\mathbf{z}}\} - \dim\{\mathbf{\Theta}\} \tag{6.16}$$

where $\dim\{\tilde{\mathbf{z}}\}$ signifies the total number of data points and $\dim\{\mathbf{\Theta}\}$ represents the total number of coefficients. A greater number of statistical degrees of freedom is desired and will result in greater confidence in the parameter estimates. The overall ability for the model to predict the output are given by the the standard error of the model, s, and the multiple correlation coefficient, R^2.

$$s^2 = \frac{\text{SSE}}{\text{df}} \tag{6.17}$$

$$R^2 = \frac{\text{SSE}}{\sigma^2} \tag{6.18}$$

Similar to the signal to noise ratio, a value of R^2 close to one means that the noise is small, and so the model is able to correctly capture the output. The standard error, $\{\mathbf{s}\}$, of the

coefficients in $\left\{\tilde{\mathbf{\Theta}}\right\}$ is defined to be

$$\left\{\mathbf{s}^2\right\} = s^2 \left\{\boldsymbol{\lambda}_\Sigma\right\} \tag{6.19}$$

Where $\{\boldsymbol{\lambda}_\Sigma\}$ is the vector of eigenvalues of the covariance matrix $[\boldsymbol{\Sigma}]$ which is approximated by the Jacobian.

$$[\boldsymbol{\Sigma}] \approx \left[\frac{\partial \mathbf{f}\left(\mathbf{\Theta}\right)}{\partial \mathbf{\Theta}}^T \frac{\partial \mathbf{f}\left(\mathbf{\Theta}\right)}{\partial \mathbf{\Theta}}\right]^{-1} \tag{6.20}$$

Increases in the process or measurement noise will result in a larger standard error, and thus a larger uncertainty in the measurement. Hypothesis testing is used to test the validity of the regression result. For hypothesis testing a null hypothesis, H_0, and a contradictory alternative hypothesis, H_1, are established. The data is tested to see if it satisfies the null hypothesis. If the test fails then the null hypothesis is rejected and the alternative hypothesis is accepted. The first test is for the statistical significance of the parameters.

$$H_0 : \Theta_i = 0 \tag{6.21}$$

$$H_1 : \Theta_i \neq 0 \tag{6.22}$$

The t-statistic for the i-th parameter is defined:

$$t_i = \frac{\Theta_i}{s_i} \tag{6.23}$$

Assuming sufficient statistical degrees of freedom, df $\gtrsim 26$, then the estimate of the parameters will have a normal distribution, rather than a t-distribution. Therefore, if $t_i \geq 1.96$, zero does not lie within the likely values of the parameters. Thus we reject the null hypothesis, and accept that the estimated parameter is statistically significant. This means that even if the uncertainty is large, then the data does support that the parameter has a significant effect on the output. If the parameters representing the coupling between the structural

dynamics and the flight dynamics are statistically significant, then it can be concluded that the experiment is showing the desired coupling.

Some additional evaluation of the residuals is also desirable to test the quality of the model and the regression. In the regression and the evaluation of the significance of the coefficients, the residuals are assumed to be normally distributed, uncorrelated, and have uniform variance. This means that there exists a first order relationship between the error terms at one frequency and the next.

$$H_0 \quad : \quad \text{The errors are not correlated} \tag{6.24}$$

$$H_1 \quad : \quad \text{The errors are correlated} \tag{6.25}$$

6.3 Ground Testing

Before the flight testing could begin, a series of ground tests were performed to characterize the sensor behavior, test the airworthiness, and examine the structural dynamics. These test improved the confidence in the design and provide valuable information for the analysis with very low risk to the vehicle.

6.3.1 Sensor Calibration

The first goal of the ground testing was to characterize the behavior of the sensors on the aircraft. A calibration curve was required to relate the voltage that was recorded by the data logger to the quantity that was being measured. All of the sensors, except the elevator potentiometer, are designed to exhibit a linear behavior. The calibration curves for the accelerometer, gyro, and strain gages are all available from the specification sheets for the sensors. Although the specifications were available for the pitot tube's pressure sensor, calibration was performed to characterize the complete system and ensure that there were no

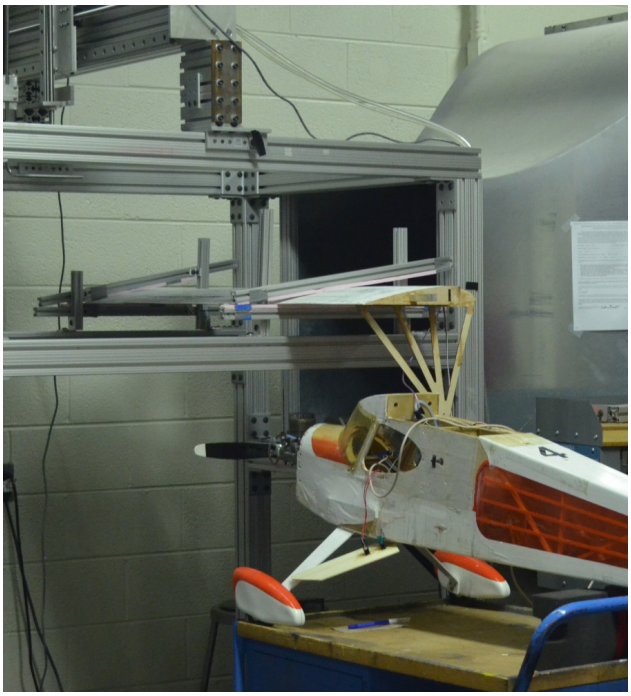

Figure 6.6: Calibration of Flexible Wing Pitot Tube

significant errors introduced by the alignment of the tube. As for the elevator potentiometer, the calibration was necessary because there are no published specifications available.

6.3.1.1 Elevator Potentiometer

The voltage of the potentiometer is provided by connecting the data logger to a computer. The elevator angle was measured using an inclinometer on the control surface. The corresponding elevator deflection and potentiometer voltage were measured for several different control inputs.

6.3.1.2 Pitot Tube

To calibrate the pitot tube, each wing was mounted in Virginia Tech's 0.7m open-jet wind tunnel, Figure 6.6. A monometer is available on the tunnel to provide the dynamic pressure at the open section. By recording the voltage at several different dynamic pressures, a

calibration curve can be calculated.

Additionally, the mounting brackets for the wing can be adjusted to repeat the calibration at various different angles of attack and angles of sideslip. This will ensure that there is no inaccuracy in the velocity measurements at the attitudes for the present flight testing.

6.3.2 Static Load Test

The simplest test to ensure the airworthiness of a new R/C aircraft is a static load test, i.e. a tip test. For the static load test, the aircraft is suspended only by the wing tips. This simulates a large load factor (≈ 2.7), since the loads in flight are distributed along the wing.

The static load test also provides an estimation of the wing bending stiffness, which is used in creating the wing structural dynamic model. Due to the symmetry of the loading, the wing is treated as a beam cantilevered at the wing root with a point load at the wing tip, the weight of the fuselage, and a uniform load along the span, the weight of the wing. Therefore the beam deflections from Euler-Bernoulli beam theory are given by[93]:

$$\begin{aligned} EI\delta z_{wing} &= \frac{W_{wing}}{384b} y^2 \left(\frac{6b^2}{4} - 2by + y^2 \right) \\ &\quad + \frac{W_{fuselage}}{6} y^2 \left(\frac{3b}{2} - y \right) \end{aligned} \tag{6.26}$$

Thus the wing stiffness is given by the slope of the line fit to the calculated deflections on the right and the measured deflections on the left.

6.3.3 Ground Vibration Test

Characterization of the structural dynamics are provided by ground vibration tests (GVT). To simulate a free boundary condition, as seen in flight, the aircraft was suspended with bungee cords, Figure 6.7. To provide excitation, an electromagnetic shaker was attached to the landing gear. This was selected as since it is a much more rigid connection then the

Figure 6.7: Suspension of Rascal for GVT

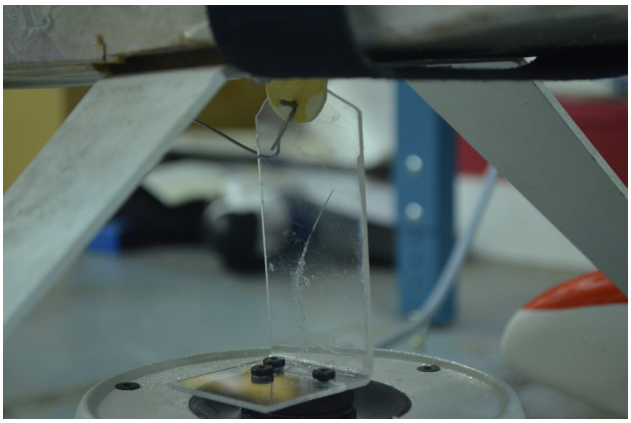

Figure 6.8: GVT Shaker Bracket

balsa wood covering the rest of the fuselage. This location for the excitation will not provide any excitation of the anti-symmetric modes, but these modes are of little interest for the current flight tests. The shaker was mounted to a flexible bracket, Figure 6.8, to provide as little constraint to the dynamics as possible in an attempt to maintain the free boundary conditions.

The shaker was used to provide linear and logarithmic frequency sweeps to the aircraft. These sweeps provided excitation from 1Hz to 10Hz. The shaker frequency was also manually adjusted to higher frequencies to identify modes above the anti-aliasing filters on the data acquisition system. The measurement of the accelerations from the IMU were used as in input

and the strain gages as the output for the system identification. This provides a precise and accurate measurement of the frequency of the first wing bending mode.

6.4 System Identification

6.4.1 Input Selection

The selection of the input can have a significant effect on the quality of the results. The present identification technique is permissive of a wide variety of inputs. However, it is desirable for these inputs to excite as broad a spectrum of the dynamics as possible.

The flight testing utilized frequency sweeps to the elevator. These frequency sweeps are input manually. Such manual inputs do not provide as precise inputs as automatically generated inputs. However, such variations can be more effective at providing excitation over the full bandwidth of interest[74]. Other inputs were explored, such as doublets and 3-2-1 doublets. However, these gave less accurate results due to the relatively short period of excitation. After the controls are returned to trim, the vehicle response becomes difficult to distinguish from the gust inputs.

6.4.2 Reconstruction of States

The IMU is unable to provide a direct measurement of the states that are used in the current parametrization. Therefore it is necessary to reconstruct these states from the measurements of the IMU and the strain gauges. Since the system identification is to determine the linear model, the linear equations of motion have been used. This restriction to the linear dynamics also decouples the longitudinal and lateral motions. Therefore, the yaw rate is not required for the reconstruction of the angle of attack or pitch angle.

$$\dot{w} \approx \frac{1}{2\mathrm{Fr}}\delta a_z + \delta\hat{q}\cos\alpha_0 \tag{6.27}$$

These equations represent the kinematic equations that will be used to reconstruct the angle of attack. The δ has been used to signify a perturbation from trim. At trim the pitch angle, θ, and angle of attack are equal. Therefor the α_0 terms can be replaced by the trim measurements from the accelerometer.

$$\dot{w} \approx \frac{1}{2\mathrm{Fr}}\delta a_z + a_{z_0}\delta\hat{q} \tag{6.28}$$

The Euler angles are reconstructed from the linearized rotational kinematic equations.

$$\dot{\theta} \approx \delta\hat{q} \tag{6.29}$$

with the initial conditions

$$\hat{w}(0) \approx a_{z_0} \tag{6.30}$$

$$\theta(0) \approx a_{x_0} \tag{6.31}$$

The expression for $\dot{\theta}$ is integrated first.

6.4.3 Signal Conditioning and Filtering

The drawback to reconstructing the states from the measurements of the IMU is that the accelerometer and gyros typically have some bias in the measurement. The errors from the bias are amplified by the integration used for the reconstruction. The bias causes the reconstructed states to drift, leading to significant errors in the reconstructed state. To reduce the errors signal conditioning and filtering is required.

The first step in the signal conditioning is to detrend the data. The detrending removes any linear trend that is present in the data. To achieve this a line is fit to the data. The detrended data is the difference between the original data and the line.

Detrending will resolve the primary bias and drift errors. Additional bandpass filtering of-

Table 6.1: Bandpass Filter Properties

First Stopband	0.1Hz
First Passband	0.2Hz
Second Passband	10Hz
Second Stopband	12Hz
Stopband Attenuation	80dB
Passband Ripple	0.5dB

fers the ability to focus the system identification on the short-period mode and the structural dynamics. The parameters in Table 6.1 were used to design a minimal order Butterworth bandpass filter. The Butterworth filter uses an a polynomial approximation of the ideal filter to design an infinite impulse response (IIR) filter. The first passband was selected to be well below the anticipated frequency of the short-period mode. The upper passband was selected to correspond the the analog anti-aliasing filters on the data acquisition system.

6.4.4 Output Error System Identification

Initially an equation error technique was considered for the system identification. The equation error provides the solution as a linear least squares problem. However, it requires a more specific form for the equations of motion and also requires differentiation of the signals. Without the typical filters on the inertial measurement unit and the significant bandwidth required for identification of the structural dynamics, the differentiated signals were excessively noisy. This made identification of a reasonable model impossible. Instead an output error technique was selected. This technique only requires the outputs, which were selected to have significantly lower noise.

The present remotely piloted vehicle (RPV) requires line-of-sight for flight. This limits the lengths of maneuvers and makes identification of the Phugoid mode difficult. Furthermore, the primary interest is only in the interaction of the short-period mode with the structure.

Since the Phugoid mode is neglected, the identified system is fourth order with two

second order modes. These modes are the short-period mode, with reduced frequency k_{sp} and damping ζ_{sp}, and the aeroelastic mode, with reduced frequency k_ε and damping ζ_ε. These parameters were constrained such that

$$0.01 \leq \quad k_{sp} \quad \leq 0.1 \tag{6.32}$$

$$0.1 \leq \quad k_{\varepsilon} \quad \leq 0.7 \tag{6.33}$$

$$0 \leq \quad \zeta_{sp} \quad \leq 1 \tag{6.34}$$

$$0 \leq \quad \zeta_{\varepsilon} \quad \leq 1 \tag{6.35}$$

The lower bound on the damping insures stability of the identified model. The stability of the actual aircraft is clear from the handling qualities of the aircraft during the flight tests. The upper bound on the damping ensures that the system remains second order, which is expected from simulations of the vehicle. The bounds on the frequency ensure that the frequency remains in the bandwidth that has not been attenuated by the band-pass filtering, and prevents both poles of the model from converging on the same mode.

The outputs were selected for the parameters which will show significant response in the short-period mode. The outputs of the system, $\{\mathbf{z}\}$, are selected to be the plunge velocity (equal to the angle of attack for small angles), $\hat{w}$, pitch angle, θ, and the wing strain, ε. For these outputs the relative of the degree is known. The angle of attack has a relative degree of 1 while the pitch angle and wing strain have relative degree 2.

With the knowledge of the system, the transfer functions of the flexible vehicle have the parametrization:

$$\left\{\frac{\mathbf{F}(s,\Theta)}{U(s)}\right\} = \frac{\begin{bmatrix} n_{13} & n_{12} & n_{11} & n_{10} \\ 0 & n_{22} & n_{21} & n_{20} \\ 0 & n_{32} & n_{31} & n_{30} \end{bmatrix} \begin{Bmatrix} s^3 \\ s^2 \\ s \\ 1 \end{Bmatrix}}{\left(s^2+\zeta_{sp}k_{sp}s+k_{sp}\right)\left(s^2+\zeta_{\epsilon}k_{\epsilon}s+k_{\epsilon}\right)} \tag{6.36}$$

Thus there are 14 terms in the coefficient vector, $\{\mathbf{\Theta}\}$.

As discussed in section 6.2.1, the outputs of the system, $\{\mathbf{z}(t)\}$, are equal to the outputs of the transfer function in Eqn 6.36, $\{\mathbf{f}(t,\mathbf{\Theta})\}$, plus some noise, $\{\mathbf{e}(t)\}$[95].

$$\{\mathbf{z}(t)\} = \{\mathbf{f}(t,\mathbf{\Theta})\} + \{\mathbf{e}(t)\} \tag{6.37}$$

For the output error technique it is assumed that the error is due only to measurement noise. Output error does not consider process noise, i.e. disturbances such as gusts[95]. Such disturbances can cause the outputs to be correlated since there are additional unmeasured inputs.

The value of the function, $\{\mathbf{f}(t,\mathbf{\Theta})\}$, does require the integration of the transfer function in Eqn 6.36. This integration is achieved by the *lsim* function, an explicit numerical integration scheme, in MATLAB.

The goal is to determine the vector of 14 coefficients, $\left\{\tilde{\mathbf{\Theta}}\right\}$, which minimizes the norm of the error, $J\left(\tilde{\mathbf{\Theta}}\right)$[95].

$$\tilde{\mathbf{\Theta}} = \min_{\mathbf{\Theta}\in\mathbb{R}^{14}} J(\mathbf{\Theta}) \tag{6.38}$$

$$\text{such that } J(\mathbf{\Theta}) = \frac{1}{2}\{\mathbf{z}-\mathbf{f}(\mathbf{\Theta})\}^T\{\mathbf{z}-\mathbf{f}(\mathbf{\Theta})\} \tag{6.39}$$

The solution of the least squares problem is provided by the numerical function *lsqnonlin*

available in MATLAB.

Chapter 7

Results

7.1 Modeling

The modeling approach has been applied to the airborne subscale transport aircraft research testbed (AirSTAR) generic transport model (GTM). A rigid body simulation of the aircraft was available, and has been expanded to include the structural degrees of freedom.

7.1.1 Verification and Validation

The focus of the modeling results is to the verification and validation of the model. Lacking a baseline model, the individual pieces, aeroelastic/structural dynamics and flight dynamics, are independently checked. Since the flight dynamics are taken directly from the earlier GTM simulation the verification has been omitted. Finally the interactions of these separate pieces are examined by scaling the structural stiffness.

7.1.1.1 Aeroelastic Model Verification

The Goland wing[97] is used for verification of the aeroelastic portion of the current model. The comparison of the current numerical results and the exact analytical results of Goland

and Luke[98] are shown in Table 7.1. The current results match the exact analytical solution very well. The slight difference is likely due to the approximation used for Theodorsen's function.

Table 7.1: Verification of Aeroelastic Model

	Current Model	Goland and Luke[98]
Flutter Speed, *mph*	305	307
Flutter Frequency, *rad/s*	72.7	70.7

7.1.1.2 Aeroelastic Model Validation

The flight test data from the June 2010 deployment of the GTM was used for validation of the current model. Unfortunately, due to a lack of direct measurement of the structural response and the limited control bandwidth available, a complete validation of the current model was not possible. However, examination of the power spectral density of the IMU output in Figure 7.1 shows several peaks in the power at the structural frequencies due to gust excitation. Each plot represents the data from a different card (i.e. maneuver) during the testing.

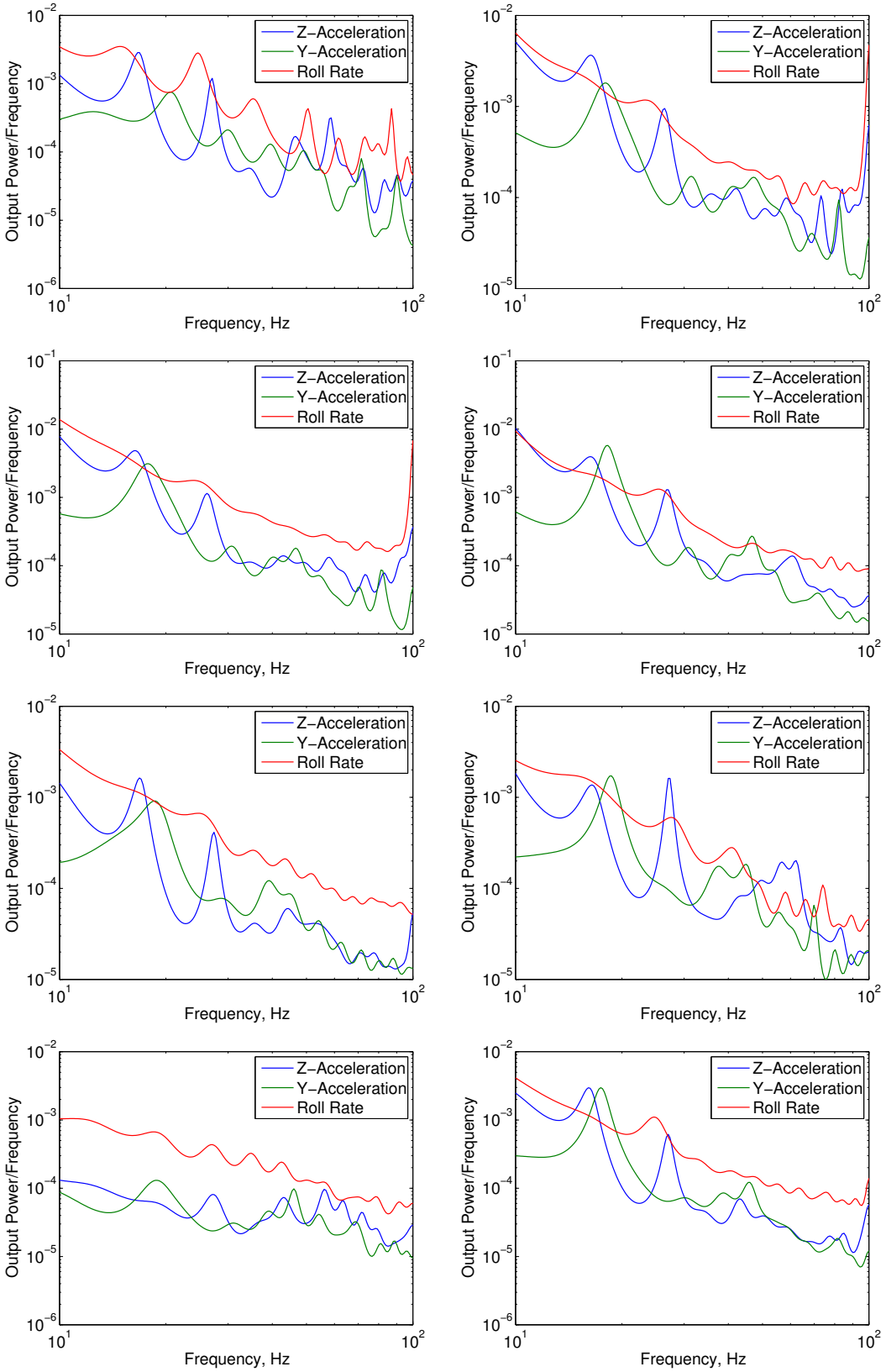

Figure 7.1: Power Spectrum Density from Flight Test Data

Examination of the peaks in the frequency response allows for identification of the GTM's aeroelastic resonant frequencies. Since not every maneuver clearly shows the excitation of all the modes, the mode shape results of the ground vibration tests were used to determine the outputs in which these peaks should occur to ensure that no modes are being overlooked. The first four modes and the corresponding output are shown in Table 7.2.

Table 7.2: GVT Mode Shape Descriptions

Mode	Description		Measurement
1	Symmetric	Wing Bending	Z-acceleration
2	Asymmetric	Wing/Fuselage Bending	Y-acceleration
3	Asymmetric	Tail Twist	Roll Rate
4	Symmetric	Fuselage Bending	Z-acceleration

The frequencies identified from several different maneuvers are shown in Figure 7.2. To determine a confidence interval for the flight test data a linear fit was used. Due to the large uncertainty in the data a higher order fit was not possible. The simulation frequencies are remaining within the confidence interval for the entire range currently tested.

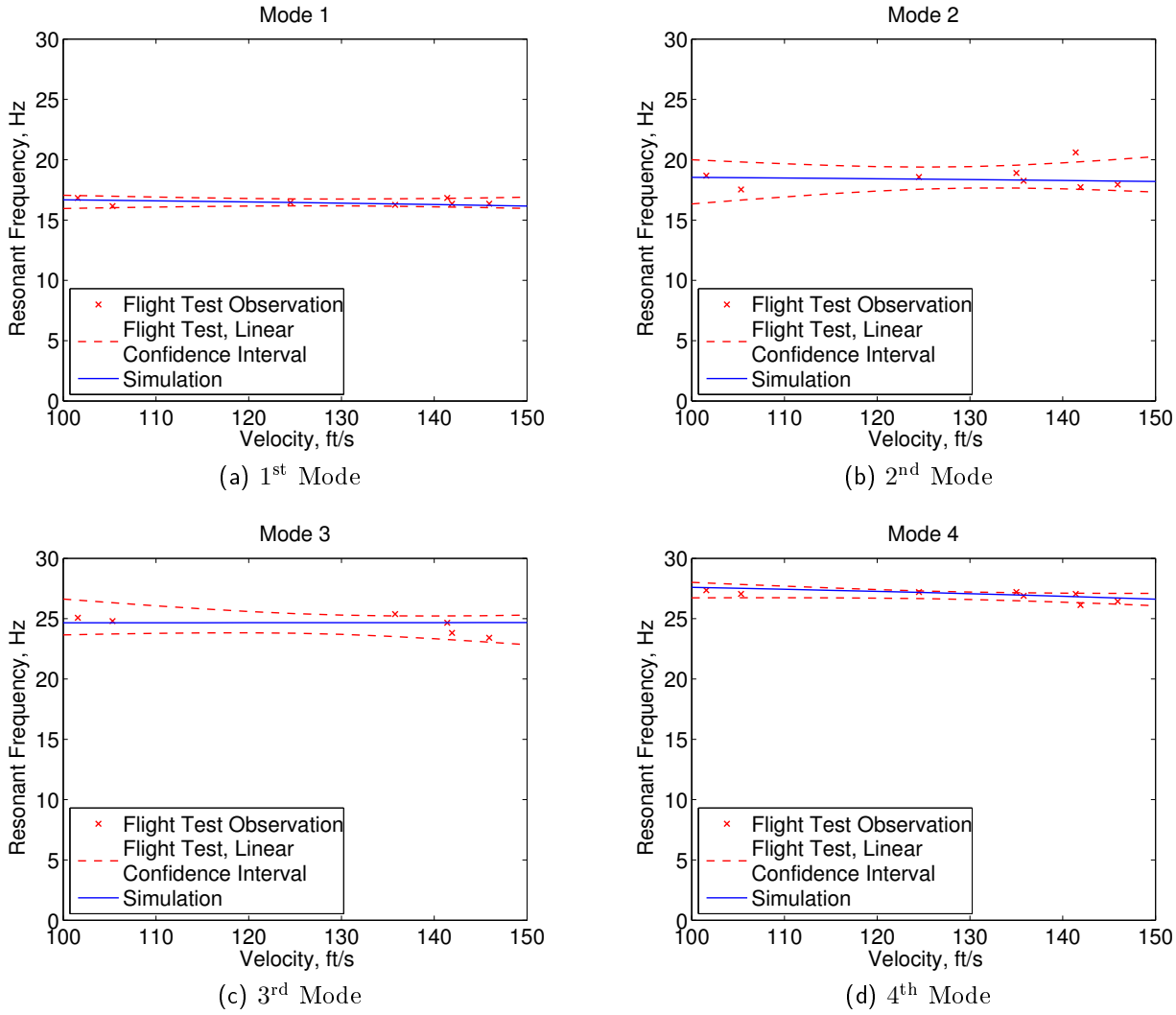

(a) 1st Mode (b) 2nd Mode

(c) 3rd Mode (d) 4th Mode

Figure 7.2: Variation in Frequencies of Structural Modes over Flight Envelope

7.1.1.3 Coupling Verification

Verification of the coupling is given by scaling the modal stiffness matrix. As the stiffness increases, the separation between the frequency of the rigid body modes and the flexible modes increases. As a result, the effects of the flexibility will decrease, and the eigenvalues will converge to the poles of the rigid simulation. The convergence of these poles to the rigid aircraft results is shown in Figure 7.3.

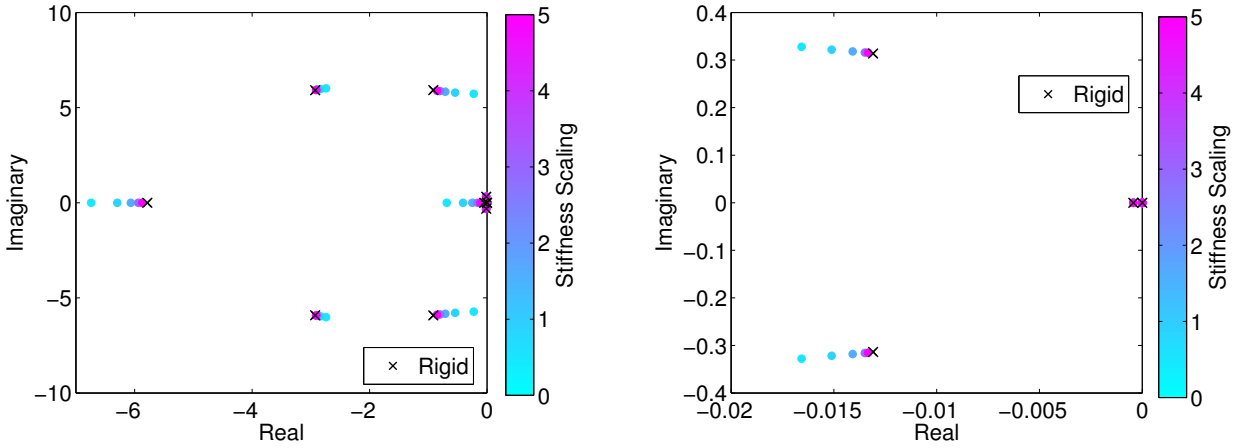

(a) Short Period, Roll, Spiral, and Dutch Roll Modes

(b) Phugoid Mode

Figure 7.3: Root Locus of Flexible Aircraft

7.2 Adaptive Control

Currently the adaptive controller has been implemented on the simulation of the AirSTAR GTM. Due to the very different time scales of the structural dynamics, flight dynamics and control law dynamics, it becomes very difficult to interpret the outputs directly. As a result, the root mean squared (RMS) error[85] is used to evaluate the tracking ability of the present controller.

$$\bar{e}(t) = \sqrt{\frac{1}{t}\int_0^t \|y_m(\tau) - y(\tau)\|^2 \, d\tau} \tag{7.1}$$

This RMS error shows the overall trends while removing the high frequency variations due to the structure. It appears that both controllers are giving a bounded error in Figure 7.4 for both configurations, but as expected the more flexible aircraft has a larger tracking error for both the adaptive and non-adaptive controllers. For both vehicles the adaptive controller

gives a lower tracking error, which is expected since the adaptive controller is better capable of accounting for the parametric uncertainty that the structure introduces.

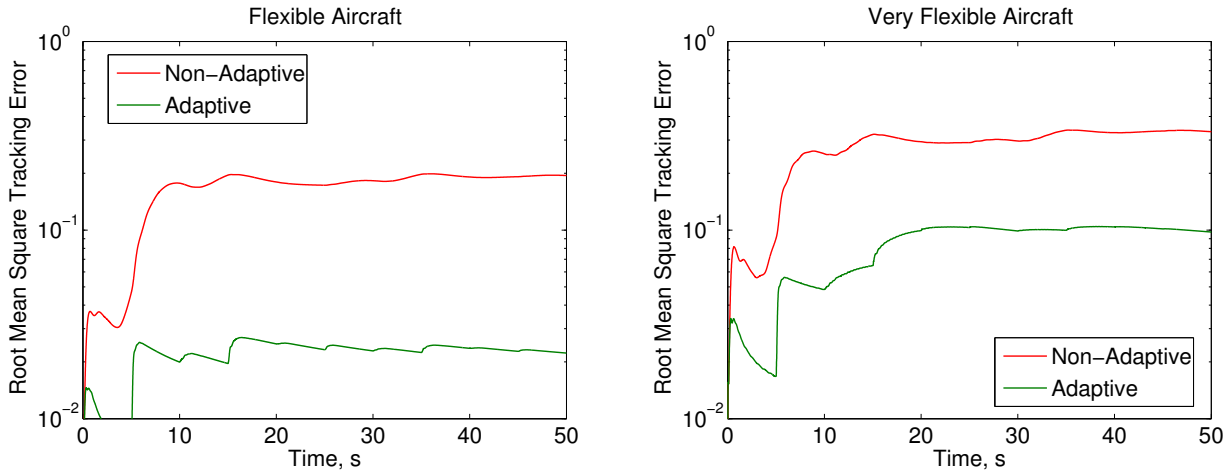

(a) Flexible Aircraft Tracking Error

(b) Very Flexible Aircraft Tracking Error

Figure 7.4: Closed Loop Tracking Error

In addition to the tracking error, the structural deformations in Figure 7.5 are also considered. The spikes in the structural deformations are occurring at the edges of the square wave. For these cases the deformations are remaining reasonably small. Although larger deformations are expected for the flexible vehicle, by halving the stiffness the deformations have increased by almost an order of magnitude. There also appears to be more variation in the peaks for the very flexible configuration, such as the very large spike at 20 s, which is not reflected in the nominal flexible vehicle. Furthermore, comparing the deformations due to the non-adaptive controller in Figures 7.5c and 7.5d the adaptive controller is clearly leading to larger deformations than the non-adaptive controller. These effects are amplified as the the adaptive gain is increased.

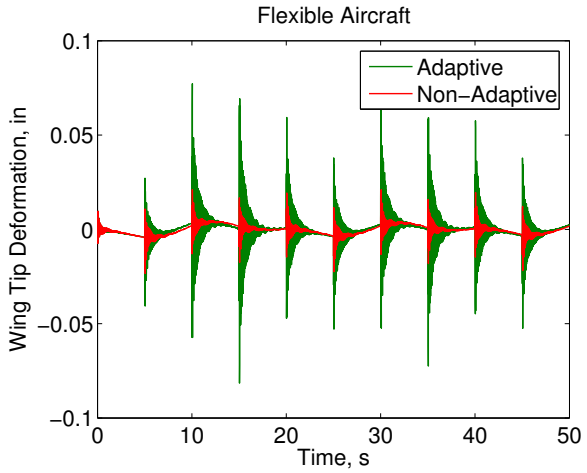

(a) Deformations for Adaptive Controller

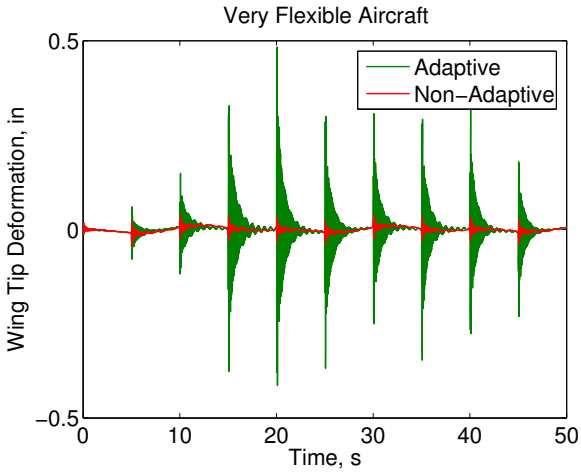

(b) Deformations for Adaptive Controller

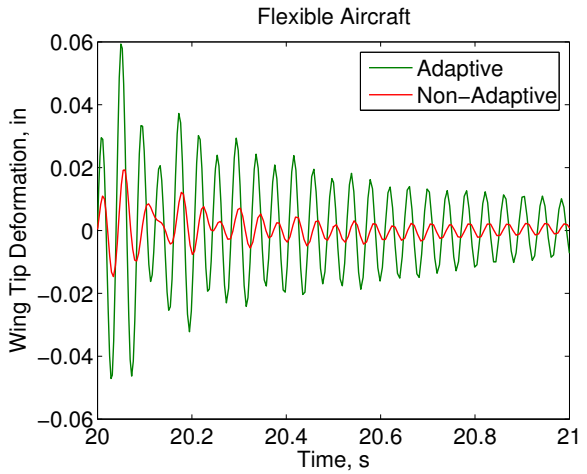

(c) Flexible Configuration

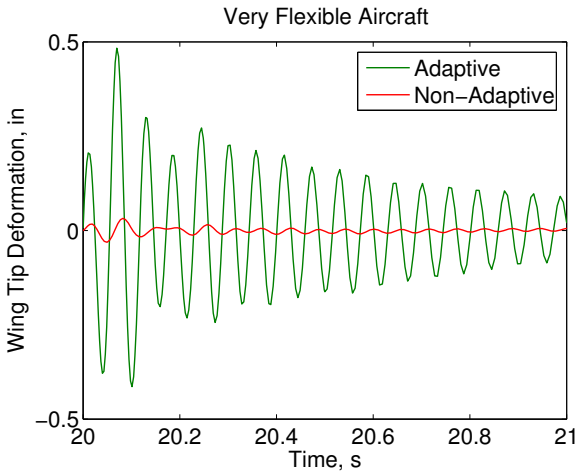

(d) Very Flexible Configuration

Figure 7.5: Comparison of Structural Deformations

The control inputs are shown in Figure 7.6. The inputs to the aileron and rudder for the rigid aircraft are zero, and are omitted for clarity. There is significant high frequency content for both of the flexible configurations, and it is clear that this high frequency content is increased as the flexibility is decreased. The increased inputs to the aileron and rudder are due in part to asymmetries from the mode shapes, but it is clear that these are exacerbated by the time varying control gains.

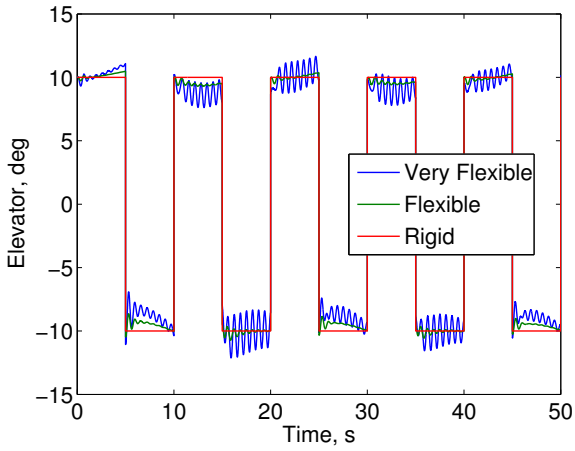

(a) Elevator Inputs

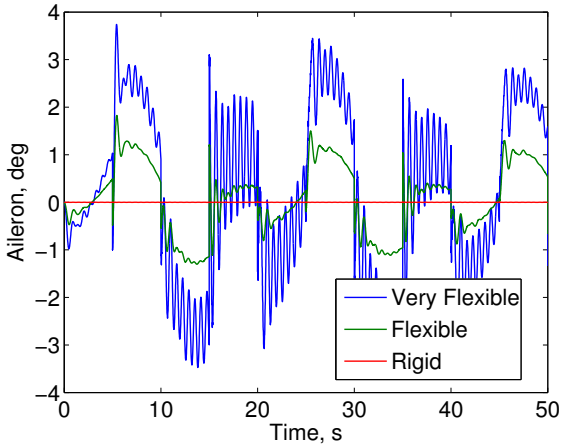

(b) Aileron Inputs

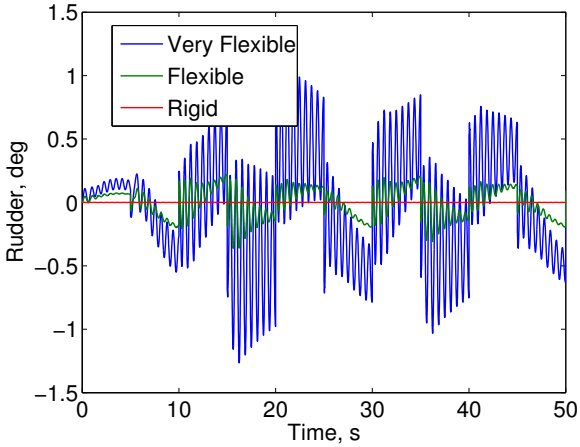

(c) Rudder Inputs

Figure 7.6: Control Inputs for Closed Loop Simulation

7.3 Scaling

7.3.1 Model Reduction

To illustrate the effect of the approximation on the system dynamics, the responses of transport aircraft of Waszak and Schmidt[15] to elevator inputs are demonstrated in Figure 7.7. The velocity and pitch angle perturbations are zero for the reduced order model, so they are not shown. The reduced frequencies of the three modes are shown in Table 7.3.

Table 7.3: Aerodynamic Coefficients of a Flexible Transport

Mode	Frequency
Phugoid	7.04×10^{-4}
Short-period	2.13×10^{-2}
Aeroelastic	1.44×10^{-1}

At low frequencies the Phugoid mode causes a significant mismatch. In the vicinity of the short-period and aeroelastic mode the reduced order model matches the full order model very well. As a result, any partial similitude based on the short-period approximation should be very effective at capturing the dynamics of these higher frequency modes.

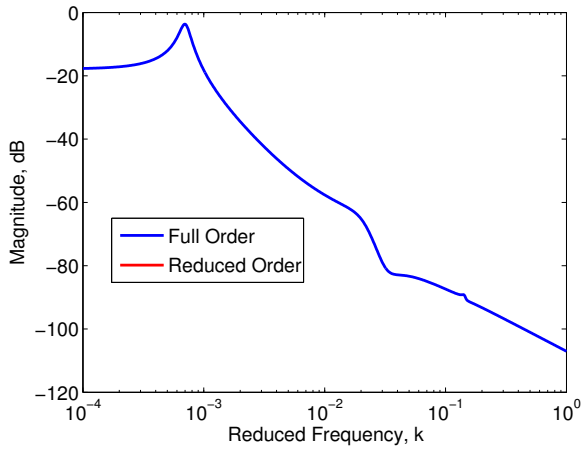

(a) Velocity, $\hat{V}$

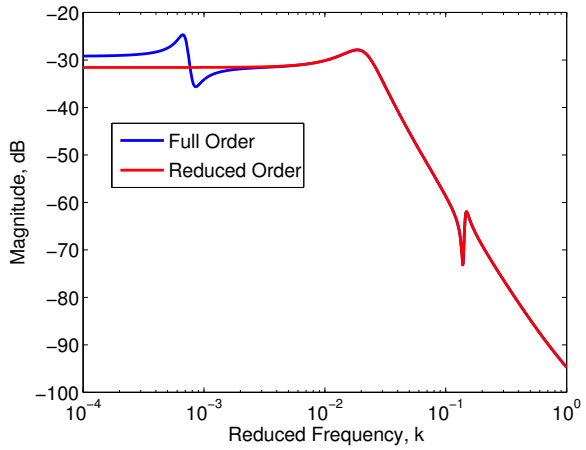

(b) Angle of Attack, α

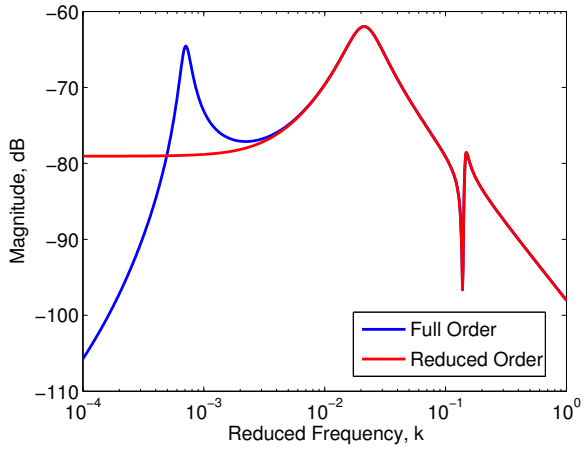

(c) Pitch Rate, $\hat{q}$

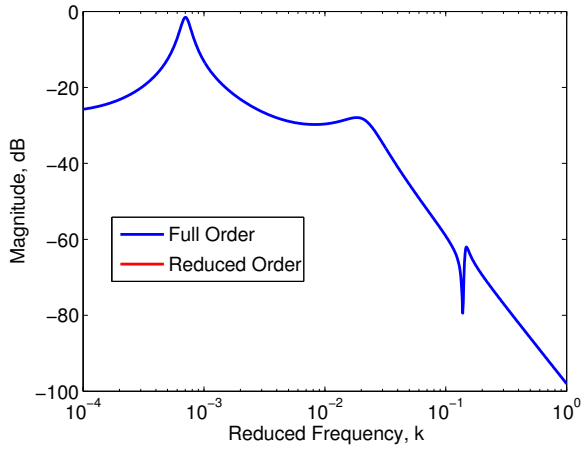

(d) Pitch Angle, θ

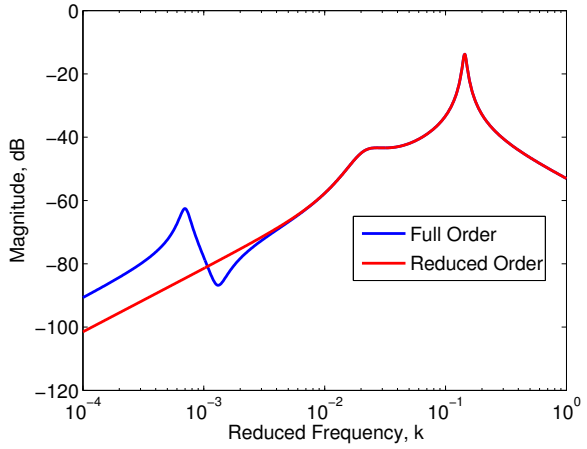

(e) Modal Rate, $\overset{*}{\xi}$

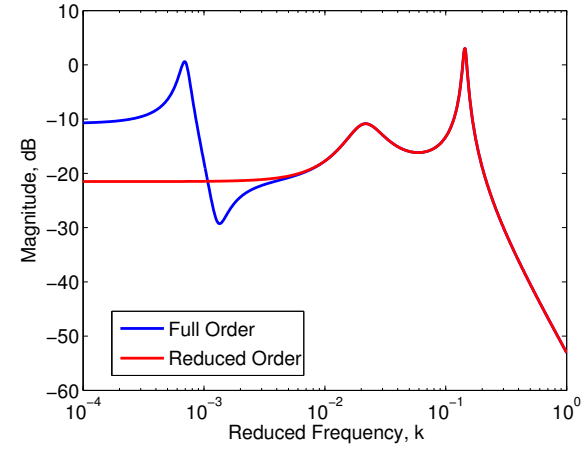

(f) Modal Displacement, ξ

Figure 7.7: Frequency Response to Elevator Input

7.3.2 Sensitivities

The sensitivities of the aircraft response shown in Figure 7.8, correspond to the response shown in Figure 7.7.

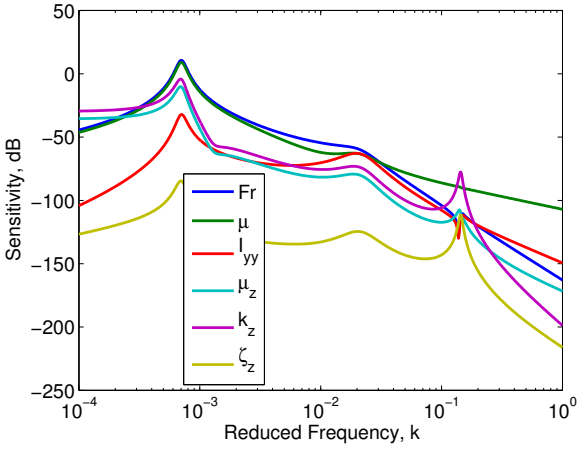

(a) Sensitivity of Velocity, $\hat{V}$

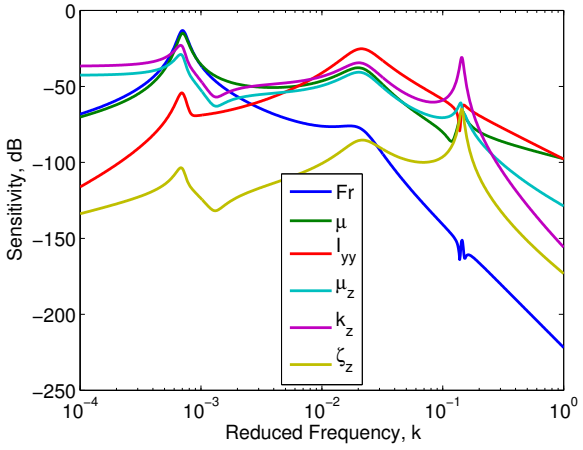

(b) Sensitivity of Angle of Attack, α

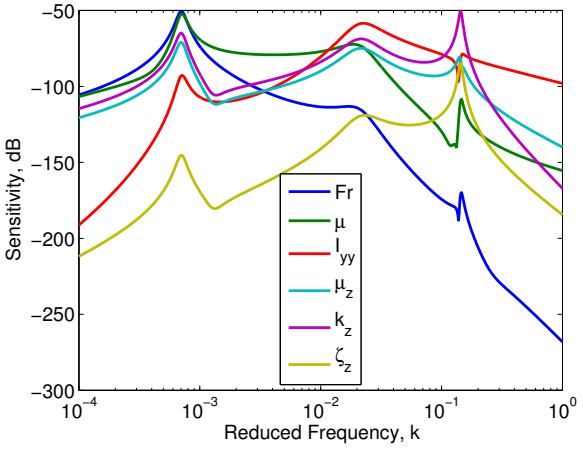

(c) Sensitivity of Pitch Rate, $\hat{q}$

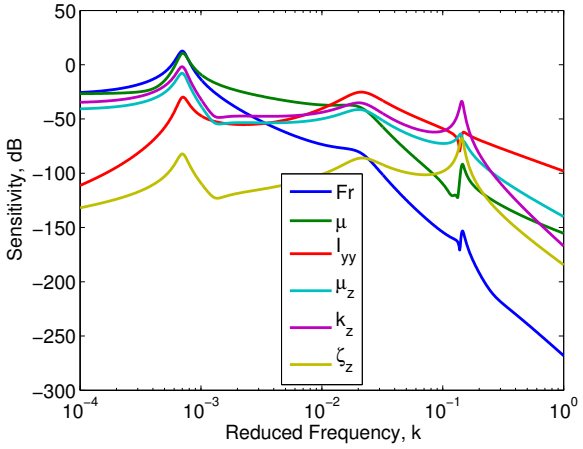

(d) Sensitivity of Pitch Angle, θ

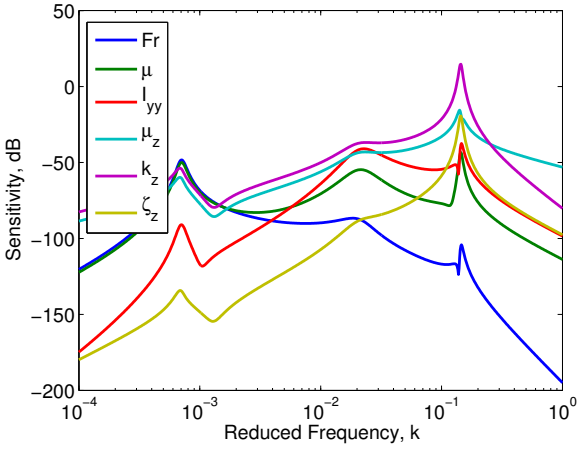

(e) Sensitivity of Modal Rate, $\overset{*}{\xi}$

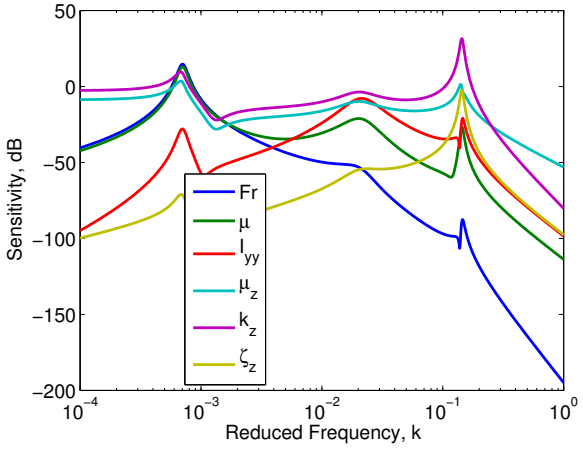

(f) Sensitivity of Modal Displacement, ξ

Figure 7.8: Sensitivity of Magnitude of the Frequency Response

As shown in Figure 7.7, for the present coupled system the velocity variations remain small at frequencies above the Phugoid mode. The velocity variations are often neglected in the consideration of the short-period or aeroelastic modes. These dynamics are of little interest, and the scaling will not attempt to achieve similitude in this minor effect. Thus, the sensitivity of the velocity response shown in Figure 7.8a is neglected in the determination of the scaling laws.

7.3.3 Scaling Parameters

Both the model reduction and sensitivity results are used to determine the requirements of a simplified subscale model. The model is designed to capture the coupling between the short-period mode and the first aeroelastic mode of a fullscale prototype.

Before applying the new methods of the model reduction and sensitivities, traditional intuition can provide some simplification of the model. The matching of the mass ratio at a lower altitude, with a higher air density, will result in a subscale model with a relatively high mass. By selectively applying the extra mass the inertial properties can be tailored. For example, adding weight near the wing tip can produce change the mass ratios, μ and μ_i. The effect on the roll and yaw inertia, $\hat{I}_{xx}$ and $\hat{I}_{zz}$ are not a concern. By considering only the longitudinal dynamics in both the model reduction and the sensitivities the roll and yaw inertia no longer appear in the equations of motion. If weight is placed near the x-coordinate of the center of gravity it will have a small effect on the pitch inertia, $\hat{I}_{yy}$. This means that it is possible to tailor the the mass ratios, μ and μ_i, independently of the pitch inertia.

Further simplifications are possible if to model is designed to focus on either the structural motion which appears in the short-period mode or the rigid body motion which appears in the aeroelastic mode.

7.3.3.1 Structural Motion in the Short-Period Mode

It is impossible for a rigid aircraft to capture this structural motion. This is the coupling which leads to body-freedom flutter. Furthermore, this motion is part of the short-period modes so the structural excitation by the controls cannot be removed by notch-filters. Therefore it is important to be able to create models which will capture this coupling. In the model reduction these effects are illustrated by examine the output of the rigid body motion, α and $\hat{q}$. In the sensitivities, these effects are shown by examine the structural degrees of freedom, ξ and$\overset{*}{\xi}$, in the vicinity of the frequency of the short-period mode, 2.13×10^{-2}rad.

The first consideration for the model are the effects of the trim state. For the sensitivity analysis, it is necessary to assume that these effects are negligible so that the system can be expressed in the frequency domain. The validity of this assumption is illustrated by the model reduction technique. The only parameter that appears in the reduced order model is the drag term, C_{D_0}. Since this parameter is added to the lift curve slope, C_{L_α} which is much larger, it's effects are negligible.

A less intuitive parameter, is the vehicle's Froude number, Fr. This parameter is important for capturing the effects of gravity. Looking at the model reduction, the Froude number appears nowhere in the equations. Similarly, with the sensitivities, the effect of the Froude number is very small at frequencies above the Phugoid mode, including at the short-period mode. Therefore it can be concluded that the Froude number has a negligible effect on structural motion component of the rigid body modes. Variations in the Froude number allow for a vehicle with a lower speed. The reduction in speed allows for a vehicle with a simpler and less expensive power plant. For a remotely piloted vehicle, the lower flight speeds also result in a vehicle which is much easier to fly. Finally, since these subscale models are often engaged in very high risk flight tests, these lower flight speeds will reduce the damage to the vehicle and property in the event of a crash. The variations in the Froude number are limited by the requirement that the aerodynamics remain linear. If the speed is reduced too far, then the lift curve slope, C_{L_α}, will change, which will effect the short-period mode. It

is reasonable that the Froude number will not have a significant effect since there is little change in altitude in the short-period mode, and thus little change in the potential energy of the system due to gravity.

Additionally, the reduced frequencies of the structural modes must be maintained. Because the dynamic pressure is reduced, the flexibility must be decreased to maintain the structural deformations. This can be seen by considering the non-dimensional stiffness parameters of a beam, $\widehat{EI} = \dfrac{4EI}{\rho V_0^2 S\bar{c}^2}$ and $\widehat{GJ} = \dfrac{4GJ}{\rho V_0^2 S\bar{c}^2}$. The stiffness is proportional to the square of the velocity, $EI \propto V_e^2$ and $GJ \propto V_e^2$. For example, a 10% reduction in velocity would require an 19% reduction in structural stiffness.

The other effect observed is the modal damping, ζ. It is not possible to draw any conclusions from the model reductions. However, examination of the sensitivities shows that the damping has a very small effect on the response at frequencies close to the short-period mode. Allowing mismatch in the damping allows for flexibility in the selection of materials for the structure. For example, plastics generally have a much higher damping then the aluminum often used in the full scale structure.

Of further note is the significance of the reduced structural frequency, k. The stiffness, which is traditionally assumed to be insignificant, has been shown to be more important then either the Froude number, Fr, or the modal damping, ζ.

7.3.3.2 Flight Dynamic Motion in Aeroelastic Modes

The other coupling of interest is the flight dynamic motion that appears in the structural modes. In the model reduction these effects are shown by looking at the output for the structural degrees of freedom, ξ and $\overset{*}{\xi}$. For the sensitives, the rigid body states, α and $\hat{q}$, are examined at frequencies close to the aeroelastic mode, 1.44×10^{-1}rad. This coupling is more difficult to achieve than the structural motion in the flight dynamics. For example, the effect of the structural damping cannot be ignored. As expected, for the aeroelastic mode, the reduced structural frequencies, k, is the dominant parameter effecting the dynamics. As

before, the trim state for the vehicle does not have a significant effect on the flight dynamic motion which appears in the aeroelastic mode. Also, the Froude number has little effect on the coupling. As a result, the model can be designed to fly at a lower trim speed while still capturing the rigid body motion that appears in the aeroelastic modes.

7.4 Flight Testing

The results for the flight testing include the design of the flexible wing with the structural properties, the ground testing to evaluate the design before flying, and finally the results of the flight tests.

7.4.1 Wing Design

The preliminary design results are shown to to give clarity as to where the selection of the wing design was determined. The final detailed model is also demonstrated.

7.4.1.1 Preliminary Wing Design

The deflections under the test loads used for the determination of the equivalent beam properties are shown in Figure 7.10.

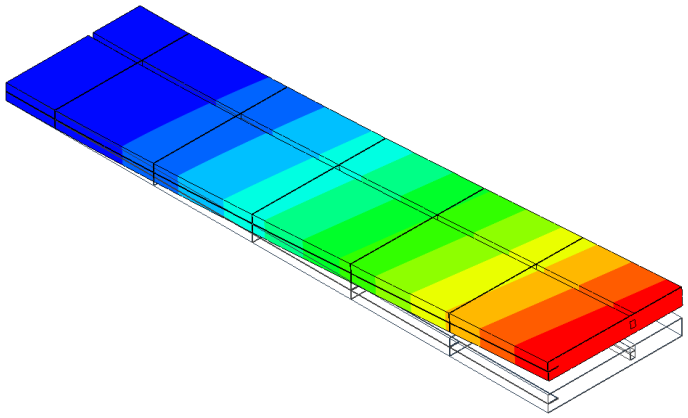

(a) Uniform Force Along Leading Edge

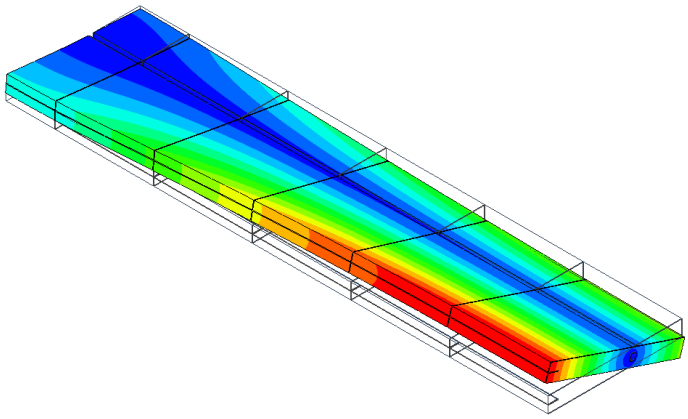

(b) Moment Along Mid Chord

Figure 7.9: Deflections Under Test Loads

The deflections due to the distributed force appear to be very well behaved. There appears to be very little chordwise deflection, assumed to be zero for Euler Bernoulli beam theory. The individual foam sections are not showing excessive flexibility. This is shown by the deflections which are monotonically increasing along the span. When the load is restricted to the moment the results are not as well behaved. The deflections near the root are non-zero, which violates the assumptions of St. Venant torsion.

The deflections of the rib at the wingtip are shown in Figure 7.10.

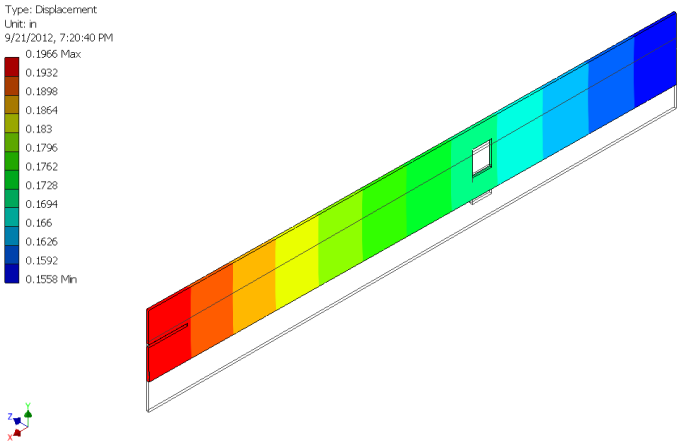

(a) Uniform Load at Leading Edge

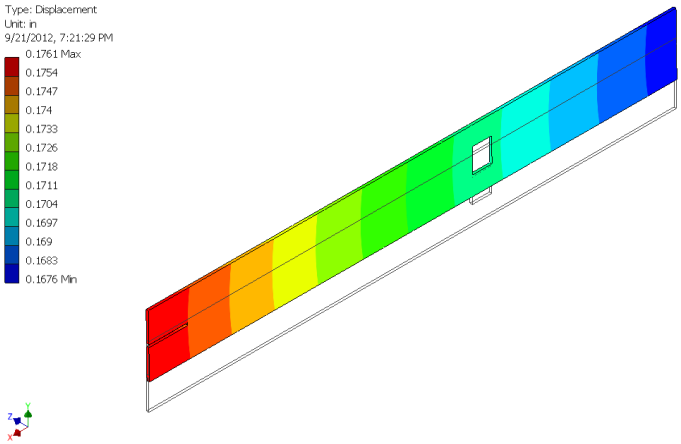

(b) Uniform Load at Mid Chord

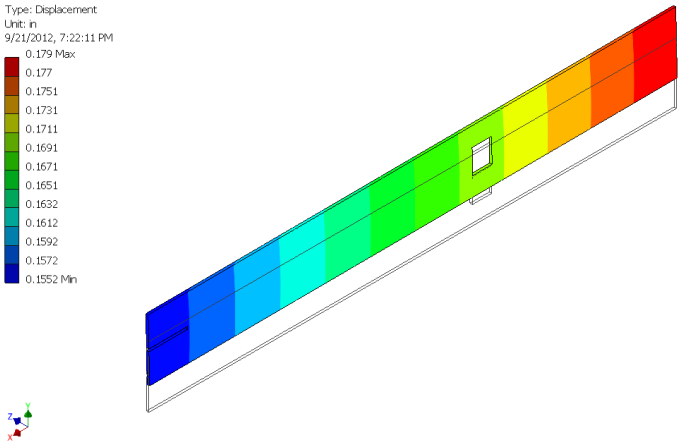

(c) Uniform Load at Trailing Edge

Figure 7.10: Tip Deflections Under Test Loads

The resulting beam properties for the finite element model are shown in Table 7.4. The Elastic axis is very close to the aluminum spar, but it has changed slightly due to the foam and ribs. The center of gravity is further forward due to the inclusion of extra weight at the leading edge.

Table 7.4: Equivalent Beam Properties

Elastic Axis, $x_{ea}/\bar{c}$	0.63
Bending Stiffness, EI	850
Torsional Stiffness, GJ	546
Center of Gravity, $x_{cg}/\bar{c}$	0.275
Mass, m/b	0.0361
Moment of Inertia, I_{yy}	0.0028

The wing under the correct loads for the 3g pull-up maneuver used for the design are shown in Figure 7.11. The factor of safety was shown in lieu of the stress due to the different materials used. The lowest factor of safety is 1.96, which is well in excess of the required 1.5. This is the lowest possible safety factor found while using standard available aluminum sections for the spar.

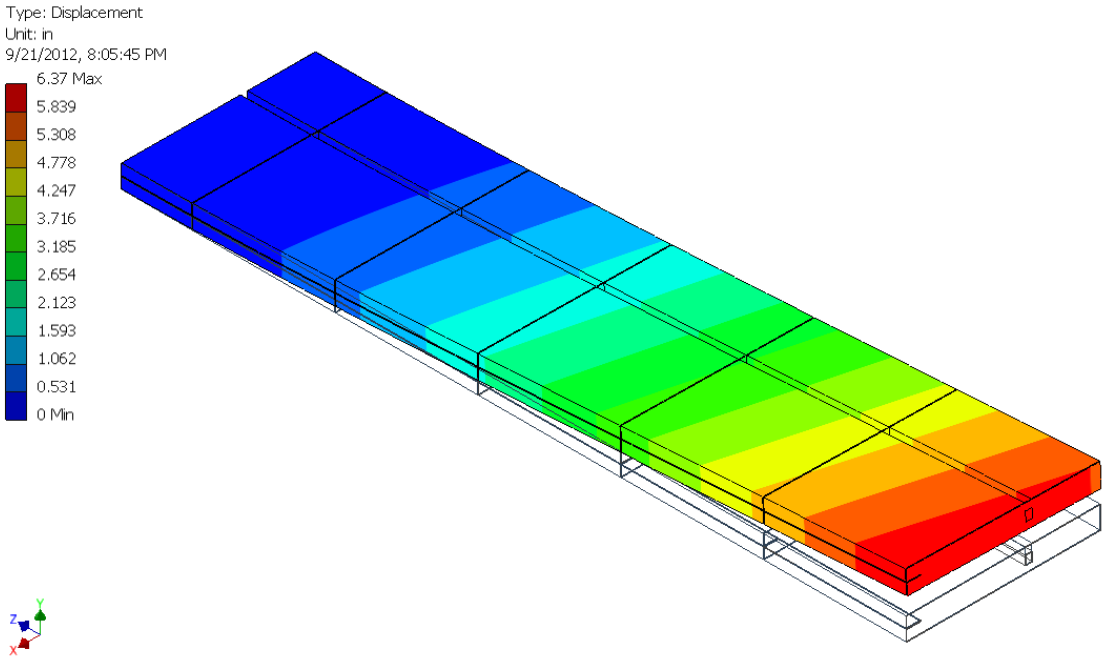

(a) Deflections

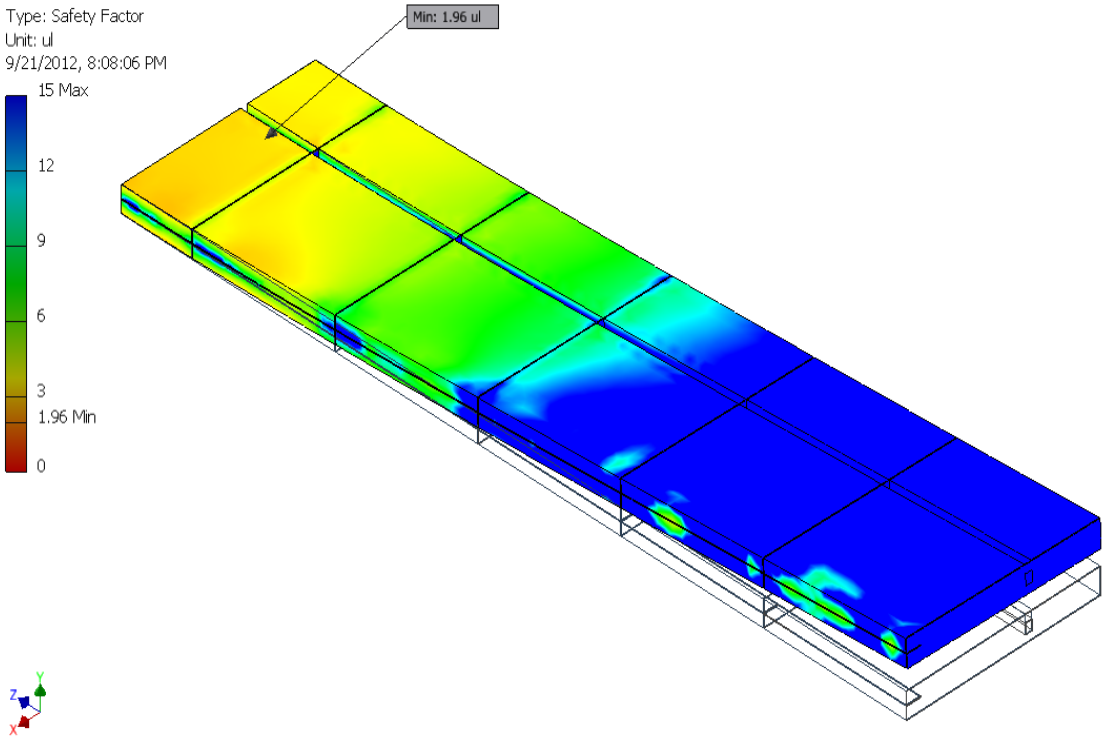

(b) Factor of Safety

Figure 7.11: Wing in 3g Pull-up Maneuver

As seen with the earlier test loads, the deflections appear satisfy the assumptions required for the equivalent beam properties. However, when the deflections of the Inventor model are compared to the analytical solutions from the equivalent beam properties, shown in Table 7.5, there is a significant mismatch in the twist. This is likely due to the issues seen at the root.

Table 7.5: Wing Tip Deflections

	Inventor	Analytical	Error
Deflection (in)	6.01	6.12	1.8%
Rotation (°)	2.41	3.64	33.7%

The mode shapes for the first 4 modes are shown in Figure 7.12.

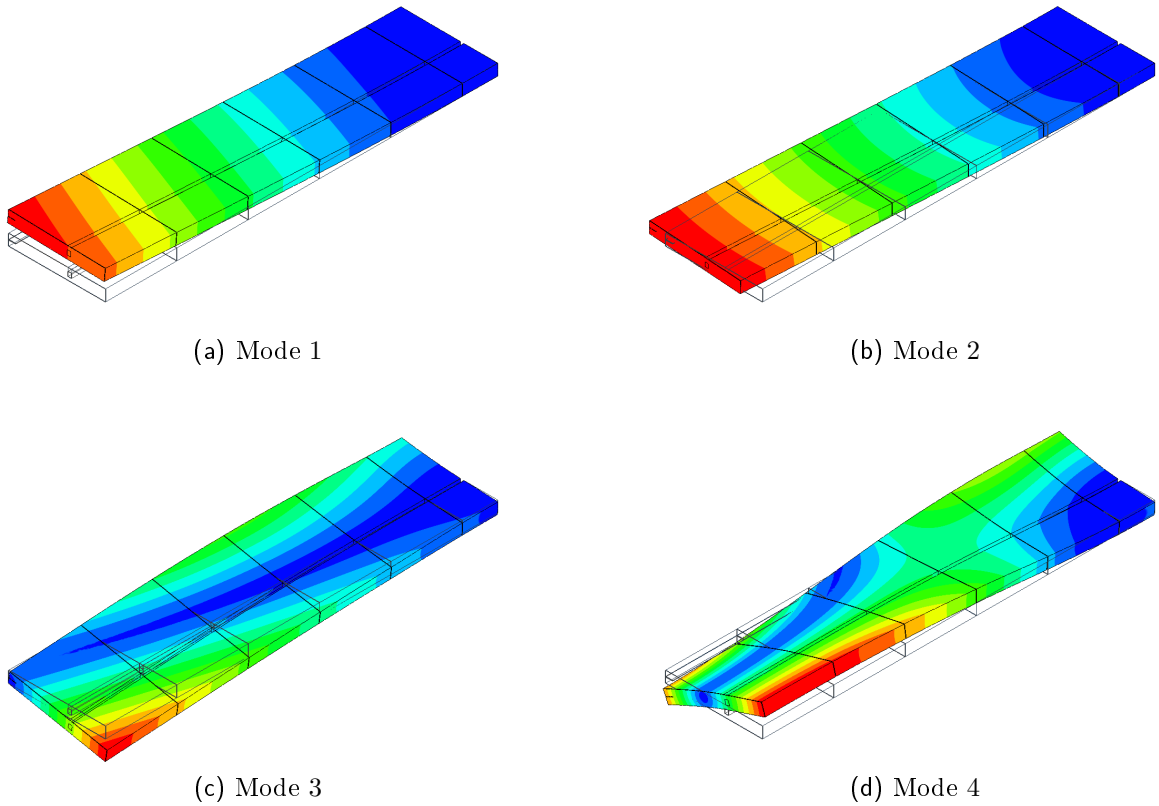

(a) Mode 1

(b) Mode 2

(c) Mode 3

(d) Mode 4

Figure 7.12: Cantilevered Wing Mode Shapes

Initially the equivalent beam properties were used in NASTRAN to produce a structural model of the free vibration modes. Later the wing bending stiffness was updated with the stiffness derived from the static loading tests. The mass of the vehicle was also updated with the as built parameters. The same strip theory from Section 3.2.1.2 was applied to the 6 rigid body and 10 structural modes from NASTRAN. This provides a linearized model of the coupled dynamics. Figure 7.13 shows the variation in the flight dynamic poles as the Froude number is changed.

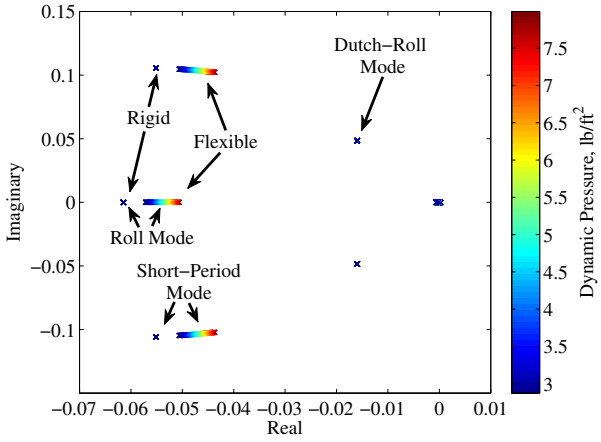

Figure 7.13: Sig Rascal Root Locus

The Dutch roll mode appears to be unaffected by the introduction of flexibility. However, there is a clear change in the short-period and roll modes. The frequency of these modes changes as the velocity is changed due to a change in the reduced natural frequency of the structure. The new wing should therefore provide a measurable change in the flight dynamics that will be identified in the flight testing.

7.4.1.2 Detailed Wing Design

Since the loading applied to the detailed wing design did not include the divergence effects, the deflections shown in Figure 7.14 do not exactly match the preliminary design results. However, the model does still show significant deflections.

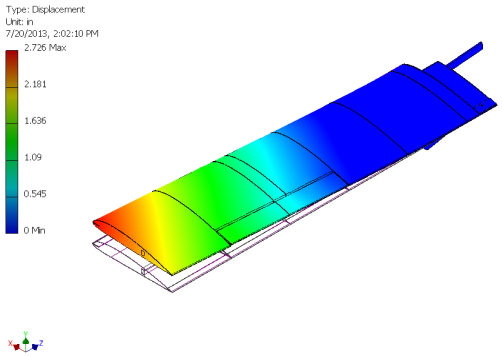

Figure 7.14: Detailed Wing Deflections

The need for the detailed model is also shown by the factor of safety in Figure 7.15. The critical point shown is due to the aileron mounting which was not captured by the preliminary design. The wing was found to be sufficiently strong for the flight tests.

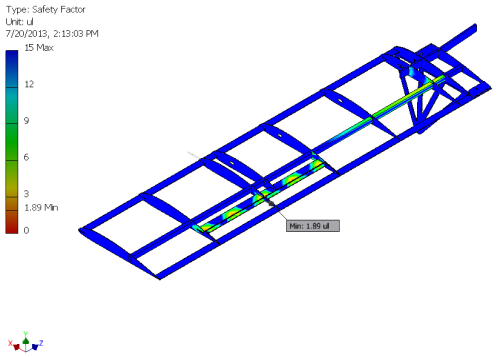

Figure 7.15: Detailed Wing Factor of Safety

7.4.2 Ground Testing

The results of the Ground testing include the calibration curves for the pitot tube and the elevator. The static load test demonstrates the airworthiness and the wing stiffness of the aircraft. Finally the ground vibration tests characterize the structural dynamics in a more controlled environment before the aircraft was flown.

7.4.2.1 Pitot Tube Calibration

The calibration curves for the pitot tube tests in the open-jet windtunnel are shown in Figure 7.16.

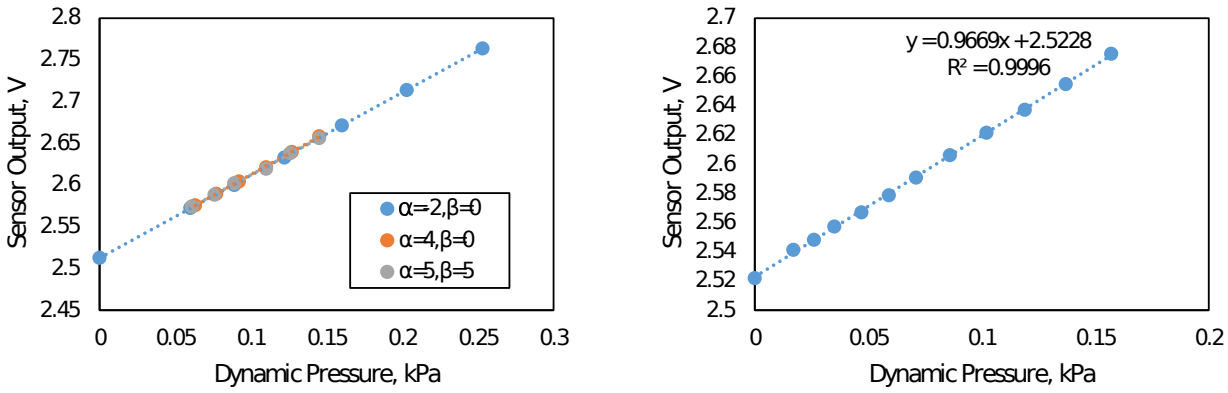

(a) COTS Pitot Tube

(b) ASE Pitot Tube

Figure 7.16: Pitot Tube Calibration Curves

The calibration appears to work very well and does not appear to change with the alignment or the wing used. To examine the independence of the curve on the alignment, the coefficients of the line with the confidence intervals are shown in Figure 7.17.

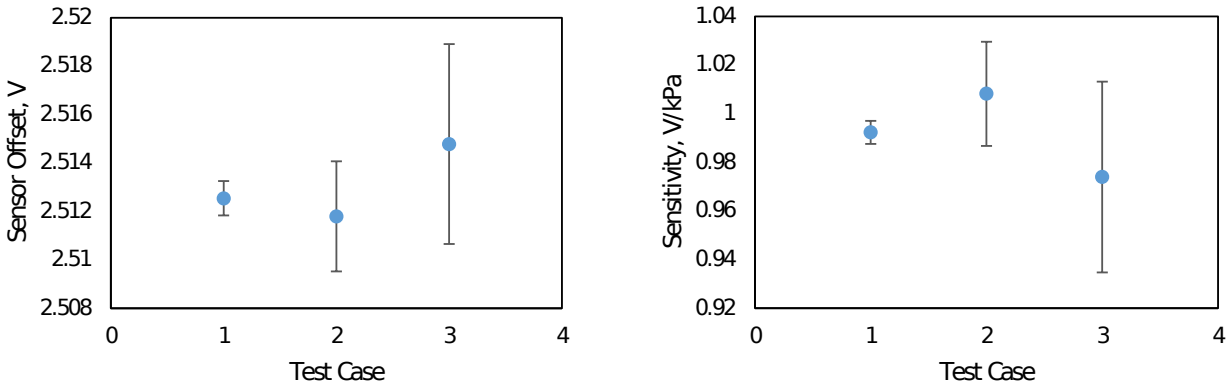

(a) Sensor Offset

(b) Sensitivity

Figure 7.17: Pitot Tube Calibration for Various Alignments

The confidence intervals are large enough that we can conclude that the coefficients for all three models are statistically equivalent. The final curve used in flight tests was calculated by performing a single fit on all of the different alignment cases and for the different wings. The curve shown in Figure 7.18 matches the data very well.

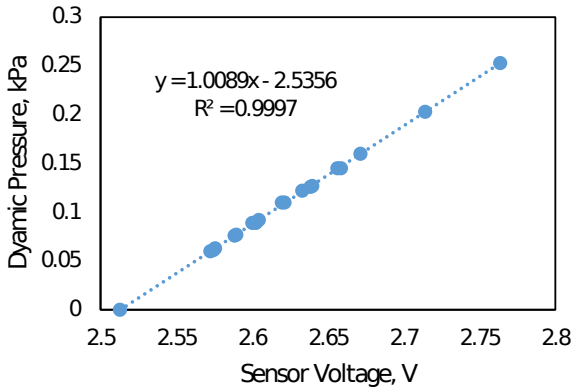

Figure 7.18: Complete Pitot Tube Calibration Curve

7.4.2.2 Elevator Potentiometer Calibration

Initially a linear fit was considered for the elevator calibration shown in Figure 7.19.

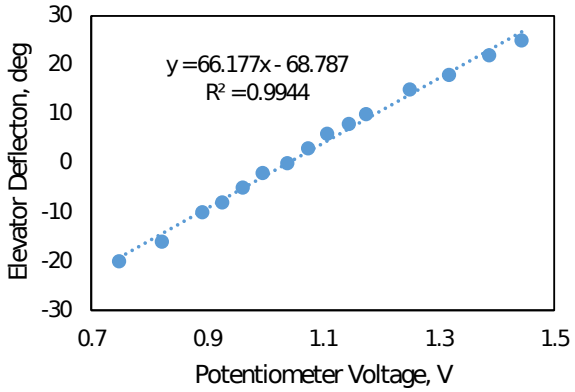

Figure 7.19: Linear Elevator Calibration

The curve appears to fit the data very well, but the residuals in Figure 7.20a shown a very

clear correlation. The correlation is due to non-linearities in the response of the elevator. To account for the non-linearities, a cubic polynomial was used for the calibration.

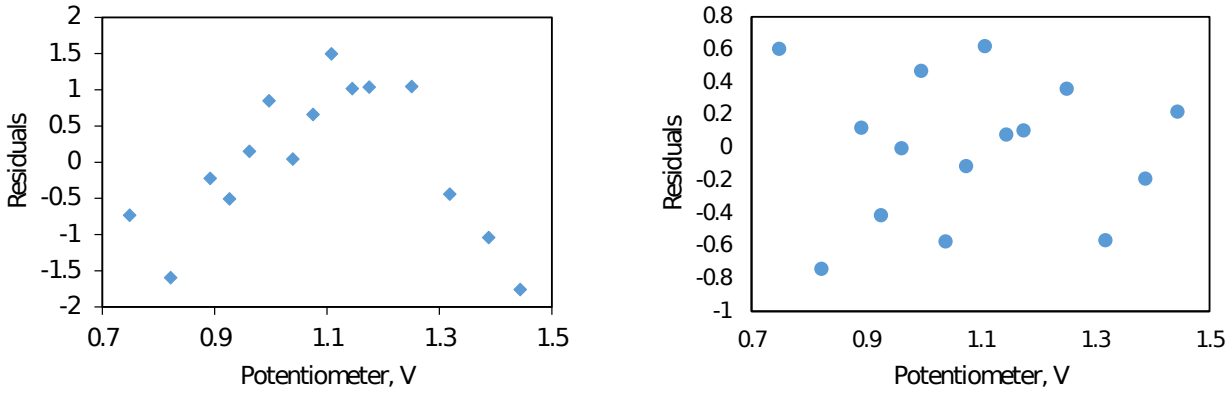

(a) Linear Calibration

(b) Cubic Calibration

Figure 7.20: Elevator Calibration Residuals

The residuals for the cubic calibration curve in 7.20b are random indicating a much better model for the elevator deflections. Thus the elevator deflections were express as a cubic function of the potentiometer voltage.

$$\delta_e = -31.76V_{pot}^3 + 83.73V_{pot}^2 - 54.19^\circ \tag{7.2}$$

7.4.2.3 Static Load Test

The wing shown in Figure 7.21 is clearly able to withstand the significant loads applied to it by the tip test. The magenta dots indicate the measurement points used to calculate the stiffness.

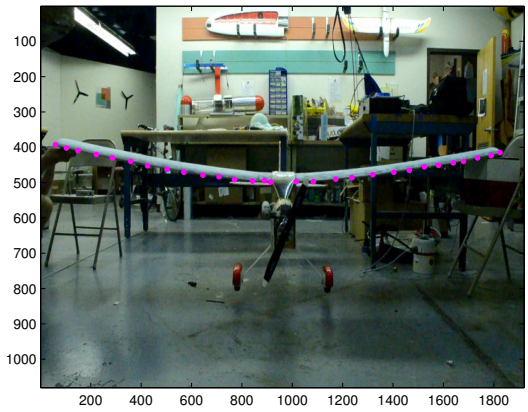

Figure 7.21: Static Load Test

The comparison of the deflections and the value expected from Euler-Bernoulli beam theory is shown in Figure 7.22.

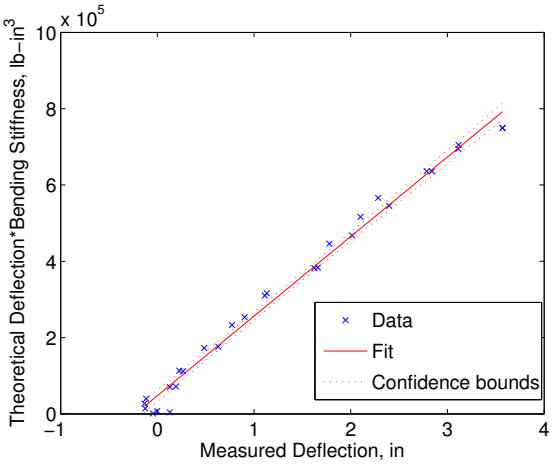

Figure 7.22: Static Load Stiffness Fit

The data appears to match the linear trend very well. Thus the slop of the line give a good estimate of the wing's bending stiffness, $EI = 208\text{lb} - \text{in}^2$.

7.4.2.4 Ground Vibration Tests

Due to the application of the shaker in the aircraft's plane of symmetry, only the symmetric modes were identified. The first 3 modes are shown in Table 7.6.

Table 7.6: ASE Rascal Symmetric Structural Modes

Mode	Frequency	Description
1	5Hz	1st Symmetric Wing Bending
2	14Hz	1st Symmetric Tail Bending
3	20Hz	Landing Gear Mode

7.4.3 Flight Testing

The flight test data was collected over a series of six separate flights shown in Table 7.7. The first three tests were of the commercial off-the-shelf model of the Sig Rascal. There were also three flights of the Rascal with the aeroservoelastic (ASE) wing. During the first and sixth flight there was no data collected due to an error with the data logger.

Table 7.7: Flight Tests

Flight #	Configuration	Date
1	COTS	4/6/2013
2	COTS	4/16/2013
3	COTS	4/16/2013
4	ASE	7/8/2013
5	ASE	7/12/2013
6	ASE	7/23/2013

The data has been broken down into individual maneuvers. Each maneuver, frequency sweeps or doublets, are described in the flight tests cards. These maneuvers were repeated

several times at various velocities, Froude number. A separate model has been identified from each flight test case, to show the variation as the Froude number is changed.

In addition to the response, a plot of the normality of the residuals is shown. These plots arrange the probability distribution such that the data is a straight line for a normal distribution. Ideally the residuals should form a normal distribution.

7.4.3.1 COTS Rascal

With Flight 2 There were 4 separate maneuvers used shown in Table 7.8.

Table 7.8: COTS Rascal Maneuvers

Flight #	Card #	Repetitions	Description
2	8	2	Moderate Speed Doublet
2	9	2	High Speed Doublet
3	5	4	Moderate Speed Frequency Sweep
3	6	1	High Speed Frequency Sweep
3	7	1	Low Speed Frequency Sweep
3	8	1	Moderate Speed Doublet

The first two were moderate speed pitch doublets. The first double, Figure 7.23, does not match well with the angle of attack. Yet, the pitch angle does match very well. This suggests that the poles of the system are reasonable, but that the zeros for the angle of attack did not converge to a correct value. Such a model would be insufficient for controller design, but this model is still useful for examining the frequency of the short-period mode. In contrast, the second example, Figure 7.24, shows a very good match for both outputs. Furthermore, except one tail of the pitch angle, the residuals appear to match very well to the normal distribution. Thus this is a very good model of the aircraft's short-period dynamics. The remaining maneuvers were high speed pitch doublets. The first example, Figure 7.25, shows a good match for both outputs, and the residuals do fit the normal distribution. This example does show an initial mismatch before the pilot began the control inputs. These

initial disturbances are likely due to gusts disturbing the aircraft from the trim, in contrast to the assumption of no process noise. The second high speed doublet, Figure 7.26, also shows a very good match for the model outputs.

The third flight included a total of 7 maneuvers described in Table 7.8. The first 4 maneuvers were frequency sweeps at a moderate trim speed. These sweeps offer a much longer time record where the vehicle was actively excited, resulting in a larger sample size for the identification. This appears to give a much more successful excitation of the system dynamics. The first case, Figure 7.27, shows a very good match. The model does not always capture the peak of the response, but does match quite well. Additionally the residuals do match the normal distribution very well. The second case, Figure 7.28 also shows a very good match in the response and the normality of the residuals. It also is showing the initial disturbances before the control inputs begin that are due to the gusts. The third case, Figure 7.29, overall shows a good match in the response, but the the residuals are not normally distributed. The exception in the match is occurring near the end of the record, where the amplitude of the angle of attack oscillation increases, but the model output does not increase to match. The mismatch is still reasonable and may be due to a gust that could also cause the residuals to no longer be normally distributed. The fourth case, Figure 7.30, gives a good model with a good match of the response and normally distributed residuals. There was also a frequency sweep at a higher trim speed. As with the moderate speed, the high speed sweep, Figure 7.31, shows a good match in the response. Yet, the residuals in the angle of attack deviate from the normal distribution. There was also a sweep a low speed, Figure 7.32. Even though the model output matches the flight test data, the distribution of the residuals deviates from the normal distribution in the tails. There was also a moderate speed pitch doublet, Figure 7.33. This pitch doublet gave a very good model for the response.

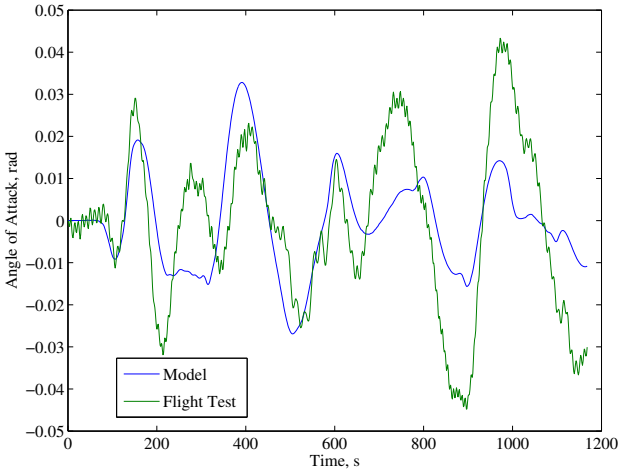

(a) Angle of Attack Response

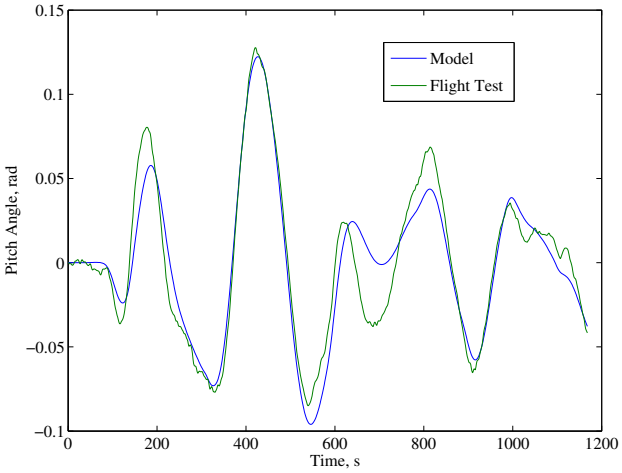

(b) Pitch Angle Response

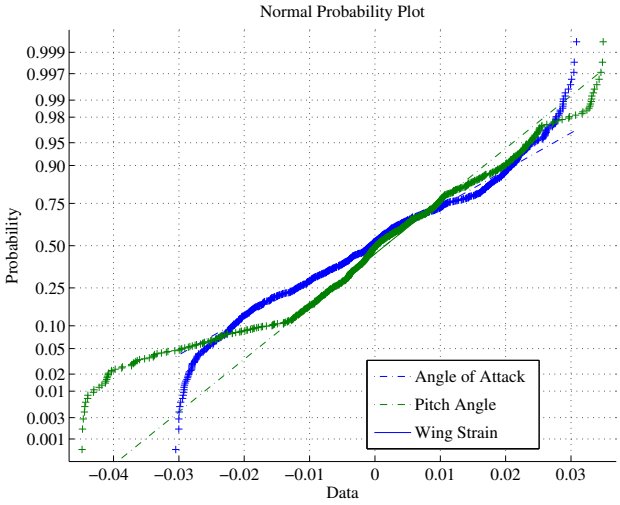

(c) Normality of Residuals

Figure 7.23: COTS Rascal: Flight 2, Card 8-1

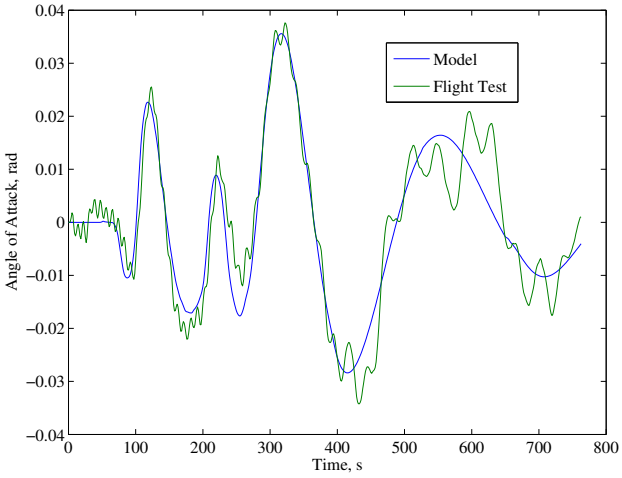

(a) Angle of Attack Response

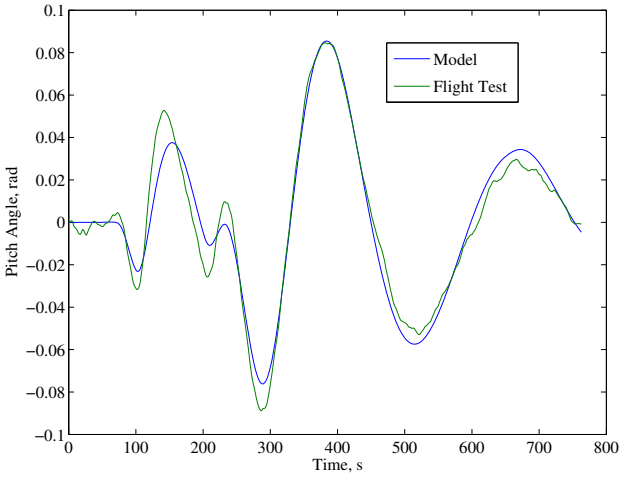

(b) Pitch Angle Response

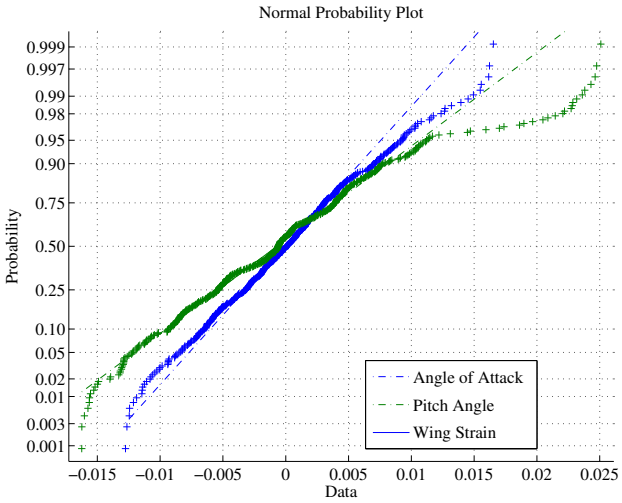

(c) Normality of Residuals

Figure 7.24: COTS Rascal: Flight 2, Card 8-2

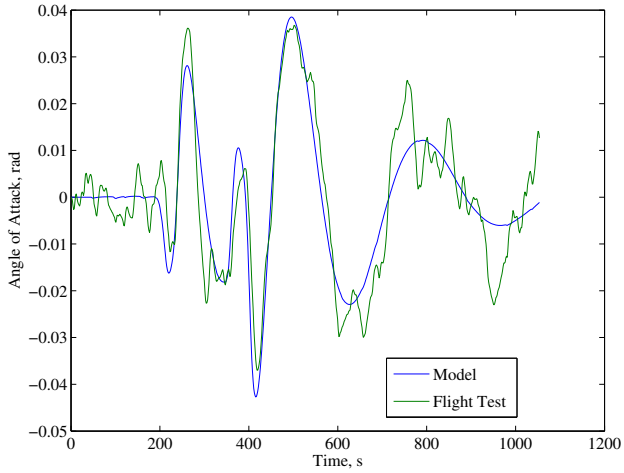

(a) Angle of Attack Response

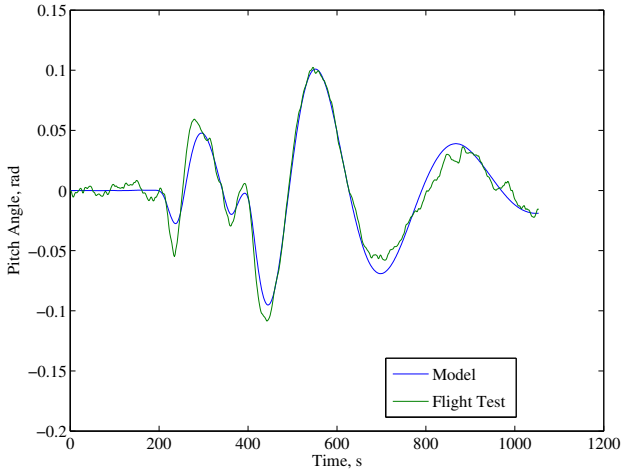

(b) Pitch Angle Response

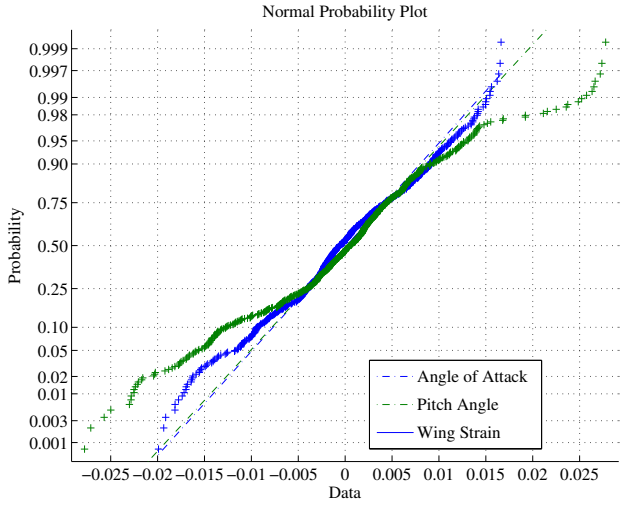

(c) Normality of Residuals

Figure 7.25: COTS Rascal: Flight 2, Card 9-1

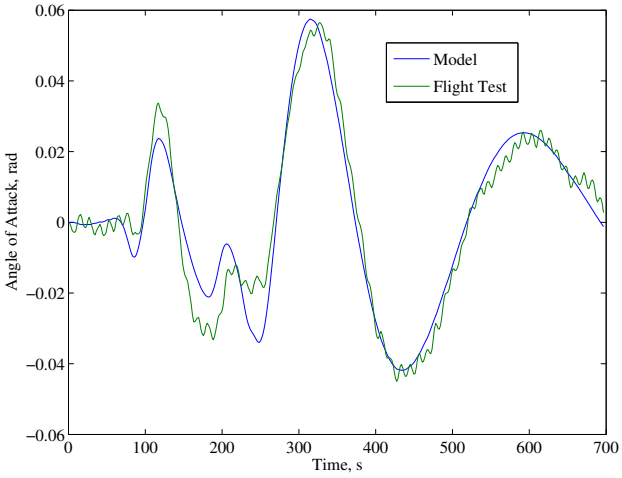

(a) Angle of Attack Response

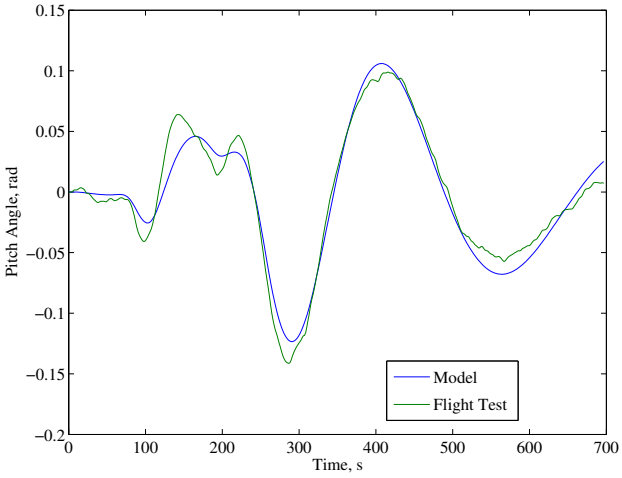

(b) Pitch Angle Response

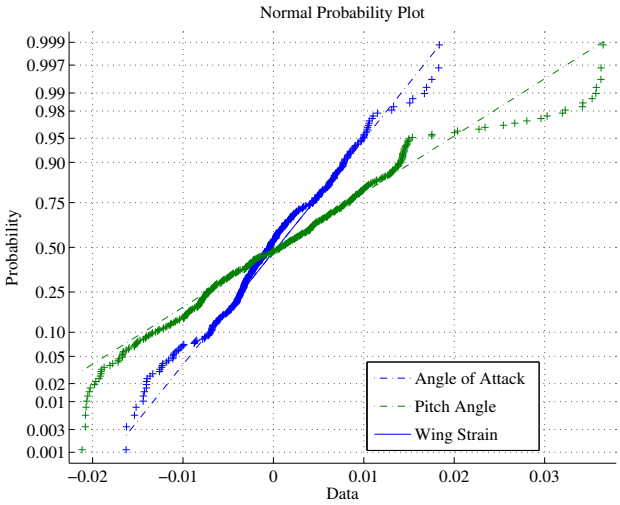

(c) Normality of Residuals

Figure 7.26: COTS Rascal: Flight 2, Card 9-2

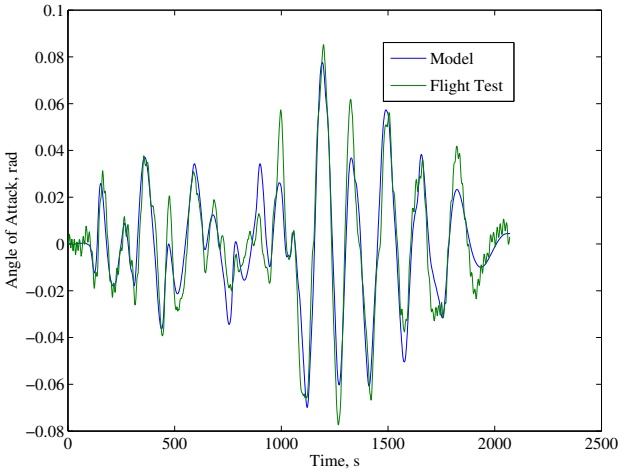

(a) Angle of Attack Response

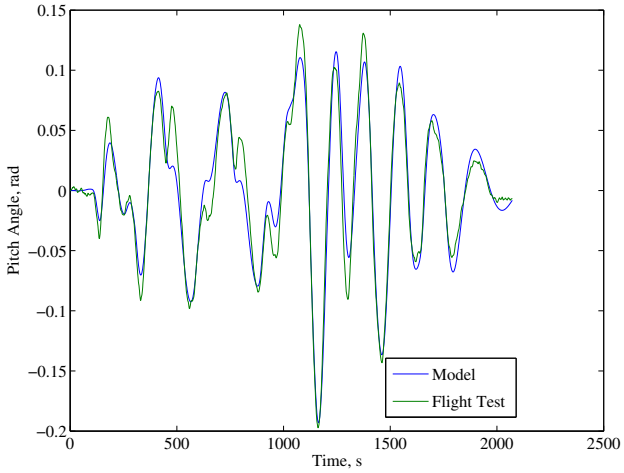

(b) Pitch Angle Response

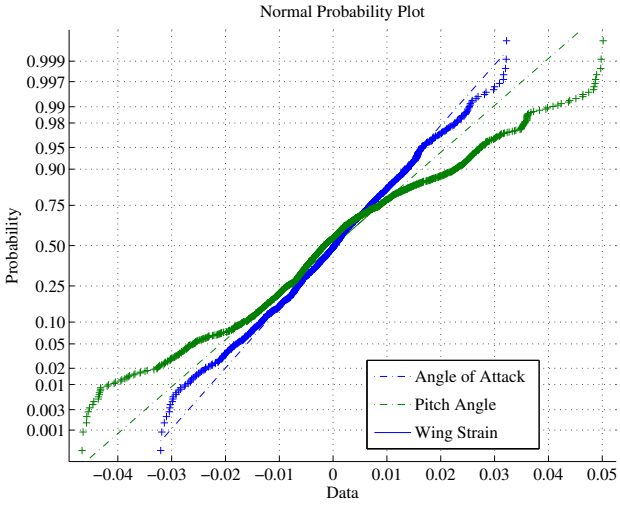

(c) Normality of Residuals

Figure 7.27: COTS Rascal: Flight 3, Card 5-1

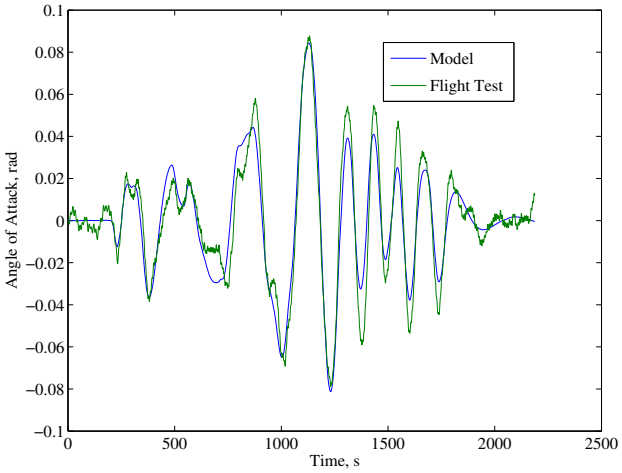

(a) Angle of Attack Response

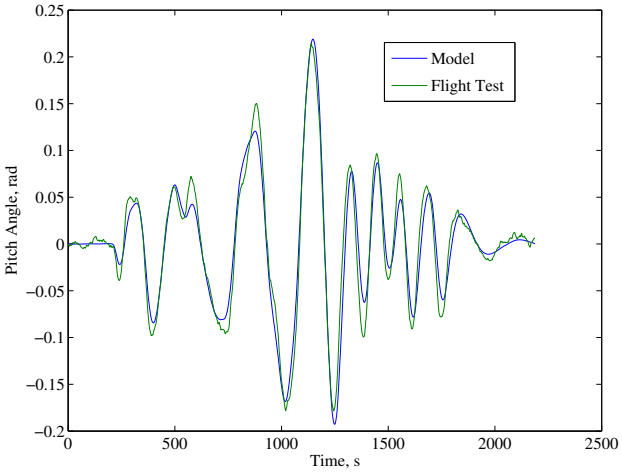

(b) Pitch Angle Response

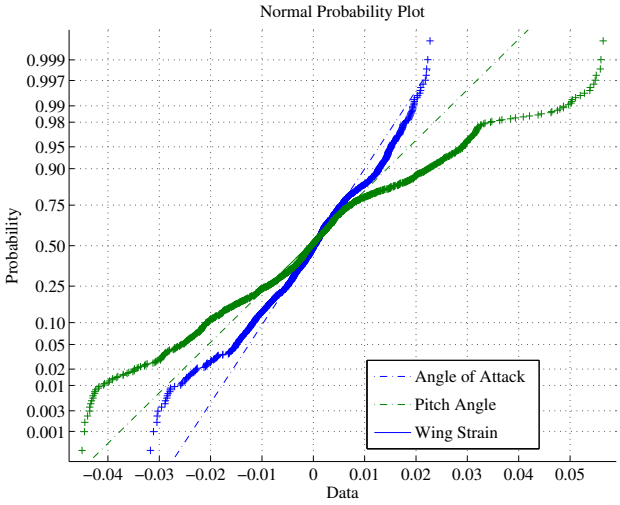

(c) Normality of Residuals

Figure 7.28: COTS Rascal: Flight 3, Card 5-2

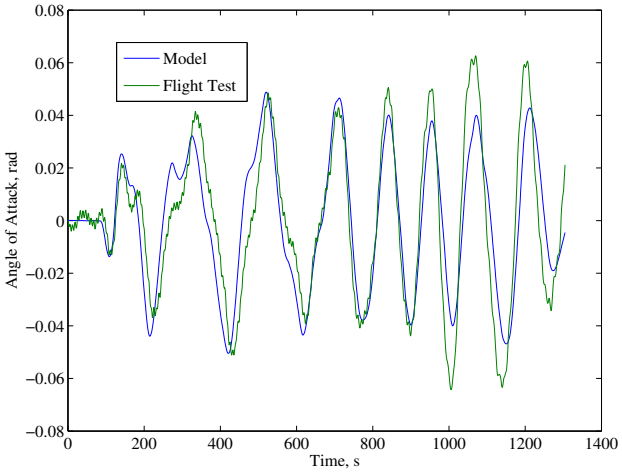

(a) Angle of Attack Response

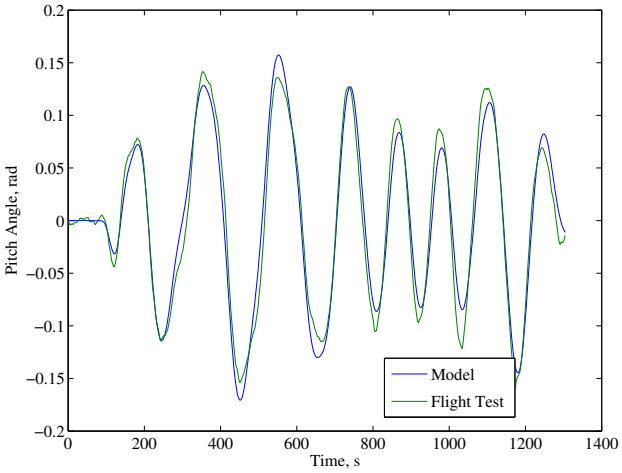

(b) Pitch Angle Response

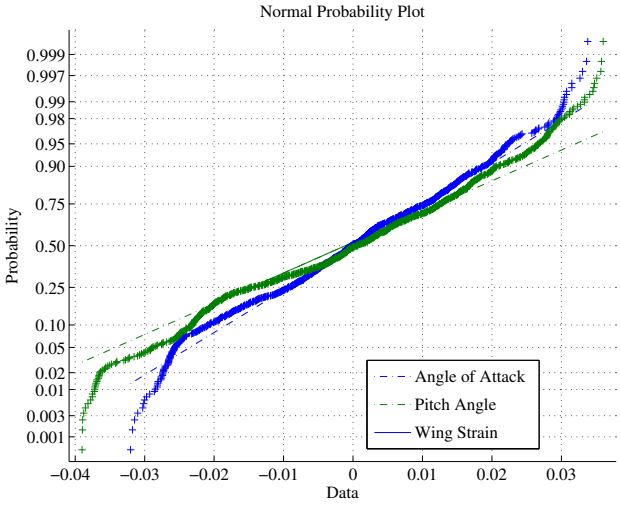

(c) Normality of Residuals

Figure 7.29: COTS Rascal: Flight 3, Card 5-3

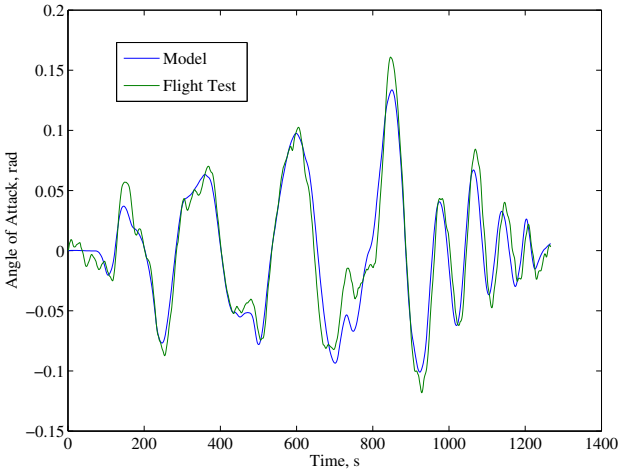

(a) Angle of Attack Response

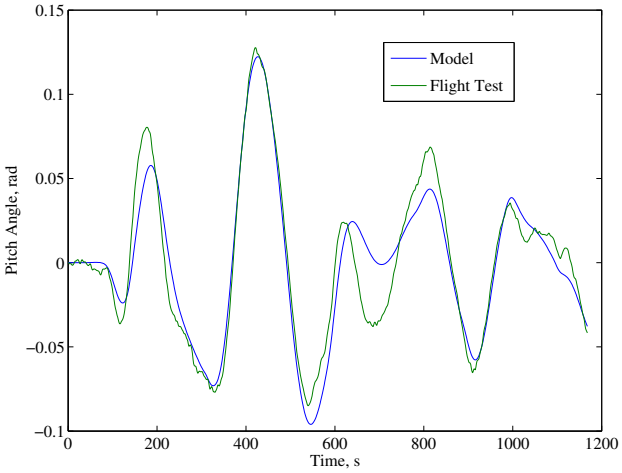

(b) Pitch Angle Response

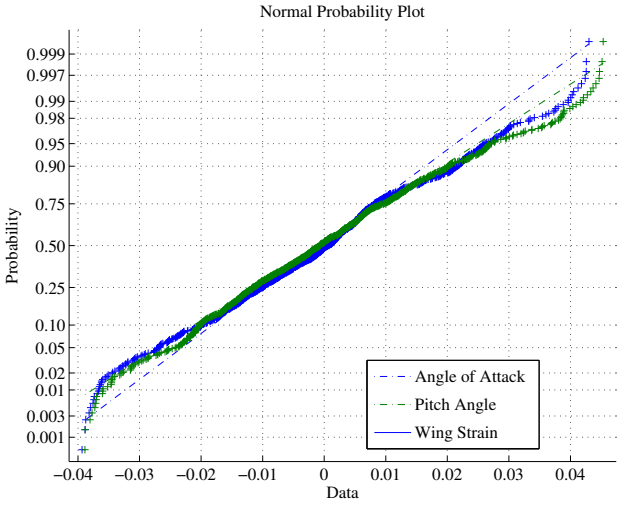

(c) Normality of Residuals

Figure 7.30: COTS Rascal: Flight 3, Card 5-4

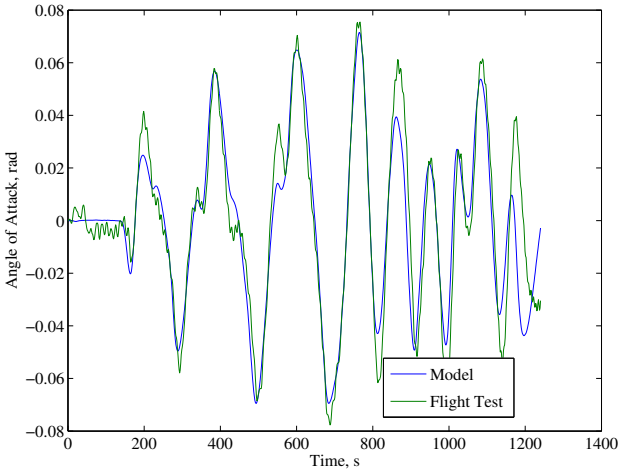

(a) Angle of Attack Response

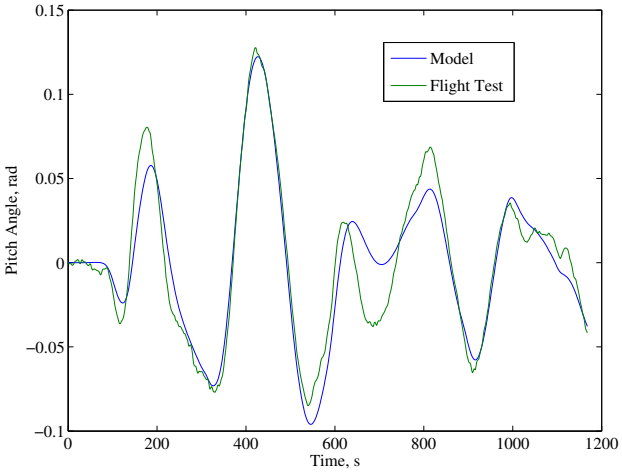

(b) Pitch Angle Response

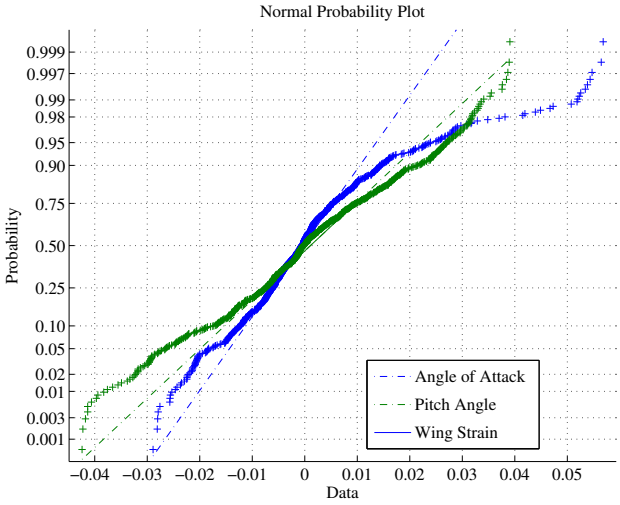

(c) Normality of Residuals

Figure 7.31: COTS Rascal: Flight 3, Card 6-1

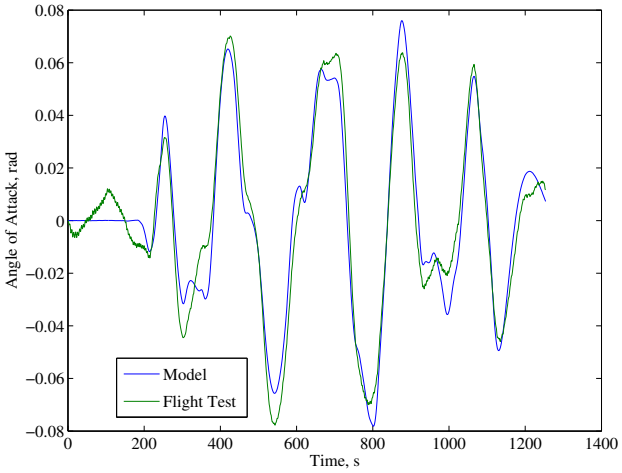

(a) Angle of Attack Response

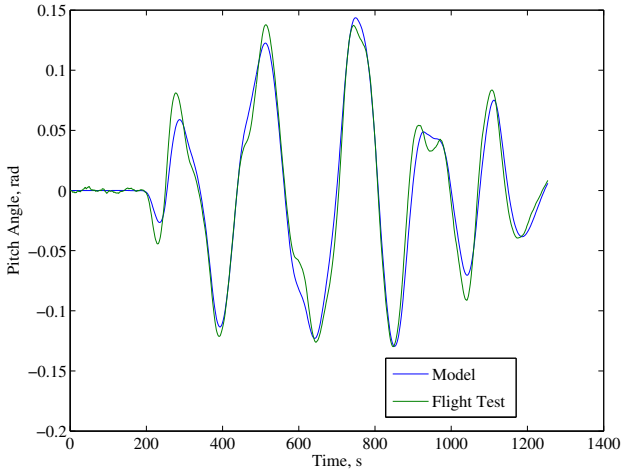

(b) Pitch Angle Response

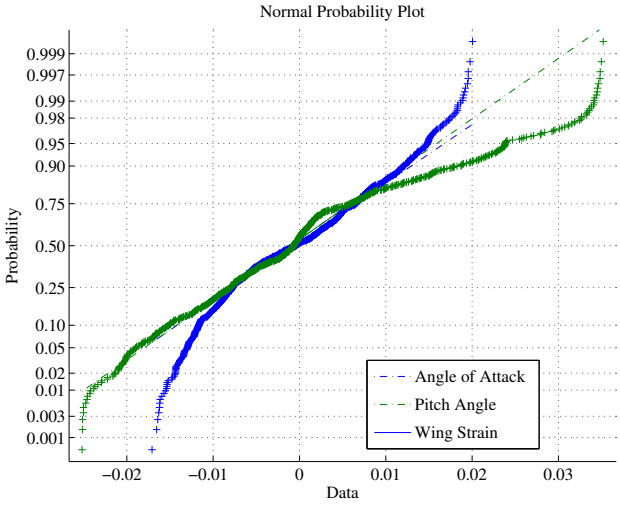

(c) Normality of Residuals

Figure 7.32: COTS Rascal: Flight 3, Card 7-1

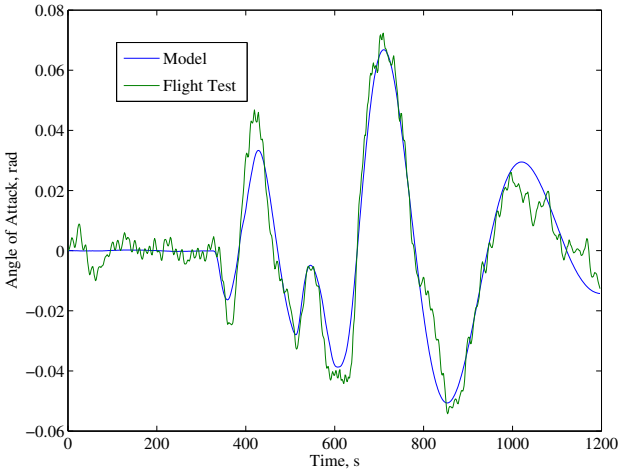

(a) Angle of Attack Response

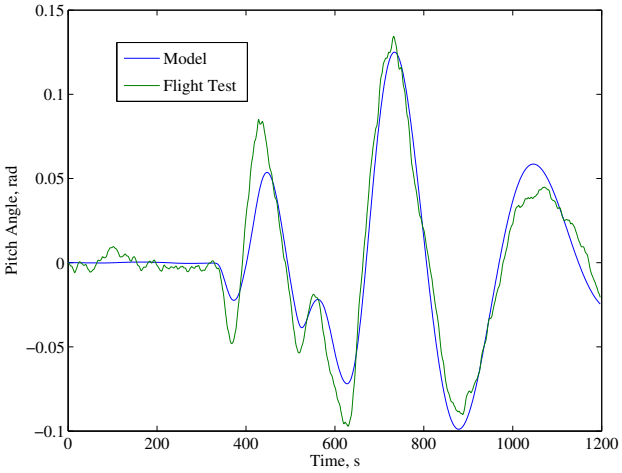

(b) Pitch Angle Response

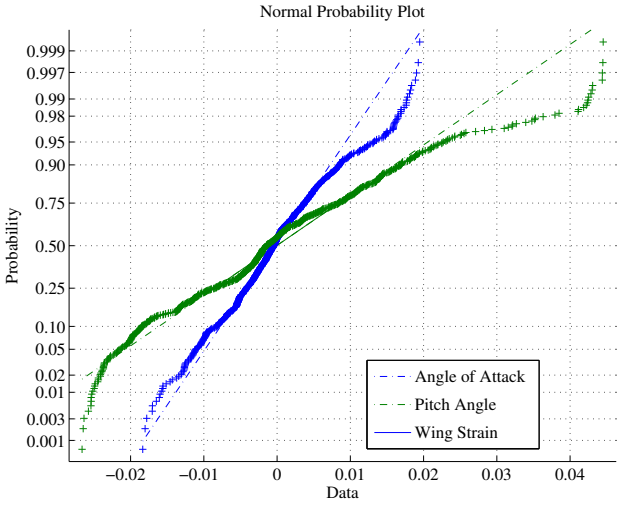

(c) Normality of Residuals

Figure 7.33: COTS Rascal: Flight 3, Card 8-1

7.4.3.2 ASE Rascal

The first flight test of the flexible wing, Flight 4, included 3 maneuvers in Table 7.9.

Table 7.9: ASE Rascal Maneuvers

Flight #	Card #	Repetitions	Description
4	5	1	Moderate Speed Frequency Sweep
4	6	1	High Speed Frequency Sweep
4	7	1	Low Speed Frequency Sweep
5	5	1	Moderate Speed Frequency Sweep
5	11	5	Moderate Speed 3-2-1 Doublet
5	12	2	High Speed 3-2-1 Doublet

The frequency sweep at a moderate speed is shown in Figure 7.34. The initial response does not match very well. However, as the amplitude of the response increased, the model output matches much better. The residuals do fit the normal distribution quite well. The frequency sweep at a high trim speed, Figure 7.35, gave a very good model. The frequency sweep at a low speed, Figure 7.36, does not match the angle of attack output well. Yet the other outputs do match quite well. Also the outputs are normally distributed even for the angle of attack. Therefore this model was considered to be acceptable for the identification of the short-period frequency.

A total of 4 maneuvers were used from Flight 5 shown in Table 7.9. The winds were higher during the 5th flight. Thus several of the maneuvers show a noisier response. There as one frequency sweep at a moderate flight speed, Figure 7.37. Again the frequency sweep data gave a good model that fits the response and has normally distributed residuals. The remaining maneuvers were $3-2-1$ doublets. Many of these maneuvers resulted in very large large amplitude responses. Also, the noise for these maneuvers appears to be greater. Due to these difficulties, only 2 examples at a moderate speed were used. The first, Figure 7.38, does not match the angle of attack or pitch angle outputs. The strain outputs do match reasonably well, but there is a high frequency content that is leading to appreciable errors. Because the errors are still normally distributed, it appears that the model is at least capturing the bending of the wing from the short-period mode, and thus the frequency of the short-period mode. The second moderate speed case, Figure 7.39, shows the high frequency

noise in all three of the outputs, but overall appears to match the response slightly better. One $3-2-1$ doublet at a high trim speed was also used, Figure 7.40. The model output for the angle of attack and pitch angle do not match well. Yet, the wing strain does do a reasonable job matching the flight test data. Additionally, since the residuals are normally distributed, the resulting model was considered to be acceptable for the frequency of the short-period mode.

The Rascal with the aeroservoelastic appears to be much more susceptible to gust disturbances. Unfortunately the servo dynamics are not fast enough to effectively excite the structural modes. The gusts are exciting the structural modes as much as the elevator inputs. Since the output error is assuming that there is no process noise such as gusts, the output error was not effective for identifying an accurate and consistent model for the structural dynamics. Fortunately, it did still work quite well for identifying the short-period mode.

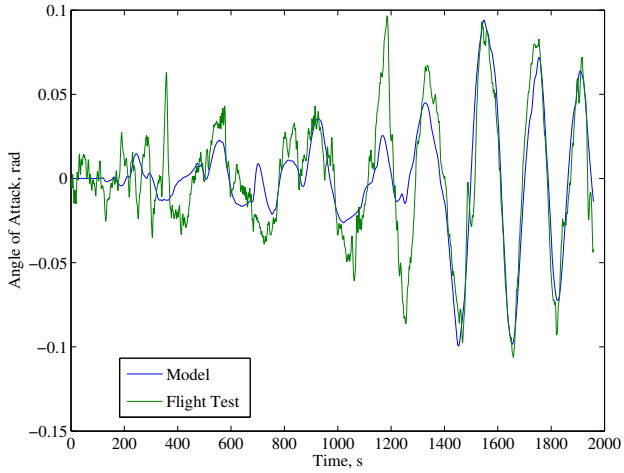

(a) Angle of Attack Response

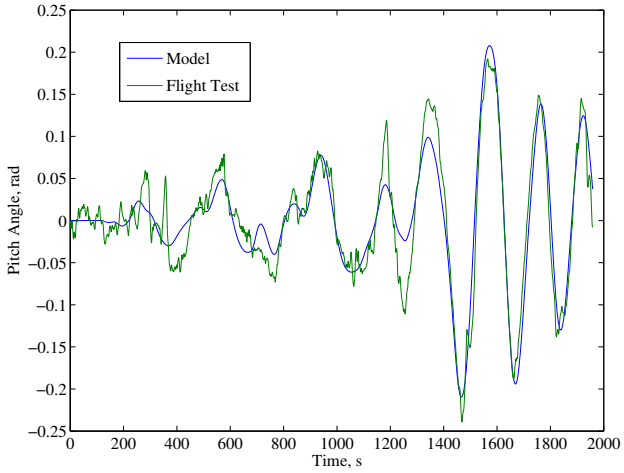

(b) Pitch Angle Response

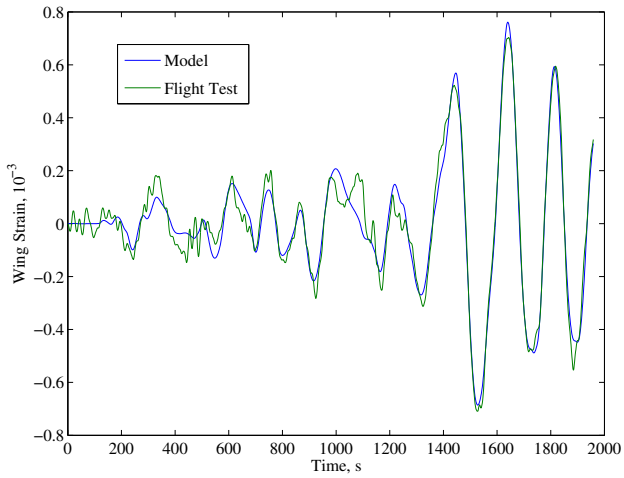

(c) Wing Strain Response

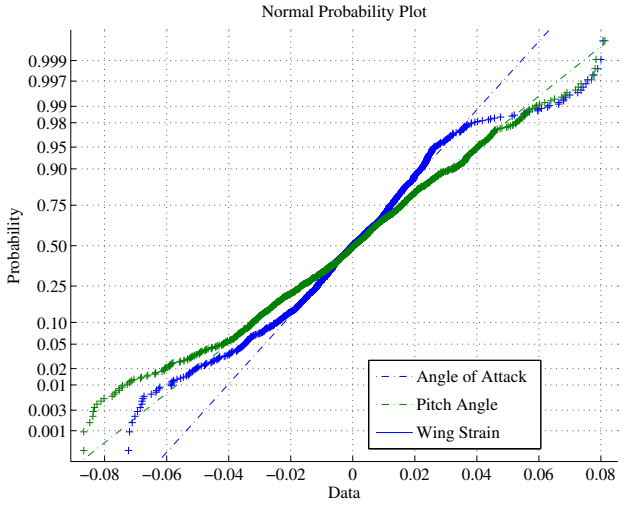

(d) Normality of Residuals

Figure 7.34: ASE Rascal: Flight 4, Card 5-1

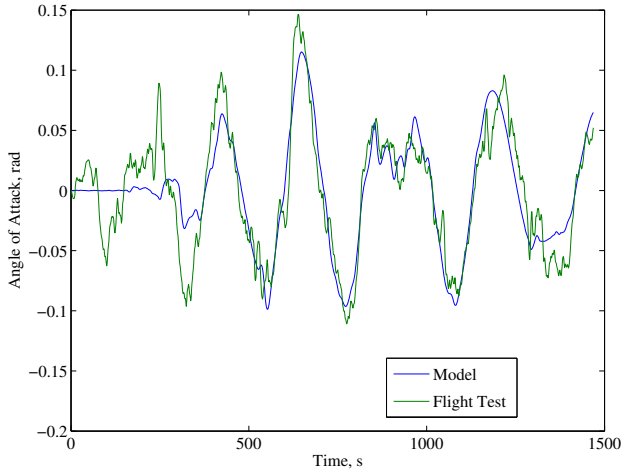

(a) Angle of Attack Response

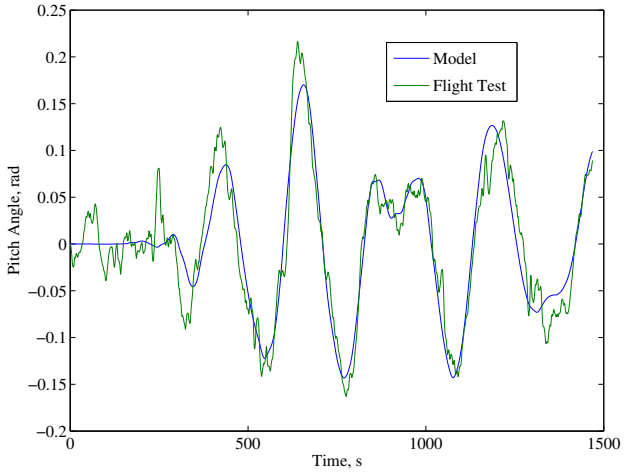

(b) Pitch Angle Response

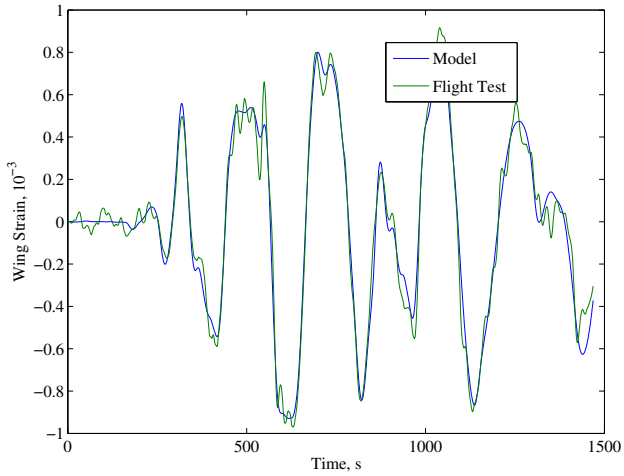

(c) Wing Strain Response

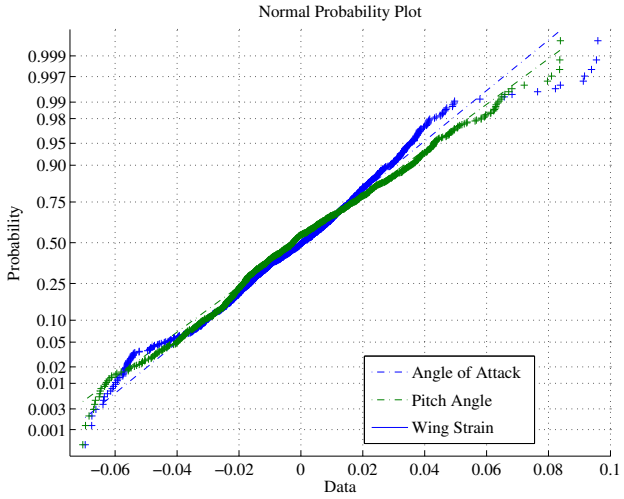

(d) Normality of Residuals

Figure 7.35: ASE Rascal: Flight 4, Card 6-1

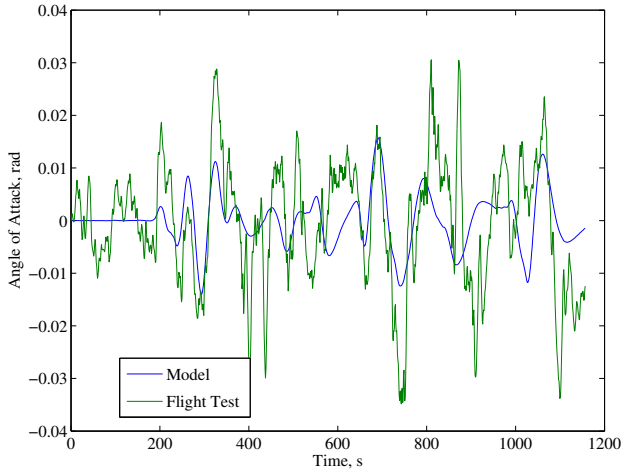

(a) Angle of Attack Response

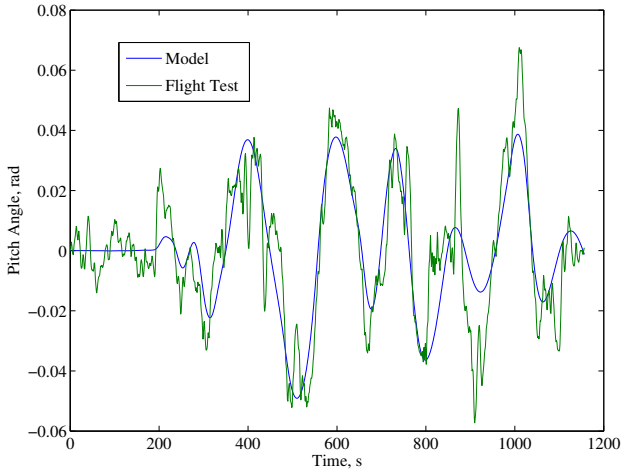

(b) Pitch Angle Response

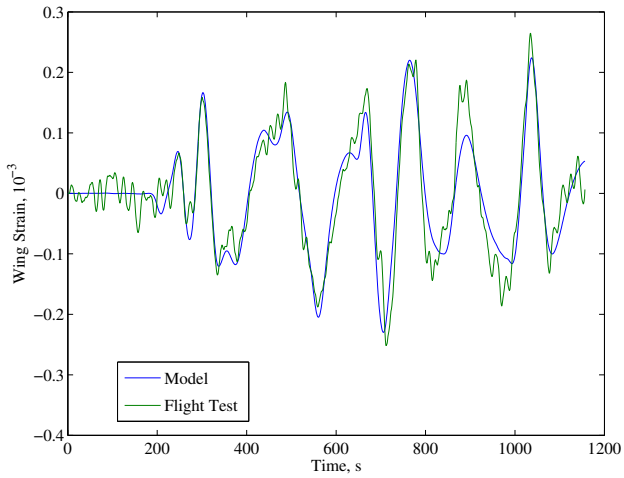

(c) Wing Strain Response

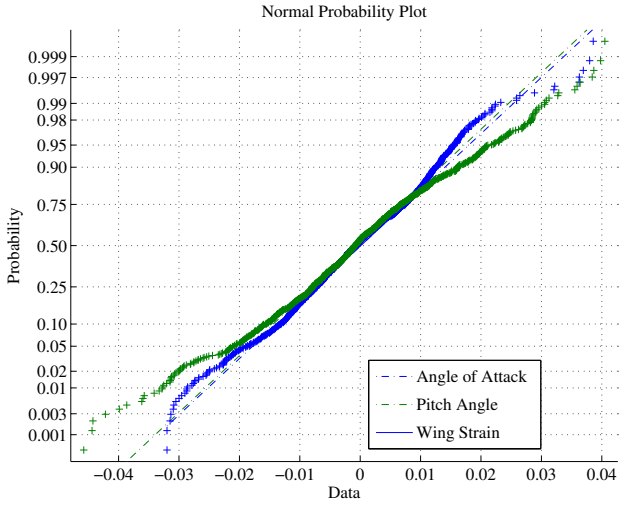

(d) Normality of Residuals

Figure 7.36: ASE Rascal: Flight 4, Card 7-1

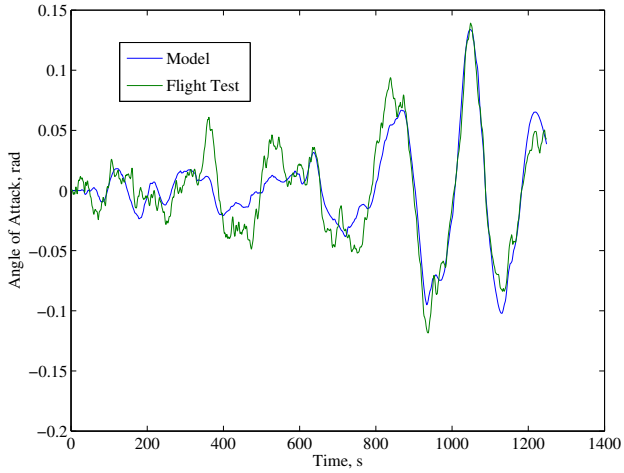

(a) Angle of Attack Response

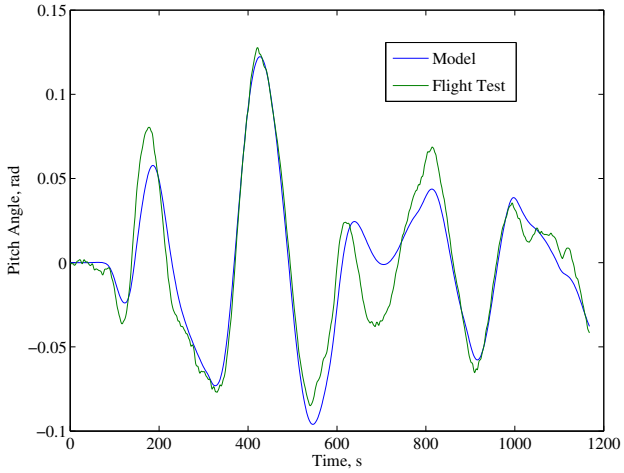

(b) Pitch Angle Response

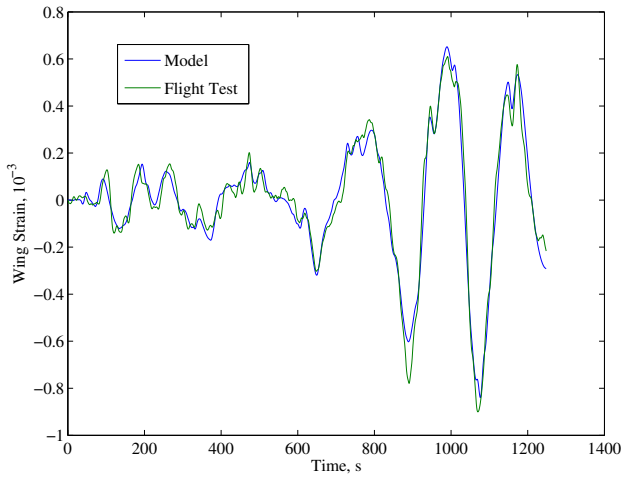

(c) Wing Strain Response

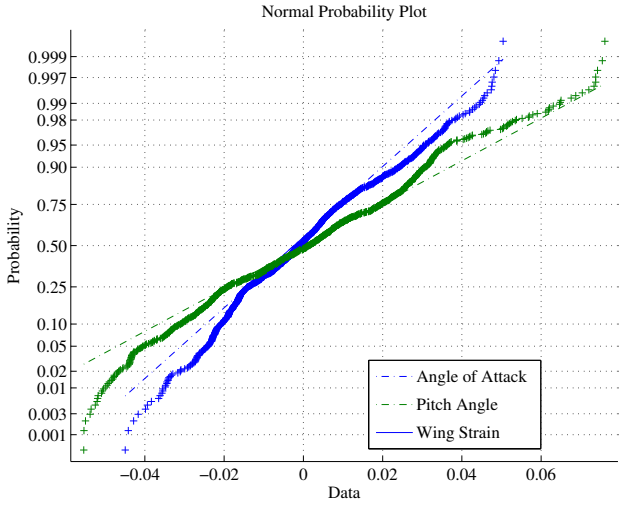

(d) Normality of Residuals

Figure 7.37: ASE Rascal: Flight 5, Card 5-1

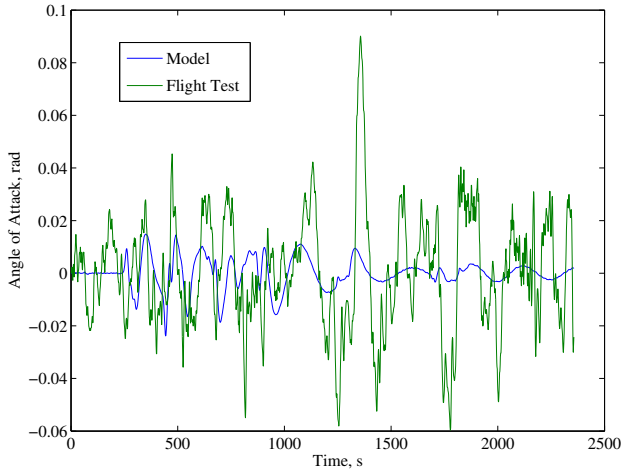

(a) Angle of Attack Response

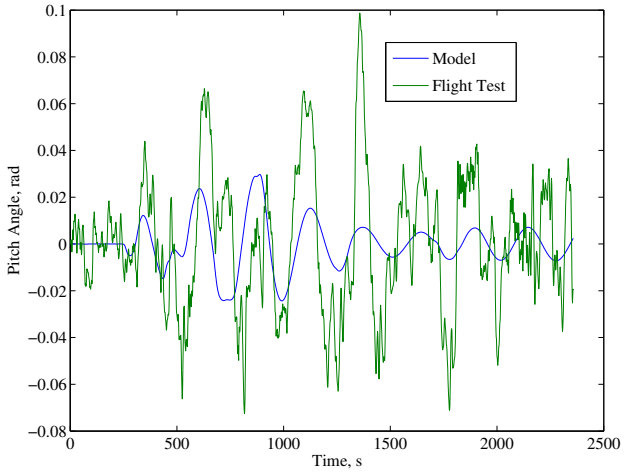

(b) Pitch Angle Response

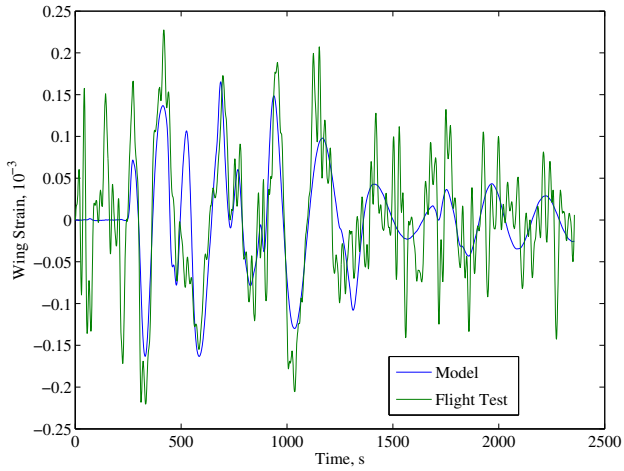

(c) Wing Strain Response

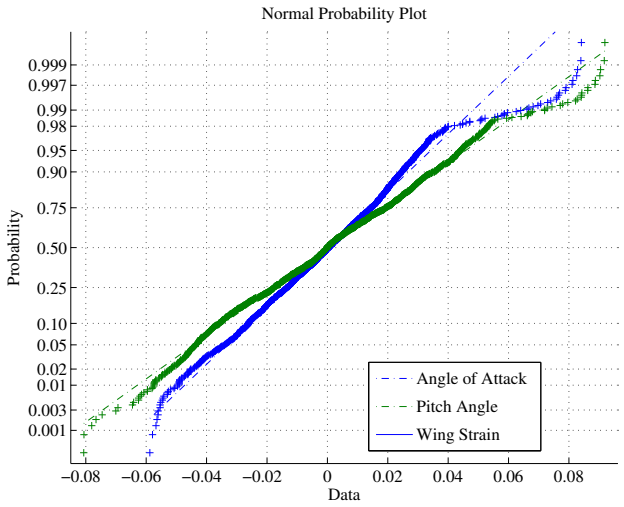

(d) Normality of Residuals

Figure 7.38: ASE Rascal: Flight 5, Card 11-4

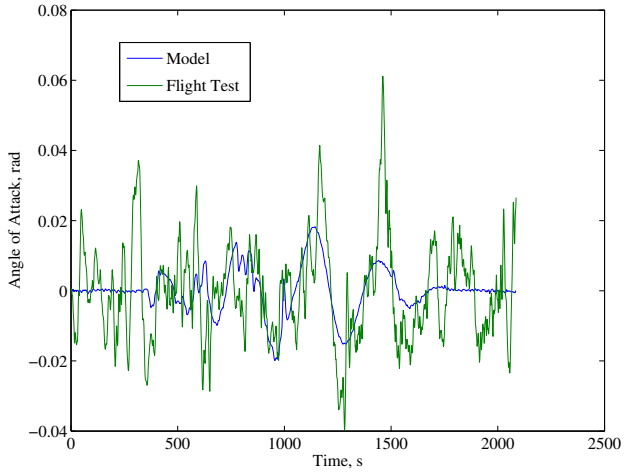

(a) Angle of Attack Response

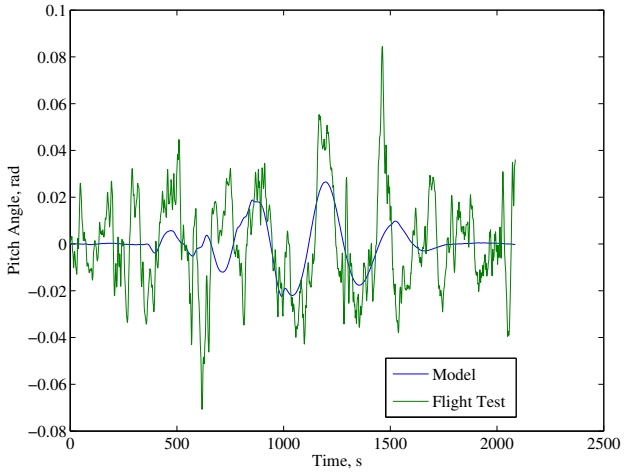

(b) Pitch Angle Response

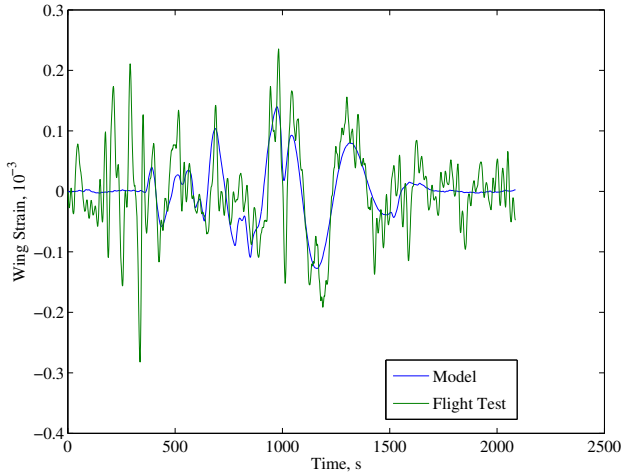

(c) Wing Strain Response

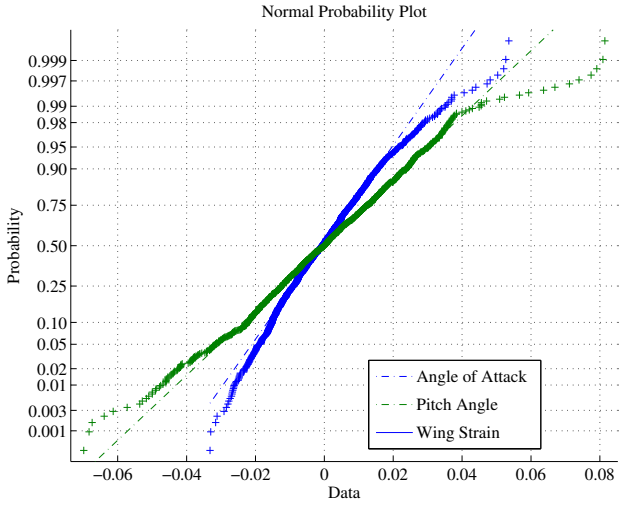

(d) Normality of Residuals

Figure 7.39: ASE Rascal: Flight 5, Card 11-5

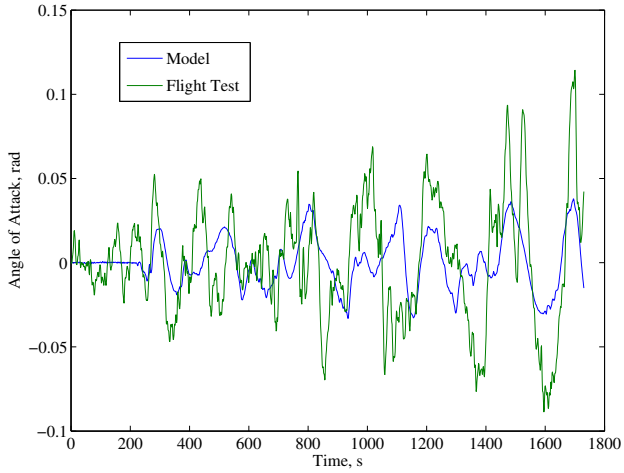

(a) Angle of Attack Response

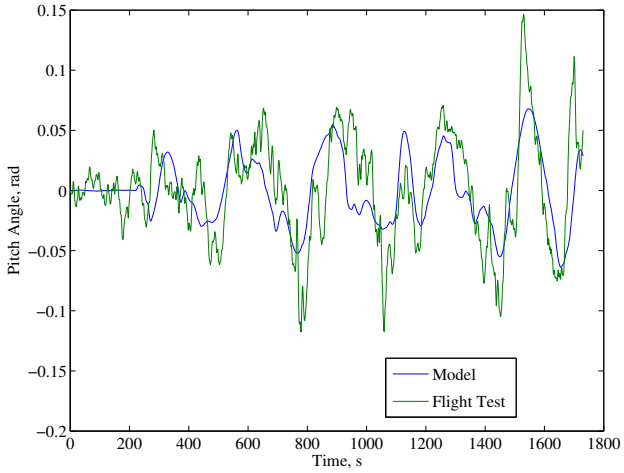

(b) Pitch Angle Response

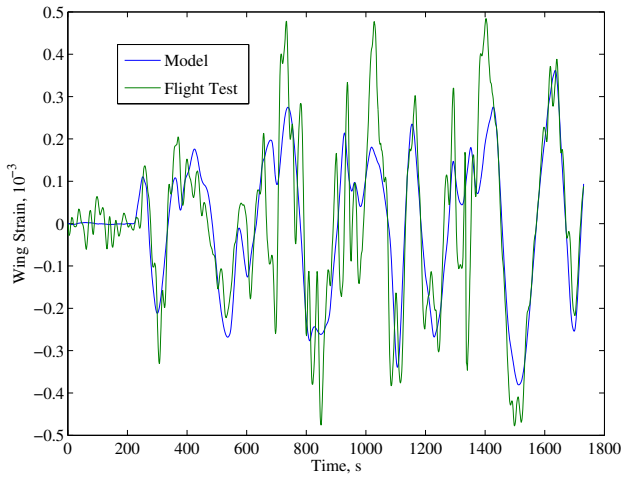

(c) Wing Strain Response

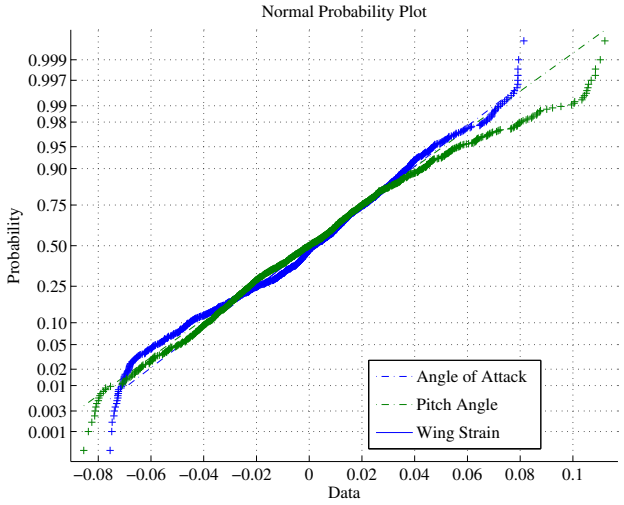

(d) Normality of Residuals

Figure 7.40: ASE Rascal: Flight 5, Card 12-1

7.4.3.3 Comparison of Configurations

Typically, the model is validated by using a separate set of data to show that the model response is consistent. In contrast, the present work is attempting to show how the model changes with the dynamic pressure. A single model may not match a separate set of data at a different dynamic pressure. Thus, the consistency of the response is demonstrated by examining the trend of the frequency of the short-period mode.

As the dynamic pressure changes, only the Froude number and the reduced structural frequencies are effected. The variations in the short-period mode from the simulation used in the preliminary wing design are shown in Figure 7.41a. The rigid 6-DoF model has no structural stiffness, so only the Froude number is effected. As a result, there is no change in the frequency of the short-period mode. In contrast, when the effects of the reduced structural frequency are included, there is a slight decrease in the frequency of the short-period mode. The frequency is appearing to decrease linearly with the dynamic pressure.

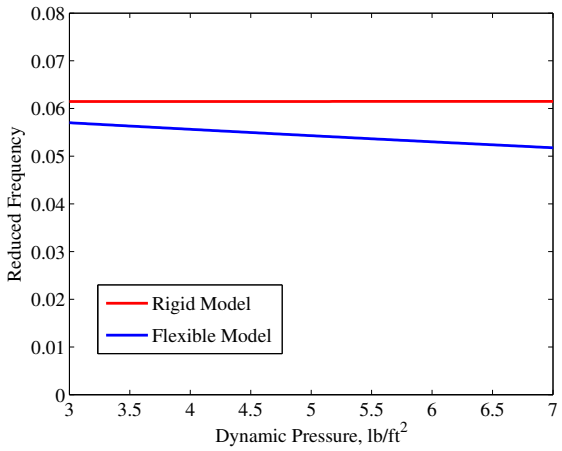

(a) Strip Theory Simulation

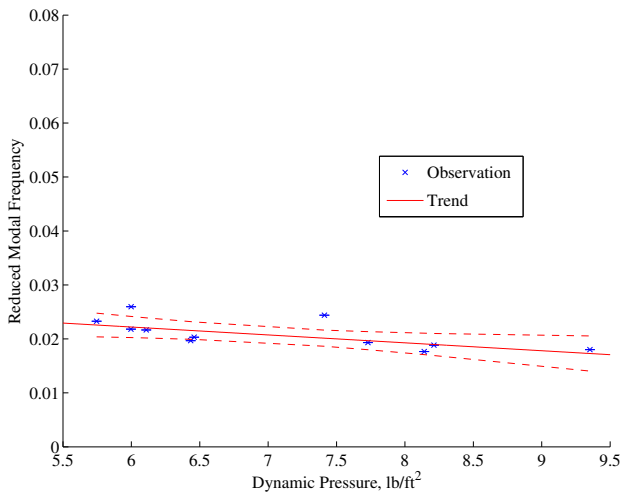

(b) COTS Rascal

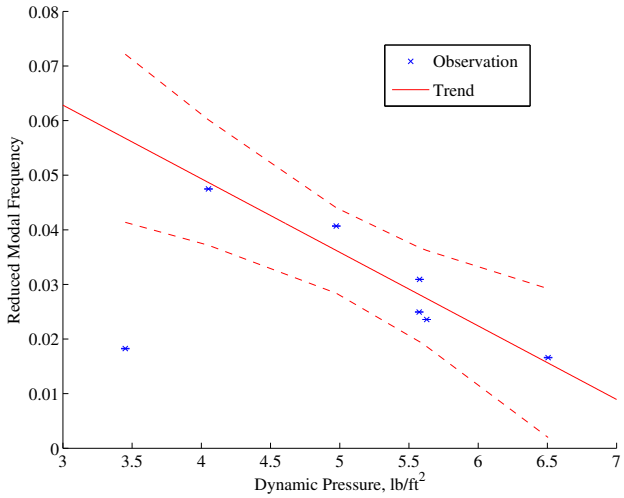

(c) ASE Rascal

Figure 7.41: Variations in the Frequency of the Short-Period Mode

These variations in the short-period frequency of the COTS aircraft are shown in Figure 7.41b. The models shown in Section 7.4.3.1 match the vehicle response very well. As a result, the linear fit matches the flight test data quite well. A bilinear fit was used to reduce the influence of any outliers. This robust linear curve gives a slope of -0.0017 ± 0.0015. Although the vehicle is very stiff, it is impossible to make the vehicle rigid so there is still a slight decrease in the frequency.

The data for the ASE Rascal in Section 7.4.3.2, were much noisier. As a result, the uncertainty in the trend in Figure 7.41c is much larger. Yet the same bilinear fit gives a slope of -0.0141 ± 0.0084. Because the error of the model is very sensitive to the frequencies, the estimates of the individual frequencies have a low uncertainty. However, systematic errors in the design of the experiment can result in a large variation between samples. These errors can include differences in air pressure due to the vehicle altitude or errors in trim so that the aircraft is actually climbing. As a result of these systematic errors, the flight test data does not give a precise value for the slope though. Despite the large uncertainty in the measure of the slope, we still reject the null hypothesis and conclude that there is a significant trend. Thus the flight test has shown that the frequency of the short-period mode is correlated to the Froude number. Even with the uncertainty, the frequency of the simulation is not decreasing as much as the flight tests data. This difference between the simulation and the flight test data is likely due to the inaccuracy in the structural model.

Chapter 8

Conclusions and Future Work

8.1 Conclusions

The objective of this dissertation is the development of tools for the examination and evaluation of the effect of a flexible structure on next generation flight controls, especially adaptive controls. These tools include modeling of a flexible aircraft, scaling laws for creating a subscale vehicle, and flight testing to validate the theory.

A numerical simulation was developed for nonlinear simulations of a flexible vehicle. By using a mean axis system, the non-linear flight dynamics and the linear structural dynamics are orthogonal. This orthogonality allowed for the use of separate and relevant aerodynamic models which better represented the physics of the associated dynamics. The model developed was used to simulate a subscale model of a commercial aircraft. The flexibility of the aircraft led to coupling between flight dynamics and aeroelasticity. It was shown that as the stiffness of the vehicle was increased the dynamics converged toward the expected rigid vehicle. After applying an output feedback model reference adaptive controller, there is a clear demonstration of this model's ability to capture the degradation of the controller's performance, and the excitation of the structure. The adaptive controller was shown to be capable of aggravating the structural excitation.

The next level of capability was the development of scaling laws that would allow for the creation of a subscale model. The subscale model has the structural interactions similar to a fullscale vehicle. A complete set of scaling laws was demonstrated that would achieve complete similitude. The scaling laws were based on mean axis parametrization of a flexible aircraft. Partial similitude was also examined. The partial similitude was used to match the coupling between the structural dynamics and the short-period mode. First by examining a reduced order model based on the short-period approximation. This reduces to total parameters present in the system. Second the sensitivity of the system response to the vehicle's non-dimensional Π-groups. This shows the parameters which have the greatest impact on the response. Both methods showed the Froude number matching was found to be less significant than the structural stiffness. The difference in Froude number means that it is possible to flight test the vehicle at a lower flight speed. As a trade off, the structural stiffness must be scaled to account for the reduced dynamic pressure. For example a 10% reduction in velocity would require an 19% reduction in structural stiffness.

The final piece is a series of flight tests that showed the ability to use a subscale vehicle to demonstrate these interactions and to validate the results of the scaling theory. A very flexible wing was designed for a Sig Rascal. Using the very stiff off-the-shelf wing and the flexible wing, a comparison of the short-period mode of the two wings was undertaken. Using a time domain output error method a model was created for the aircraft's short-period mode. The stiffer wing showed a more precise, but ultimately statistically insignificant trend. The more flexible wing showed decrease in the short-period mode as the Froude number of the vehicle was increased.

8.2 Future Work

The modeling work could be expanded by incorporating a higher fidelity aerodynamic model. The higher fidelity aerodynamic model could be used with alternative basis functions in the surrogate model to examine non-linear effects such as stall.

The scaling could be easily expanded to examine the lateral dynamics such as roll and dutch-roll modes. The sensitivity method for partial similitude can be applied to examine scaling for non-linear response.

With the flight testing, alternative methods of excitations would allow for better identification of the aeroelastic modes in flight. Closed-loop flight controls could be implemented on the ASE Rascal vehicle. Alternative system identification methods, e.g. Filter-Error method, may offer better identification of the system dynamics. The identification of the lateral dynamics is also possible, if a measurement of yaw was added.

Bibliography

[1] Stevens, B. L. and Lewis, F. L., *Aircraft Control and Simulation*, John Wiley and Sons, Inc., Hoboken, 2003.

[2] Nelson, R. C., *Flight Stability and Automatic Control*, McGraw-Hill, Inc., 1998.

[3] "Statistical Summary of Commercial Jet Airplane Accidents: Worldwide Operations 1959-2008," Airplane Safety Engineering, Boeing Commercial Airplane Group, 2009.

[4] Foster, J. V., Cunningham, K., Fremaux, C. M., Shah, G. H., Stewart, E. C., Rivers, R. A., Wilborn, J. E., and Gato, W., "Dynamics Modeling and Simulation of Large Transport Airplanes in Upset Conditions," *AIAA Guidance, Navigation and Control Conference and Exhibit*, No. AIAA-2005-5933, San Francisco, CA, 2005.

[5] Balas, M. J., "Active Control of Flexible Systems," *Journal of Optimization Theory and Applications*, Vol. 25, No. 3, 1978, pp. 415–436.

[6] Dydek, Z. T., Annaswamy, A. M., and Lavretsky, E., "Adaptive Control and the NASA X-15 Program: A Concise History, Lessons Learned, and a Provably Correct Design," *American Control Conference*, Seattle, Washington, 2008.

[7] Patil, M. J., "Nonlinear Gust Response of Highly Flexible Aircraft," *AIAA/ASME/ASCE/AHS/ASC Structures, Structural Dynamics, and Materials Conference*, 2007.

[8] Kier, T. M. and Looye, G. H., "Unifying Manoeuvre and Gust Loads Analysis Models," *International Forum on Aeroelasticity and Structural Dynamics*, No. IFASD-2009-106, Seattle, WA, 2009.

[9] Roughen, K. M., Bendiksen, O. O., and Baker, M. L., "Development of Generalized Aeroservoelastic Reduced Order Models," *Structures, Structrual Dynamics, and Materials Conference*, No. AIAA-2009-2491, Palm Springs, CA, 2009.

[10] Torralba, J., Demourant, F., Puyou, G., and Ferreres, G., "Modeling A Flexible Aircraft as a Continuum using Linear Fractional Transformation," *International Forum on Aeroelasticity and Structural Dynamics*, 2009.

[11] Hodges, D. H., "Lateral-Torsional Flutter of a Deep Cantilever Loaded by a Lateral Follower Force at the Tip," *Journal of Sound and Vibration*, Vol. 247, 2001, pp. 175–183.

[12] Detinko, F. M., "Some phenomena for flutter of beams under follower load," *International Journal of Solids and Structures*, Vol. 39, 2001, pp. 341–350.

[13] Mazidi, A., Fazelzadeh, S., and Marzocca, P., "Flutter of Aircraft Wings Carrying a Powered Engine Under Roll Maneuver," *Journal of Aircraft*, Vol. 48, No. 3, 2011, pp. 874–883.

[14] Milne, R. D., "Dynamics of the Deformable Aeroplane," Tech. Rep. No. 3345, Queen Mary College, University of London, 1962.

[15] Waszak, M. R. and Schmidt, D. K., "Flight Dynamics of Aeroelastic Vehicles," *Journal of Aircraft*, Vol. 25, 1988, pp. 563–571.

[16] Waszak, M. R., Davidson, J. B., and Schmidt, D. K., "A Simulation Study of the Flight Dynamics of Elastic Aircraft," NASA contractor report NASA CR-4102, National Aeronautics and Space Administration, 1987.

[17] Baghdadi, N. and Lowenberg, M. H., "Application of Bifurcation and Continuation Methods to Nonlinear Flexible Aircraft Dynamics," *AIAA Guidance Navigation and Control Conference*, No. AIAA-2009-6305, Chicago, IL, 2009.

[18] Silvestre, F. J. and Luckner, R., "Integrated model for the flight mechanics of a flexible aircraft in the time domain," *International Forum on Aeroelasticity and Structural Dynamics*, No. IFASD-2009-066, Seattle, WA, 2009.

[19] Pogorzelski, G., Zalmanovici, A., da Silva, R. G. A., and Paglione, P., "FlightÂ dynamicsÂ ofÂ theÂ flexibleÂ aircraftÂ includingÂ unsteadyÂ aerodynamicÂ effects," *International Forum on Aeroelasticity and Structural Dynamics*, No. IFASD-2009-084, Seattle, WA, 2009.

[20] Reschke, C., *Integrated Flight Loads Modeling and Analysis for Flexible Transport Aircraft*, Ph.D. thesis, Institut fur Flugmechanik und Flugregelung der Universitat Stuttgart, 2006.

[21] Meirovitch, L. and Tuzcu, I., "Integrated Approach to Flight Dynamics and Aeroservoelasticity of Whole Flexible - Part 1: System Modeling," *AIAA Guidance, Navigation and Control Conference and Exhibit*, No. AIAA-2002-4747, Monterey, CA, 2002.

[22] Meirovitch, L. and Tuzcu, I., "Integrated Approach to the Dynamics and Control of Maneuvering Flexible Aircraft," Tech. Rep. CR-2003-211748, National Aeronautics and Space Administration, 2003.

[23] Meirovitch, L. and Tuzcu, I., "The Lure of Mean Axis," *Journal of Applied Mechanics*, Vol. 74, No. 3, 2007, pp. 497–504.

[24] Nguyen, N., "Integrated Flight Dynamic Modeling of Flexible Aircraft with Inertial Force-Propulsion-Aeroelastic Coupling," *AIAA Aerospace Sciences Meeting and Exhibit*, 2008.

[25] Nguyen, N. and Tuzcu, I., "Flight Dynamics of Flexible Aircraft with Aeroelastic and Inertial Force Interactions," *AIAA Atmospheric Flight Mechanics Conference*, No. AIAA-2009-6045, Chicago, IL, 2009.

[26] Tuzcu, I. and Nguyen, N., "Unsteady Aeroelasticity of Generic Transport Model," *AIAA Atmospheric Flight Mechanics Conference*, No. AIAA-2011-6319, Portland, OR, August 2011.

[27] Grant, P. R., Abbasi, H., and Li, N., "Real-time Simulation of Flexible Aircraft: a Comparison of Two Methods," *AIAA Modeling and Simulation Technologies Conference*, No. AIAA-2009-6024, Chicago, IL, 2009.

[28] Li, N. X., R.Grant, P., and Abbasi, H., "A Comparison of the Fixed-Axis and the Mean-Axes Modeling Methods for Flexible Aircraft Simulation," *Robust Adaptive Control of a Structurally Damaged Aircraft*, No. AIAA-2010-7605, Toronto, ON, 2010.

[29] Patil, M. J. and Hodges, D. H., "Flight Dynamics of Highly Flexible Flying Wings," *Journal of Aircraft*, Vol. 43, 2006, pp. 1790–1798.

[30] Sotoudeh, Z., Hodges, D. H., and Chang, C.-S., "Validation Studies for Nonlinear Aeroelastic Trim and Stability of Hale Aircraft (NATASHA)," *International Forum on Aeroelasticity and Structural Dynamics*, 2009.

[31] Zhao, Z. and Ren, G., "Multibody Dynamic Approach of Flight Dynamics and Nonlinear Aeroelasticity of Flexible Aircraft," *AIAA Journal*, Vol. 49, No. 1, 2011, pp. 41–54.

[32] Niblett, L. T., "The fundamentals of body-freedom flutter," *Aeronautical Journal*, Vol. 90, 1986, pp. 373–377.

[33] Love, M., Zink, P. S., Wieselmann, P., and Youngren, H., "Body Freedom Flutter of High Aspect Ratio Flying Wings," *AIAA/ASME/ASCE/AHS/ASC Structures, Structural Dynamics and Materials Conference*, No. AIAA-2005-1947, Austin, TX, 2005.

[34] Haddad, W. M. and Bernstein, D., "Optimal Reduced-Order Observer-Estimators," *Journal of Guidance, Control, and Dynamics*, Vol. 13, 1990, pp. 1126–1135.

[35] Prudhomme, S., "Low order LG observers for aeroelastic aircraft control," *AIAA Guidance, Navigation, and Control Conference*, No. AIAA-97-3622, New Orleans, LA, 1997.

[36] Frost, S. A., Taylor, B. R., Jutte, C. V., Burken, J. H., Trinh, K. V., and Bodson, M., "A Framework for Optimal Control Allocation with Structural Load Contraints," *AIAA Guidance Navigation and Control Conference*, No. AIAA-2010-8112, Toronto, ON, 2010.

[37] Moulin, B. and Karpel, M., "Gust Loads Alleviation Using Special Control Surfaces," *Journal of Aircraft*, Vol. 44, 2007, pp. 17–25.

[38] Teufel, P., Hanel, M., and Well, K. H., "Integrated Flight Mechanic and Aeroelastic Modelling and Control of a Flexible Aircraft Considering Multidimensional Gust Input," *RTO AVT Specialists' Meeting on "Structural Aspects of Flexible Aircraft Control"*, Ottawa, ON, 1999.

[39] Haghighat, S., Martins, J. R., and Liu, H. H., "Aeroservoelastic Design Optimization of a Flexible Wing," *Journal of Aircraft*, Vol. 49, No. 2, 2012, pp. 432–443.

[40] Gang, C., Jian, S., and Yueming, L., "Active flutter suppression control law design method based on balanced proper orthogonal decomposition reduced order model," *Nonlinear Dynamics*, Vol. 68, No. 4, June 2012.

[41] Gadient, R., Levin, J., and Lavretsky, E., "Comparison of Model Reference Adaptive Controller Designs Applied to the NASA Generic Transport Model," *AIAA Guidance Navigation and Control Conference*, No. AIAA-2010-8406, Toronto, ON, 2010.

[42] Hinson, B., Steck, J., Rokhsaz, K., and Nguyen, N., "Adaptive Control of an Elastic General Aviation Aircraft," *AIAA Guidance, Navigation, and Control Conference*, No. AIAA-2011-6560, Portland, OR, August 2011.

[43] Calise, A. J., Kim, N., and Buffington, J. M., "Adaptive Compensation for Flexible Dynamics," *AIAA Guidance Navigation and Control Conference and Exhibit*, 2002.

[44] Calise, A. J., Yank, B.-J., and Craig, J. I., "Augmenting Adaptive Approach to Control of Flexible Systems," *Journal of Guidance, Control, and Dynamics*, Vol. 27, 2004, pp. 387 – 396.

[45] Zeng, J., Wang, J., de Callafon, R., and Brenner, M., "Suppression of the Aeroelastic/Aeroservoelastic Interaction Using Adaptive Feedback Control Instead of Notching Filters," *AIAA Atmospheric Flight Mechanics Conference*, No. AIAA-2011-6459, Portland, OR, August 2011.

[46] Li, X. L. and Brenner, M. J., "Practical Aeroservoelasticity In-Flight Identification and Adaptive Control," *AIAA Atmospheric Flight Mechanics Conference*, No. AIAA-2010-7502, Toronto, ON, August 2010.

[47] Kim, K., Yucelen, T., Calise, A., and Nguyen, N., "Adaptive Output Feedback Control for an Aeroelastic Generic Transport Model: A Parameter Dependent Riccati Equation Approach," *AIAA Guidance, Navigation, and Control Conference*, No. AIAA-2011-6456, Portland, OR, August 2011.

[48] Nguyen, N., Krishnakumar, K., and and, J. B., "An Optimal Control Modification to Model-Reference Adaptive Control for Fast Adaptation," *AIAA Guidance, Navigation and Control Conference and Exhibit*, No. AIAA-2008-7283, Honolulu, HI, August 2008.

[49] Nguyen, N. T., "Asymptotic Linearity of Optimal Control Modification Adaptive Law with Analytical Stability Margins," *AIAA Infotech@Aerospace*, No. AIAA-2010-3301, Atlanta, GA, 2010.

[50] Avanzini, G., Capello, E., Piacenza, I., Quagliotti, F., Hovakimyan, N., and Xargay, E., "L1 Adaptive Control of Flexible Aircraft: Preliminary Results," *AIAA Atmospheric Flight Mechanics Conference*, No. AIAA-2010-7501, Toronto, ON, August 2010.

[51] Roemer, M., Ge, J., Lew, J.-S., and and, J.-N. J., "Adaptive Flutter Suppression for Aircraft Upset and Damage Conditions," *AIAA Atmospheric Flight Mechanics Conference*, No. AIAA-2011-6369, Portland, OR, August 2011.

[52] Buckingham, E., "On Physically Similar Systems; Illustrations of the Use of Dimensional Equations," *Physical Review*, Vol. 4, No. 4, October 1914, pp. 345–376.

[53] Wolowicz, C. H., James S. Bowman, J., and Gilbert, W. P., "Similitude Requirements and Scaling Relationships as Applied to Model Testing," Tech. Rep. NASA-TP-1435, NASA, August 1979.

[54] Presente, E. H. and Friedmann, P. P., "Aeroservoelasticity in subsonic flow and associated scaling laws," *AIAA/ASME/ASCE/AHS/ASC Structures, Structural Dynamics, and Materials Conference*, No. AIAA-1997-1079, Kissimmee, FL, April 1997.

[55] Presente, E., *Innovative Scaling Laws for Aeroelastic and Aeroservoelastic Problems in Compressible Flow*, Ph.D. thesis, University of California, Los Angeles, 1999.

[56] Norris, G., "Breaking the Flutter Barrier," *Aviation Week & Space Technology*, Vol. 174, No. 5, February 2012, pp. 28.

[57] Beranek, J., Nicolai, L., Burnett, M. B. E., Atkinson, C., Holm-Hansen, B., and Flick, P., "Conceptual Design of a Multi-Utility Aeroelastic Demonstrator," *AIAA Aviation Technology, Integration, and Operations (ATIO) Conference*, No. AIAA-2010-9350, Fort Worth, TX, 2010.

[58] Richards, J., Suleman, A., and Blair, M., "Aeroelastic Scaling of Unconventional Joined Wing Concept for Exploration of Gust Load Response," *International Forum on Aeroelasticity and Structural Dynamics*, No. IFASD-2009-177, Seattle, WA, 2009.

[59] Richards, J., Suleman, A., Aarons, T., and Canfield, R., "Multidisciplinary Design for Flight Test of a Scaled Joined Wing SensorCraft," *AIAA Aviation, Technology, Inte-*

gration, and Operations (ATIO) Conference, No. AIAA-2010-9351, Fort Worth, TX, 2010.

[60] Templeton, J. and Rice, C., "AirSTAR GTM-T2 Modal Test," NASA, July 2009.

[61] Brenner, M. J. and Prazenica, R. J., "Aeroservoelastic Model Validation and Test Data Analysis of the F/A-18 Active Aeroelastic Wing," *International Forum on Aeroelasticity and Structural Dynamics*, Amsterdam, Netherlands, 2003.

[62] Bosworth, J., "Full Scale Flight Validation," *NASA Aviation Safety Conference*, McLean, VA, 2009.

[63] Pavlock, K. M., "Full-Scaled Advanced Systems Testbed: Ensuring Success of Adaptive Control Research Through Project Lifecycle Risk Mitigation," *SFTE International Symposium*, SFTE, Seattle, WA, June 2011.

[64] Cunningham, K., Foster, J. V., Morelli, E. A., and Murch, A. M., "Practical Application of a Subscale Transport Aircraft for Flight Research in Control Upset and Failure Conditions," *AIAA Atmospheric Flight Mechanics Conference and Exhibit*, No. AIAA-2008-6200, Honolulu, HI, 2008.

[65] Jordan, T., Langford, W., Belcastro, C., Foster, J., Shah, G., Howland, G., and Kidd, R., "Development of a Dynamically Scaled Generic Transport Model Testbed for Flight Research Experiments," *AUVSI's Unmanned Systems North America Symposium and Exhibition*, Anaheim, CA, Aug. 2004.

[66] Jordan, T. L., Langford, W. M., and Hill, J. S., "Airborne Subscale Transport Aircraft Research Testbed - Aircraft Model Development," *AIAA Guidance, Navigation, and Control Conference and Exhibit*, No. AIAA-2005-6432, San Francisco, CA, 2005.

[67] Cesnik, C. E. S., Senatore, P. J., Su, W., Atkins, E. M., Shearer, C. M., and Pitchter, N. A., "X-HALE: A Very Flexible UAV for Nonlinear Aeroelastic Tests,"

AIAA/ASME/ASCE/AHS/ASC Structures, Structural Dynamics, and Materials Conference, No. AIAA-2010-2715, Orlando, Florida, 2010.

[68] Morelli, E. A., "Multiple Input Design for Real-Time Parameter Estimation in the Frequency Domain," *13th IFAC Conference on System Identification*, No. REG-360, Rotterdam, Netherlands, 2003.

[69] Brenner, M. J., Lind, R. C., and Voracek, D. F., "Overview of recent flight flutter testing research at NASA Dryden," *AIAA/ASME/ASCE/AHS/ASC Structures, Structural Dynamics, and Materials Conference and Exhibit*, No. AIAA-1997-1023, Kissimmee, FL, 1997.

[70] Troyer, T. D., Runacres, M. C., Guillaume, P., and Peeters, B., "Analysis of Flight Flutter Test Data Using Combined Artificial and Turbulence Excitation," *International Forum on Aeroelasticity and Structural Dynamics*, No. IFASD-2009-058, Seattle, WA, 2009.

[71] Morelli, E. A., "Real-Time Parameter Estimation in the Frequency Domain," *Journal of Guidance, Control, and Dynamics*, Vol. 23, 2000, pp. 812–818.

[72] Morelli, E. A., "Real-Time Aerodynamic Parameter Estimation without Air Flow Angle Measurements," *AIAA Atmospheric Flight Mechanics Conference*, No. AIAA-2010-7951, Toronto, ON, 2010.

[73] Theodore, C. R., Ivler, C. M., Tischler, M. B., Field, E. J., Neville, R. L., and Ross, H. P., "System Identification of Large Flexible Transport Aircraft," *AIAA Atmospheric Flight Mechanics Conference and Exhibit*, No. AIAA-2008-6894, Honolulu, HI, 2008.

[74] Tischler, M. B. and Remple, R. K., *Aircraft and Rotorcraft System Identification: Engineering Methods with Flight Test Examples*, American Institute of Aeronautics and Astronautics, Reston, 2006.

[75] Callafon, R. A., Miller, D. N., Zeng, J., and Brenner, M. J., "Covariance Function Realization Algorithms for Aeroelastic Dynamic Modeling," *AIAA Atmospheric Flight Mechanics Conference*, No. AIAA-2010-7800, Toronto, ON, 2010.

[76] Boely, N. and Botez, R. M., "Identification and validation of a F/A-18 model Using Neural Networks," *AIAA Atmospheric Flight Mechanics Conference*, No. AIAA-2010-7799, Toronto, ON, 2010.

[77] Silva, B., "Data Gathering and Preliminary Results of the System Identification of a Flexible Aircraft Model," *AIAA Atmospheric Flight Mechanics Conference*, No. AIAA-2011-6355, Portland, OR, August 2011.

[78] Mangalam, A. S., Jutte, C., and Brenner, M., "Unsteady Aerodynamic and Structural Measurement of the Aerostructures Test Wing for Flutter Testing," *AIAA Atmospheric Flight Mechanics Conference*, No. AIAA-2010-8113, Toronto, ON, 2010.

[79] Meirovitch, L., *Methods of Analytical Dynamics*, McGraw-Hill, Inc., New York, 1970, pp. 110-112.

[80] Venkatesan, C. and Friedmann, P. P., "New Approach to Finite-State Modeling of Unsteady Aerodynamics," *AIAA Journal*, Vol. 24, 1986, pp. 1889–1897.

[81] Ouellette, J. A., Raghavan, B., Patil, M. J., and Kapania, R. K., "Flight Dynamics and Structural Load Distribution for a Damaged Aircraft," *AIAA Atmospheric Flight Mechanics Conference*, No. AIAA-2009-6153, Chicago, IL, 2009.

[82] Ouellette, J. A., *Flight Dynamics and Maneuver Loads on a Commercial Aircraft with Discrete Source Damage*, Master's thesis, Virginia Polytechnic Institute and State University, 2010.

[83] Drela, M. and Youngren, H., *AVL 3.26 User Primer*, http://web.mit.edu/drela/Public/web/avl/avl_doc.txt, April 2006, Viewed April 15, 2009.

[84] Bisplinghoff, R. L., Ashley, H., and Halfman, R. L., *Aeroelasticity*, Dover Publications, Inc., Cambridge, 1996, pp. 251-281.

[85] Meirovitch, L., *Fundamentals of Vibrations*, McGraw-Hill, Inc., Boston, 2001, pp. 265-267.

[86] Chapra, S. C. and Canale, R. P., *Numerical Methods for Engineers: With Software and Programming Applications*, McGraw-Hill, Inc., Boston, 2002, pp. 620-621.

[87] Tao, G., *Adaptive Control Design and Analysis*, John Wiley & Sons, Inc., Hoboken, 2003.

[88] Ioannou, P. A. and Sun, J., *Robust Adaptive Control*, Pre, Upper Saddle River, NJ, 1996, pp. 313-434.

[89] Rugh, W. J., *Linear System Theory*, Prentice Hall, Upper Saddle River, 1996, pp. 169-181.

[90] Khalil, H. K., *Nonlinear Systems*, Prentice Hall, 2002.

[91] Wilborn, J. E. and Foster, J. V., "Defining Commercial Transport Loss-of-Control: A Quantitative Approach," *AIAA Atmospheric Flight Mechanics Conference and Exhibit*, No. AIAA-2004-4811, Providence, RI, 2004.

[92] Langhaar, H. L., *Dimensional Analysis and Theory of Models*, Robert E. Krieger Publishing Company, Malabar, FL, 1951.

[93] Shigley, J. E., Mischke, C. R., and Budynas, R. G., *Mechanical Engineering Design*, McGraw-Hill, Inc., 2004.

[94] Megson, T., *Aircraft Structures for Engineering Students*, Elsevier Ltd., 1999.

[95] Klien, V. and Morelli, E. A., *Aircraft System Identification: Theory and Practice*, American Institute of Aeronautics and Astronautics, Reston, 2006.

[96] Bowerman, B. L., O'Connell, R. T., and Koehler, A. B., *Forecasting, Time Series, and Regression*, Thompson, Belmont, CA, 2005.

[97] Goland, M., "The Flutter of a Uniform Cantilever Wing," *Journal of Applied Mechanics*, Vol. 12, 1945, pp. A197 – A208.

[98] Goland, M. and Luke, Y. L., "The Flutter of a Uniform Wing With Tip Weights," *Journal of Applied Mechanics*, Vol. 12, 1948, pp. 13 – 20.

Appendix A

Flight Test Cards

TEST LIMITS

- **AIRSPEED: ?? < KIAS < 85**
- **TARGET ALTITUDE: 50' < AGL < 400'**
- **WINDS: <10 MPH**
- **FUEL:**
  - **WEIGHT AT TAKEOFF: >14 OZ**
  - **FLIGHT TIME: <20 MIN**
- **OUTSIDE AIR TEMP (OAT):**
  - **40 F < OAT < 100 F**

NOTES:

COTS Sig Rascal 4			Date:_____
Card #:	Target KIAS:	Maneuver:	Target Altitude:
01	V_{ref}	Familiarization	100

Notes

A. FLY NORMAL PATTERN TO BECOME FAMILIAR WITH AIRCRAFT

COTS Sig Rascal 4			Date:_____
Card #:	Target KIAS:	Maneuver:	Target Altitude:
02	V_{ref}	Trim Shot	100

A. TRIM SHOT
B. NO STICK INPUTS ~10+ SEC

Notes

COTS Sig Rascal 4			Date:_____
Card #:	Target KIAS:	Maneuver:	Target Altitude:
03	V_{min}	Trim Shot	100
C. TRIM SHOT D. NO STICK INPUTS ~10+ SEC			**Notes**

COTS Sig Rascal 4			Date:_____
Card #:	Target KIAS:	Maneuver:	Target Altitude:
04	V_{max}	Trim Shot	100

E. TRIM SHOT
F. NO STICK INPUTS ~10+ SEC

Notes

COTS Sig Rascal 4			Date:_____
Card #:	Target KIAS:	Maneuver:	Target Altitude:
05	V_{ref}	Sys ID	100

G.TRIM SHOT ~3 SEC
H. ELEVATOR SWEEP ~20 SEC
1. START AT 1/2 HZ
2. INCREASE TO 2 HZ

THROTTLE FIXED

Notes

COTS Sig Rascal 4			Date:_____
Card #:	Target KIAS:	Maneuver:	Target Altitude:
06	V_{max}	Sys ID	100

I. TRIM SHOT ~3 SEC
J. ELEVATOR SWEEP ~20 SEC
   1. START AT 1/2 HZ
   2. INCREASE TO 2 HZ

THROTTLE FIXED

Notes

COTS Sig Rascal 4			Date:_____
Card #:	Target KIAS:	Maneuver:	Target Altitude:
07	V_{min}	Sys ID	100

K.TRIM SHOT ~3 SEC
L. ELEVATOR SWEEP ~20 SEC
1. START AT 1/2 HZ
2. INCREASE TO 2 HZ

THROTTLE FIXED

Notes

COTS Sig Rascal 4			Date:_____
Card #:	Target KIAS:	Maneuver:	Target Altitude:
INTENTIONALLY LEFT BLANK			**Notes**

COTS Sig Rascal 4			Date:_____
Card #:	Target KIAS:	Maneuver:	Target Altitude:
08	V_{ref}	Validation	100

M. TRIM SHOT ~3 SEC

N. ELEVATOR DOUBLET

1. STICK BACK ~1 SEC
2. STICK FORWARD ~1 SEC

O. STICK NEUTRAL ~10 SEC

THROTTLE FIXED

Notes

COTS Sig Rascal 4			Date:_____
Card #:	Target KIAS:	Maneuver:	Target Altitude:
09	V_{max}	Validation	100

P. TRIM SHOT ~3 SEC
Q. ELEVATOR DOUBLET
1. STICK BACK ~1 SEC
2. STICK FORWARD ~1 SEC
R. STICK NEUTRAL ~10 SEC

THROTTLE FIXED

Notes

COTS Sig Rascal 4			Date:_____
Card #:	Target KIAS:	Maneuver:	Target Altitude:
10	V_{min}	Validation	100

S. TRIM SHOT ~3 SEC

T. ELEVATOR DOUBLET

1. STICK BACK ~1 SEC
2. STICK FORWARD ~1 SEC

U. STICK NEUTRAL ~10 SEC

THROTTLE FIXED

Notes

COTS Sig Rascal 4			Date:_____
Card #:	Target KIAS:	Maneuver:	Target Altitude:
INTENTIONALLY LEFT BLANK			**Notes**

COTS Sig Rascal 4			Date:_____
Card #:	Target KIAS:	Maneuver:	Target Altitude:
11	V_{ref}	3-2-1 Doublet	100
V. TRIM SHOT ~3 SEC			**Notes**

COTS Sig Rascal 4			Date:_____
Card #:	Target KIAS:	Maneuver:	Target Altitude:
12	V_{max}	3-2-1 Doublet	100
W. TRIM SHOT ~3 SEC			**Notes**

COTS Sig Rascal 4			Date:_____
Card #:	Target KIAS:	Maneuver:	Target Altitude:
13	V_{min}	3-2-1 Doublet	100
X.TRIM SHOT ~3 SEC Y.			**Notes** S

COTS Sig Rascal 4			Date:_____
Card #:	Target KIAS:	Maneuver:	Target Altitude:
INTENTIONALLY LEFT BLANK			**Notes**

COTS Sig Rascal 4			Date:_____
Card #:	Target KIAS:	Maneuver:	Target Altitude:
14	V_{min}	Engine Noise ID	100

Notes

Z. TRIM SHOT ~3 SEC

AA. INCREASE TO FULL THROTTLE ~10+ SEC

1. HOLD AIRCRAFT LEVEL
2. MINIMIZE CONTROLS

COTS Sig Rascal 4			Date:_____
Card #: 15	Target KIAS: V_{min}	Maneuver: Stall Test	Target Altitude: 100
BB. TRIM SHOT ~3 SEC CC. REDUCE THROTTLE TO IDLE 1. HOLD AIRCRAFT LEVEL 2. MINIMIZE CONTROLS DD. RECOVER ONCE STALLED			**Notes**

COTS Sig Rascal 4			Date:_____
Card #: 16	Target KIAS: V_{min}	Maneuver: GVT	Target Altitude: 0
			Notes